WOOD AND FIBER SCIENCE

The Sustainable Natural Materials Journal

Volume 58, Number 4, 2026 (ISSN 0735-6161)

Open Access

JOURNAL OF THE

SWST – International Society of Wood Science and Technology

SOCIETY OF WOOD SCIENCE AND TECHNOLOGY

2025-2026 Officers of the Society

President: **Francesco Negro**, University of Torino, Italy
Immediate Past President: **Ilona Peszlen**, North Carolina State University, Raleigh, NC, USA
President-Elect: **Matthew Schwarzkopf**, Innorenew, Izola, Slovenia
Vice President: **Lech Muszyński**, Oregon State University, Corvallis, OR, USA
Executive Director: **Angela Haney**, Society of Wood Science and Technology, P.O. Box 6155, Monona, WI 53716-1655, execdir@swst.org

Directors

Lili Cai, University of Idaho, USA
Frederico José Nistal França, Mississippi State University, USA
Frederik Laleicke, North Carolina State University, USA
Tahiana Ramananantoandro, University of Antananarivo, Madagascar
Editor, *Wood and Fiber Science*: Eric Hansen,Oregon State University, USA
Associate Editors, *Wood and Fiber Science*: Andreja Kutnar, University of Primorksa, Slovenia; Ling Li, University of Maine, USA; and Arijit Sinha, Oregon State University, USA
Digital Communication Coordinator: Lena Leiter, BOKU University, Austria
Editor, *BioProducts Business*: Pipiet Larasatie, Virginia Tech, USA

WOOD AND FIBER SCIENCE

Wood and Fiber Science is published quarterly in January, April, July, and October by the Society of Wood Science and Technology, P.O. Box 6155, Monona, WI 53716-6155

Editor

Eric Hansen
Oregon State University
eric.hansen@oregonstate.edu

Associate Editors

Andreja Kutnar, University of Primorska
Andreja.kutnar@innorenew.eu

Ling Li, University of Maine
ling.li@maine.edu

Arijit Sinha, Oregon State University
arijit.sinha@oregonstate.edu

Editorial Board

Stergio Adamopoulos, Sweden
Babatunde Ajayi, Nigeria
Susan Anagnost, USA
Claudio Del Menezzi, Brazil
Levente Denes, Hungary
Yusuf Erdil, Turkey
Massimo Fragiacomo, Italy
Fred França, USA
Steven Keller, USA
Shujun Li, China
Lucian Lucia, USA
Sameer Mehra, Ireland
John Nairn, USA
Francesco Negro, Italy
Jerrold Winandy, USA
Qinglin Wu, USA

There are three classes of membership (electronic only) in the Society: Members – dues $150; Retired Members – dues $75; Student Members – dues $25. We also have a membership category for individuals from Emerging Countries where individual members pay $30, individual students pay $10; Emerging Groups of 10 pay $290, and Student Groups of 10 pay $90. Institutions and individuals who are not members pay $300 per volume (electronic only). Applications for membership and information about the Society may be obtained from the Executive Director, Society of Wood Science and Technology, P.O. Box 6155, Monona, WI 53716-6155 or found at the website https://www.swst.org.

Site licenses are also available with a charge of:

$300/yr for single online membership, access by password and email
$500/yr for institutional subscribers with 2–10 IP addresses
$750/yr for institutional subscribers with 11–50 IP addresses
$1000/yr for institutional subscribers with 51–100 IP addresses
$1500/yr for institution subscribers with 101–200 IP addresses
$2000/yr for institutions subscribers with over 200 IP addresses.

New subscriptions begin with the first issue of a new volume. All subscriptions are to be ordered through the Executive Director, Society of Wood Science and Technology. The Executive Director, at the Business Office shown below or by email to execdir@swst.org, should be notified 30 days in advance of a change of email address.

Business Office: Society of Wood Science and Technology, P.O. Box 6155, Monona, WI 53716-6155.
Editorial Office: Eric Hansen, eric.hansen@oregonstate.edu
Copy Editor, *Wood and Fiber Science* and *BioProducts Business*: Caryn M. Davis, Cascadia Editing, Philomath, OR USA

EDITORIAL AND PUBLICATION POLICY

Wood and Fiber Science as the official publication of the Society of Wood Science and Technology publishes open access papers with both professional and technical content. Original papers of professional concern, or based on research of international interest dealing with the science, processing, and manufacture of wood and composite products of wood or wood fiber origin will be considered.

All manuscripts are to be written in US English, the text should be proofread by a native speaker of English prior to submission. Any manuscript submitted must be unpublished work not being offered for publication elsewhere.

Papers will be reviewed by referees selected by the editor and will be published in approximately the order in which the final version is received. Research papers will be judged on the basis of their contribution of original data, rigor of analysis, and interpretations of results; in the case of reviews, on their relevancy and completeness.

Color photos/graphics will be offered at no additional cost to authors. The Open Access fee will be $1800/article for SWST members and $2000/article for nonmembers. Reduced rates are available for authors based in developing countries.

Technical Notes

Authors are invited to submit Technical Notes to the Journal. A Technical Note is a concise description of a new research finding, development, procedure, or device. The length should be **no more than two printed pages in WFS**, which would be five pages or less of double-spaced text (TNR12) with normal margins on 8.5 x 11 paper, including space for figures and tables. In order to meet the limitation on space, figures and tables should be minimized, as should be the introduction, literature review and references. The Journal will attempt to expedite the review and publication process. As with research papers, Technical Notes must be original and go through a similar double-blind, peer review process.

On-line Access to *Wood and Fiber Science* Back Issues

SWST is providing readers with a means of searching all articles in *Wood and Fiber Science* from 1968 to present.

Visit the SWST website at https://www.swst.org and go to Wood & Fiber Science Online. Click on either SWST Member Publication access (SWST members) or Subscriber Publication access (Institution Access). All must login with their email and password on the https://www.swst.org site or use their ip authentication if they have a site license.

As an added benefit to our current subscribers, you can now access the electronic version of every printed article along with exciting enhancements that include:

- IP authentication for institutions (only with site license)
- Enhanced search capabilities
- Email alerting of new issues
- Custom links to your favorite titles

(ISSN 0735-6161)

WOOD AND FIBER SCIENCE

JOURNAL OF THE SOCIETY OF WOOD SCIENCE AND TECHNOLOGY

VOLUME 58 OCTOBER 2026 NUMBER 4

CONTENTS

Articles

SILVANA CALVANO, FRANCESCO NEGRO, EMMA OLIVER, ISLAM HAFEZ, AND ALESSANDRO PORTALURI
Curve comparison in wood science: An introductory guide to common cases 217

KAELIN QUIGLEY, MATTHEW KONKLER, SKYLER FOSTER, AND GERALD PRESLEY
Assessment of polycyclic aromatic hydrocarbons (PAHs) migration from creosote-treated Douglas-fir and southern pine posts over a 38-month period 230

SAMUEL OLAJIDE, TOMIWA HARUNA, ALHASSAN IBRAHIM, ROBERT MACIAS, GERALD PRESLEY, AND ISLAM HAFEZ
Structural and chemical characterization of Douglas-fir and red alder biochar 249

MOJTABA HASSAN VAND AND JAN TIPPNER
An investigation of the impact response of European ash and sycamore maple 263

ZOE A. E. SPERDUTO AND FIONA A. O'DONNELL
Defining perpendicular to grain compression stress: A comparison of methods and recommendations for ASTM D143 277

Curve comparison in wood science: An introductory guide to common cases

Silvana Calvano †
PhD student
Department of Agricultural, Forest and Food sciences, University of Torino, Italy;
Email: silvana.calvano@unito.it

Francesco Negro *†
Associate professor
Department of Agricultural, Forest and Food sciences, University of Torino, Italy;
Email: francesco.negro@unito.it

Emma Oliver
BS student
Department of Wood Science and Engineering, Oregon State University, Corvallis, OR 97331, USA;
Email: oliveemm@oregonstate.edu

Islam Hafez
Assistant professor
Department of Wood Science and Engineering, Oregon State University, Corvallis, OR 97331, USA;
Email: islam.hafez@oregonstate.edu

Alessandro Portaluri
Full professor
Department of Agricultural, Forest and Food sciences, University of Torino, Italy;
Email: alessandro.portaluri@unito.it

(Received 27 March 2026)

Abstract: Empirical curves are essential for describing and analyzing phenomena in wood science. Although the theoretical framework is well established, the complexity of handling curves can hinder their proper application, which is likely to be more common in practice than generally assumed. This article aims to support the effective use and comparison of curves in wood science, and it is mainly intended as an accessible guide for approaching curve comparison, from the basic concepts of dependent and independent variables to the most complex of curve fitting and linearization. After a brief introduction and framework, this study addresses various key concepts, including types of curves, independent and dependent variables, linearization, and number of specimens required. These aspects are discussed through a methodological framework that can be useful in common situations. A section on avoiding common pitfalls is included as well. Proper confidence in handling curves is important not only to avoid errors, but also to enable their effective use, which can result in a more accurate description and a deeper understanding of phenomena.

Keywords: Curve comparison; Curve fitting; Wood science; Wood technology.

Introduction

Curves representing the relationship between independent and dependent variables are common in wood science. They are used to investigate a wide range of topics, from the fundamental behavior of wood to the properties of innovative products (Niemz et al. 2024).

There are several approaches to compare curves, and the statistical methods addressing the most common cases are well established (Hedderich and Sachs 2024). Nonetheless, guidance tailored to experimental conditions and data structures commonly encountered in wood science remains limited. In practice, researchers often adopt methods developed in other disciplines which may not fully reflect the specific characteristics of wood as a heterogeneous material or the testing procedures commonly adopted in wood science.

Curve comparison is not straightforward because curves may differ in shape, scale, rate of change, asymptotic behavior, or variability, and because observations collected along the same curve are often not statistically independent. The appropriate comparison method therefore depends on the structure of the

* Corresponding author
† Society of Wood Science & Technology member

data, the scientific question, and the assumptions of the selected model. An unsuitable method may obscure relevant differences or produce misleading conclusions. For this reason, researchers need a clear framework for selecting the most appropriate analytical approach for the curve-comparison problem under investigation.

To the best of our knowledge, methodological guidance specifically addressing common curve-comparison problems in wood science remains limited and fragmented. This paper aims to contribute to this area by providing an accessible framework for selecting and applying appropriate approaches. First, the theoretical background is presented, followed by examples drawn from published studies in wood science. Referring directly to examples from wood science is intended to facilitate comprehension, as it avoids translating examples from other disciplines. This paper provides an accessible framework for approaching the comparison of families of planar curves commonly encountered in wood science, drawing on established mathematical and statistical methods. This scope covers a broad range of common curve-comparison situations encountered in wood science research, from the basic concepts of dependent and independent variables to the most complex of curve fitting and linearization.

It should be noted that the aim of this work is not to provide a universal recipe, which would hardly be feasible, considering the broadness of the topic. Readers, especially postgraduate and PhD students, are encouraged to deepen their understanding of statistics and to consult appropriate statistical textbooks (see also the Limitations section). However, this article offers operational guidelines for approaching the most common case of curve comparison in wood science and for developing clear and effective manuscripts.

A brief mathematical theoretical framework

Mathematical descriptions and experimental observations in wood science are commonly expressed in the form of relationships between one or more independent variables and a response variable. These relationships between one dependent and one independent variable are typically represented graphically as curves either derived from theoretical formulations or obtained from experimental measurements. As a result, curves constitute a primary aspect of analysis across a wide range of wood science applications. Indeed, mathematical models are used to understand, predict, and optimize properties and behaviors of wood and wood-based materials. They can be categorized into several key areas, with some examples provided in Table 1.

Table 1. List of common mathematical models used in wood science, grouped per thematic areas. Examples include mathematical laws, well-established models, and models proposed in recent literature.

Area	Models	Examples
Physico-mechanical properties	**Mechanical properties**: predict wood mechanical properties based on wood characteristics like grain orientation, density, and moisture content.	Hankinson equation for wood compression strength (Eq. 10.47 in Niemz et al. 2024)
	Fracture mechanics: describe how wood fails under different loading conditions.	Linear Elastic Fracture Mechanics (LEFM) models (Chapter 9.4.7 in Niemz et al. 2024)
Moisture content and hygroscopic behavior	**Moisture diffusion**: predict how water moves through wood in different conditions.	Fick's law and its formulations (Eqs. 7.43-7.47 in Niemz et al. 2024)
	Sorption isotherms: explain how wood absorbs and desorbs moisture at different relative humidities.	Guggenheim-Anderson-de Boer (GAB) model (eq 7.11 in Niemz et al. 2024)
Thermal conductivity and fire reaction	**Heat transfer:** predict how heat moves through wood.	Fourier's law (Eq. 13.9 in Niemz et al. 2024)
	Charring rate: estimate the rate at which wood chars during a fire.	PYCIF heat-mass-pyrolysis model (Pečenko et al. 2023)
Natural durability	**Fungal growth:** predict fungal growth and wood decay rates.	Finnish mold growth model (or VTT model (Hukka and Viitanen 1999)
	Insect attack: assess risks of insect attack using population dynamics and environmental factors.	Modelling the influence of host plants on the distribution of emerald ash borer (Dang et al. 2021)
Wood processing and manufacturing	**Sawing and drying:** optimize cutting patterns and drying schedules.	Page's equation (e.g., Schuler Frantzen et al. 2026)
	Adhesives: analyze how bonding strength varies depending on parameters like wood density, resin content, etc.	Dai's internal bonding model for wood composites (Dai et al. 2008)
Sustainability	**Carbon sequestration:** estimate how much biogenic carbon trees store over time.	Chapman-Richards function (Robinson et al. 2025)
	Forest growth and yield: predict tree growth or timber yield under different climatic and management conditions.	Chapman-Richards function with mixed effects (Eslamdoust et al. 2026)
Computational and machine learning	**Finite element models (FEM):** simulate mechanical behavior and stress distributions in wood products and structures.	FEM analysis of tensile-load resistance of mortise-and-tenon wood joints (Hu et al. 2018)
	Artificial neural networks (ANN): predict wood properties based on large datasets of experimental results.	ANN to predict the quality of thermally modified wood (Bozkurt and Özbay 2026)

From a mathematical viewpoint, some models are described by differential equations, either ordinary or partial and derived from first principles (fundamental axioms or postulates), while others are derived from empirical functions. These models usually rely on specific parameters that serve to tune them. In most cases, their solutions can be expressed as functions of one or two independent variables. Therefore, they can be graphically represented by planar curves or surfaces. These models usually depend on one or more parameters that characterize the corresponding family of functions. Such parameters are generally estimated or calibrated from experimental data, whereas the independent variables constitute the arguments of the model.

The simplest case is that of functions depending on a single variable. Their graphs can be represented in a Cartesian reference frame xOy by plotting the dependent variable on the y-axis and the independent variable on the x-axis. A typical example in wood science is the stress-strain diagram shown in Figure 1. The experimental relation may be represented either as stress as a function of strain or, conversely, as strain as a function of stress. Exchanging the two axes replaces each point (ε, σ) with (σ, ε); geometrically, this corresponds to reflecting the plotted curve across the bisector $y = x$, provided that the same graphical scaling is used. In standard mechanical testing, stress is usually plotted on the y-axis and strain on the x-axis, particularly in displacement- or strain-controlled tests. This convention, however, should not be interpreted as establishing a causal relation: the choice of axes, the control mode of the testing device, and the physical dependence between stress and strain are distinct aspects of the experiment.



Figure 1. Experimental tests are usually set up to have strain as the independent variable and stress as the dependent one.

Types of curves

In practice, curves encountered in wood science differ primarily in the way they are represented and derived. From an analytical perspective, this leads to a limited number of recurring curve types, which differ in terms of continuity, parameterization, and suitability for statistical treatment. Three main types of curves are typically encountered in wood science as described below and in Figure 2.

1. *Infinite series of points based on mathematical models*. An empirical model function can be visualized as an infinite series of points, in which for each value of x, a corresponding value of y can be calculated. Over time, research in wood science has defined well-established mathematical models that describe several behaviors of wood and derived products. Empirical curves are commonly used in wood science, usually when comparing experimental data with expected behaviors.
2. *Finite series of points fitted by a curve* (see also curve fitting section). When data points are collected by experimental measurements, a curve can be fitted to these points to describe the phenomenon under investigation. When the functional

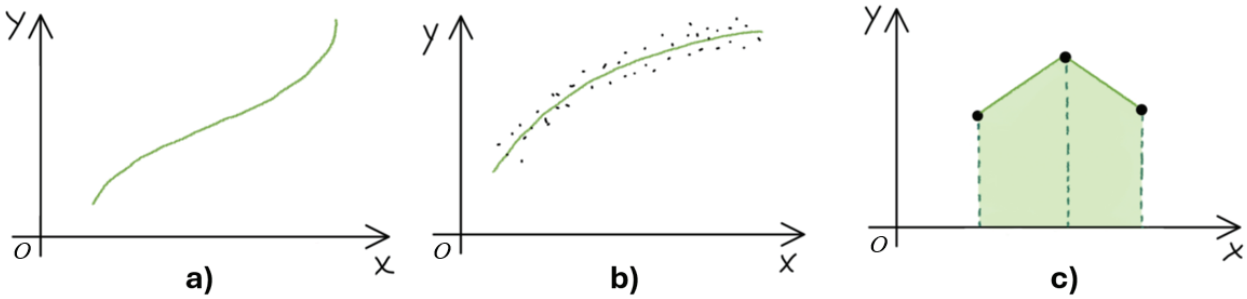


Figure 2. Three curve types typically encountered in wood science: (a) an infinite series of points coming from a mathematical model (e.g., sorption isotherm models depicting wood equilibrium moisture content, EMC, vs. relative humidity); (b) a curve fitting to a finite series of points (e.g., shape change vs. wood EMC, where the points are measured data and the line depicts the fitted curve); and (c) a finite series of points for which a fitting is not proposed, for various possible reasons; the points, which may be shown or not, are connected by broken or smooth lines (e.g., shear resistance in bonding quality test vs. glue spread rate).

dependence between the independent and dependent variables is known, the curve is fitted accordingly using a suitable class of functions, usually depending upon one or several parameters. When the relationship is not known, fitting different types of curves can be attempted. The class of candidate fitting functions should not be selected solely by analogy with similar datasets or by the number of available observations. For any finite dataset, infinitely many functions can be constructed that interpolate all observed points exactly. Therefore, a good numerical fit does not by itself identify an appropriate model. The choice of the fitting function should instead be guided primarily by the theoretical, physical, or biological model underlying the process under investigation, together with the expected qualitative behavior of the response, such as monotonicity, asymptotic limits, convexity, or the presence of saturation. The amount and distribution of the data remain important because they determine how reliably the model parameters can be estimated and how adequately the model assumptions can be checked. However, even a large dataset cannot compensate for the use of an inappropriate model family.

3. *Series of points for which a fitting is not proposed*. In many cases, researchers may choose not to fit a curve to a series of points. For example, curve fitting should be avoided when a mathematical model associated with the phenomenon under investigation is not known. Another case is when the resulting fitting, even if desirable, does not adequately represent the data. In other cases, data may be just too scarce to propose a curve fitting. It is also important to note that polynomial functions, particularly those of third degree or higher, may fit the observed data very well. However, unless the underlying process is known to be polynomial in nature, such a fit should be regarded only as an empirical approximation and not necessarily as the most accurate, interpretable, or physically meaningful representation of the phenomenon.

When curve fitting is not applied, it is quite common to connect points by lines. The resulting broken line can also be smoothed to transform it into a smooth curve, even though an analytic formal expression is not associated with it. Despite the lack of a formal expression, it is possible to calculate parameters related to the curved or broken line. For example, the trapezoidal rule enables the calculation of the area under a broken line: the area under each segment of the line is a trapezoid, and the sum of the areas of the n trapezoids is the total area under the curve.

The distinction between these curve types is not only descriptive, but it directly affects the choice of appropriate statistical methods. The following sections build on this classification to discuss the selection of independent and dependent variables and the extraction of meaningful quantities for curve comparison.

Figure 3 depicts the process to approach curve comparison. Provided that it is not intended as a universal recipe, it provides a reference methodology that applies to several common cases in wood science. In addition, the curve fitting section reports a specific example from wood science to show how the methodological flow chart applies in practice and to give an example of the elements considered in a specific case study. The remaining part of the article follows the conceptual workflow of Figure 3, which also indicates the sections of the text that correspond to the numbers in the figure, as well as pitfalls to be consulted alongside the process (see Table 2 for section numbers key).

Choosing explanatory variables and model factors

In a mathematical model, an independent variable is an argument of the function, while the dependent variable is the corresponding response. In statistical applications, independent variables are also commonly referred to as explanatory variables or predictors. Their values may be set by the experimental protocol, as in the case of treatment temperature, or recorded during the study, as in the case of time or initial moisture content (MC).

This article focuses primarily on curve-comparison problems involving one or two explanatory variables. These may be continuous predictors or categorical factors with two or more levels. For example, wood density may be treated as a continuous predictor to estimate wood swelling (Pulgar and Riesco 2024, see below) or as a categorical factor, e.g., with “low”, “medium”, and “high” levels (Nugroho et al. 2025). More complex experimental designs may also include blocking variables, covariates, repeated-measures factors, or random effects. Although it is possible to design studies with more than two independent variables, models involving several explanatory variables and their interactions may require more complex experimental designs and statistical methods. Since this article is intended as an introductory guide, it focuses mainly on situations involving one or two primary explanatory variables, while acknowledging that additional blocking factors, covariates, repeated-measures structures, and random effects may also be present.

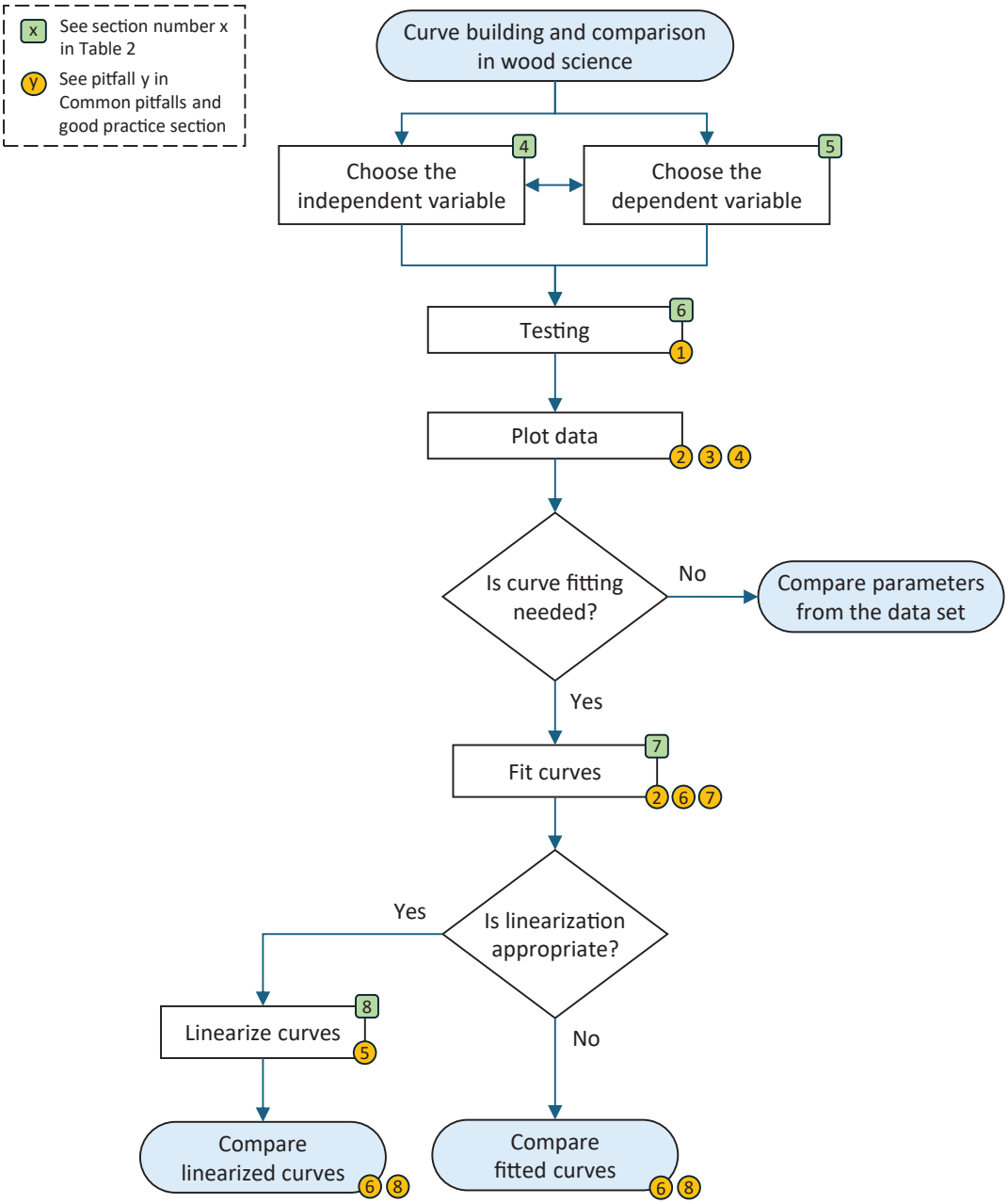


Figure 3. Methodological flow chart to approach the most common cases of curve comparison in wood science (see Table 2 for section numbers key).

Table 2. Key to section numbers shown in green squares in Figure 3 (the numbers in orange circles refer instead to pitfalls in the Common pitfalls and good practice section).

Section title in paper	Corresponding section number in Figure 3
Introduction	1
A brief mathematical theoretical framework	2
Types of curves	3
Choosing explanatory variables and model factors	4
Choosing the dependent variable	5
The number of specimens	6
Curve fitting	7
Linearization	8

The main categories of explanatory variables and model factors commonly encountered in curve comparison are listed below, along with representative examples from wood science.

Continuous predictors are numerical variables that can take values on a continuous scale. They are commonly used in regression models to describe how a response changes as the predictor varies. For example, in wood drying, wood density may be treated as a continuous predictor to estimate swelling and shrinkage values (Pulgar and Riesco 2024).

Categorical factors classify observations into two or more distinct groups or levels. Their effects may be investigated using methods such as ANOVA when the relevant assumptions are satisfied. In wood science, a typical example is the comparison of the mechanical properties of wood from different clones or species (e.g., Calvano et al. 2026a, Nyobe et al. 2024).

Blocking variables are categorical variables that are not the primary focus of the study but may contribute systematic variation to the response. Experimental units are grouped into blocks so that this source of variability can be accounted for separately from the treatment effect. For example, in a randomized complete block design on wood physico-mechanical properties, wood provenance can be included in the statistical model as a blocking factor rather than removed from the analysis (Chen et al. 2026).

Covariates are usually continuous variables that are not the main object of investigation but may influence the response. They are included in the statistical model so that comparisons among the groups of primary interest can be adjusted for their effect. In ANCOVA, for example, a covariate may be used to compare treatment groups at a common or adjusted value of that variable. For example, Abe et al. (2016) investigated the light conducting properties as a method to identify two wood species from archeological artifacts. Wood density was set as the covariate because it affects light conduction, and wood species as the independent variable.

Repeated-measures factors arise when the same experimental units are observed repeatedly at different time points or under different conditions. The resulting observations are generally correlated and therefore cannot be treated as independent replicates. Repeated-measures ANOVA or, more flexibly, mixed-effects models may be used to account for this dependence. For example, Zhang et al. (2025) investigated the decay of paper birch and red pine wood by measuring the mass loss of specimens collected from the same in-field logs (the experimental units) over a period of five years.

Random effects represent sources of variation associated with groups, subjects, or clusters whose observed levels are regarded as a sample from a broader population. They are commonly included in mixed-effects models to account for correlation among observations belonging to the same group and to estimate variability among groups. For example, when comparing wood properties, tree identity may be included as a random effect because wood specimens from the same tree are likely to be more similar to one another than specimens taken from different trees (e.g., Adutwum et al. 2023).

Finally, these categories describe different aspects of a statistical model and are not always mutually exclusive. A variable may be continuous or categorical in mathematical terms, while also having a particular role in the experimental design. For example, time may be treated as a continuous predictor (e.g., to estimate the shape change of hygromorphic wood bilayers, see Table 4), but measurements taken over time on the same specimen can also form a repeated-measures structure (e.g., Zhang et al. 2025 cited above). The appropriate classification therefore depends both on the nature of the variable and on the role it plays in the scientific question and statistical model.

Choosing the dependent variable

Dependent variables are quantities measured to assess changes resulting from the independent variables. They are traditionally thought of as a recorded variable in a dataset. As stated in the mathematical theoretical framework section (above), the y-variable, graphed on the y-axis, is the dependent variable for data with one independent variable. Although correct and often very useful, this is a narrow definition of the concept. Dependent variables, in fact, can include any quantity that adheres to the definition above, including curve parameters.

Curve parameters are unknown coefficients estimated during the fitting procedure. Once estimated separately for each experimental unit, their values may subsequently be treated as response variables when comparing groups. For example, if the same quadratic model is fitted to each specimen, the resulting specimen-specific estimates of its coefficients may be statistically compared across treatments. So, when fitting curves based on the function $y(x) = ax^2$, the a coefficient operates as a parameter that is adjusted to find the best curve. Once finalized, it can be used as a dependent variable to compare different curves based on the same function.

A key question in curve comparison is which dependent variable(s) should be considered. Several curve parameters may be of interest, such as the maximum or the average value,

the slope at a specific point, the area under the curve (AUC), etc. It is therefore necessary to determine which parameter is more useful to investigate. Five main situations can be found in practice in wood science, as outlined in Table 3 and Figure 4.

Finally, another option is to linearize data, which consists in transforming the relationship between variables to make it linear (see the Linearization section, which lists three common cases of data linearization). Linearization is performed to simplify data interpretation, to improve model outputs, or to meet statistical assumptions. Linearized relationships can then be compared by analyzing differences in regression coefficients (slopes) or intercepts. This is typically achieved using ANCOVA, as a general linear model that combines ANOVA and regression.

Table 3. Parameters to be considered when analyzing curves in wood science. The examples listed are not intended to be exhaustive, nor to describe how to conduct data analysis. Instead, they provide a prompt reference for visualizing some practical applications of the theoretical cases.

n.	Parameters being considered	Notes	Examples in wood science
1	One point	Information from the curve is lost. The analysis is reduced to one-dimensional data.	Brinell hardness of densified birch and aspen wood (Fig. 5 in Altgen et al. 2026) Bending strength of glue laminated timber beams (Fig. 7 in Martins et al. 2025).
2	Two or more points	Information from the curve is partially lost. Comparison between points is possible, but the trend between points is not considered.	Mechanical properties of wood plastic composites measured every day over 8-d water immersion (Fig. 10 in Rezakalla 2025) Mass loss values depending on wood moisture content to assess the moisture dynamics of brown rot degradation (Fig. 9 in Belt et al. 2026)
3	A section of the curve	Considering a section of the curve can be chosen by convention, as in standards that prescribe how to calculate the modulus of elasticity (MOE). It can also be chosen because of particular interest, such as, for example, focusing on the behavior of wood in the first 2 h of testing.	Near-infrared spectroscopy to determine MoE in static bending of Mongolian oak wood (Fig. 5 in Liang et al. 2018) Fracture evolution stage of four wood species under compact tension load (Fig. 6 in Hu et al. 2021)
4	The entire curve	The entire curve is considered, whereas single points are not, or are not the focus. This approach is particularly suitable for curves with similar paths.	Deformation of hygromorphic bilayers made from different woods over 24-h conditioning cycles (Fig. 3 in Calvano et al. 2026b) Time-temperature effect on plywood and oriented strand board creep deflection (Fig. 4 in Miyamoto and Sinha 2025)
5	Two or more of the previous approaches	Taking into account both punctual parameters (cases 1 and 2 from this Table) and those related to the curve (cases 3 and 4) provides a broader picture of the phenomenon under study. In some cases, it may be necessary to assess the relationship between the parameters considered.	- Flame spread evolution and final value for treated Japanese cedar wood subjected to a 10-min Steiner tunnel test (Fig. 3 in Jang and Park 2026). - Bending force at proportionality limit and at maximum limit in bending strength test of beech and aspen wood (Figs. 3 and 5 in Svoboda et al. 2017)

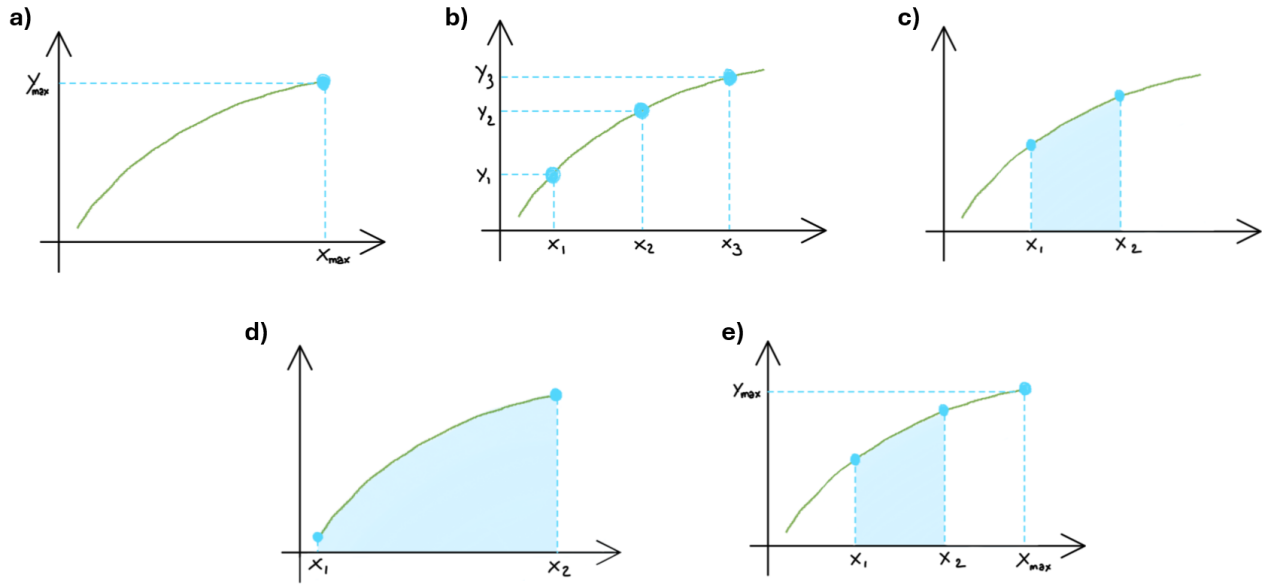


Figure 4. Parameters considered when analyzing curves, according to Table 3: (a) one point (type 1 in Table 3); (b) two or more points (type 2); (c) a section of the curve (type 3); (d) the entire curve (type 4); and (e) two or more of the previous approaches (type 5).

The number of specimens

The number of specimens depends on the specific case under investigation. There are theoretical methods for calculating it depending on the expected variability, e.g., ISO 3129 (2019). In practice, two operational approaches are generally accepted in wood science. First, the number of specimens is set based on other research studies that are taken as a reference. Second, the number is chosen based on the prescriptions of technical standards, like EN 326-1 (1994) for wood-based panels. In both cases, it is not rare to test a higher number of specimens to make the statistical analysis more robust. When these operational criteria are used, the expected variability should also be considered. A higher number of specimens is generally required for highly variable materials such as solid wood, whereas a lower number may sometimes be adequate for more homogeneous engineered wood products. Ideally, however, the number of specimens should be justified by considering the expected effect size, variance, desired statistical power, number of treatment groups, and repeated-measures structure. Importantly, multiple observations collected along the same curve do not increase the number of independent experimental units.

Curve fitting

Preliminary considerations on curve fitting have already been discussed in Types of curves, particularly in the sections "Finite series of points fitted by a curve" and "Series of points for which a fitting is not proposed." Some additional aspects that should be considered when fitting and evaluating a curve are discussed below.

A fundamental step in curve fitting is the analysis of residuals, defined as the differences between the observed values and the corresponding values predicted by the fitted model. Residual analysis helps assess whether the selected model adequately represents the phenomenon under investigation. Ideally, residuals should be randomly distributed around zero and contain no systematic patterns. Trends, curvature, changes in variance, clusters, or unusually large residuals may indicate model misspecification, non-constant variance, dependence among observations, or the presence of influential data points. In such cases, the model assumptions, the selected functional form, or the experimental structure should be reconsidered.

Another important step is the evaluation of goodness-of-fit, which describes how closely the fitted curve represents the observed data. Several complementary measures may be used. The coefficient of determination, (R^2), represents the proportion of variability in the response accounted for by the model and generally ranges from 0 to 1, with values closer to 1 indicating a closer fit. However, (R^2) should be interpreted cautiously, particularly for nonlinear models, and should not be used as the sole criterion for model selection. Adjusted (R^2) penalizes the inclusion of additional predictors and is therefore useful when comparing models of different complexity within an appropriate regression framework. The root mean squared error (RMSE) is the square root of the mean squared residuals and measures the typical magnitude of the prediction errors in the units of the response variable. Lower RMSE values indicate a closer fit, provided that the models are evaluated using the same dataset and response scale.

Confidence intervals for the fitted parameters should also be reported. They quantify the uncertainty associated with the estimated coefficients. Narrower confidence intervals generally indicate greater precision, whereas wider intervals suggest that the available data do not determine the parameter accurately. However, precise parameter estimates do not by themselves demonstrate that the selected model is scientifically appropriate.

Researchers should also consider whether the selected model and its parameters have a clear physical or biological interpretation. Purely empirical functions, such as high-order polynomials, may reproduce the shape of the observed data without explaining the mechanisms responsible for that shape. By contrast, models containing physically interpretable parameters, such as the unit shrinkage coefficient of wood, may support a more meaningful scientific interpretation of the phenomenon. This consideration is especially important when fitted parameters are subsequently compared among experimental groups. The same model should adequately describe all groups before its estimated parameters are compared.

Finally, overfitting, excessive smoothing, and the use of models without physical justification are discussed in the common pitfalls section. These issues should be considered together with residual analysis, goodness-of-fit measures, parameter uncertainty, and the scientific meaning of the selected model.

Table 4 reports an example of a study based on curve fitting, representing one of the most complex scenarios covered in this article. This example complements Table 3 (on parameters to be considered), Figure 3 (on the methodological flowchart), and this section on curve fitting.

Linearization

In the workflow of Figure 3, linearization is an optional step considered after a plausible model has been selected.

Table 4. Example from a recent study (Calvano et al. 2026b) based on the methodological framework shown in Figure 3.

Activity	Example
Choose the experimental design, including selection of the independent and dependent variables and review of similar studies in literature.	The study investigates the shape change of hygromorphic wood bilayers over time. The active layer is made with two wood species (independent variable n. 1), and bilayers are bonded using two adhesives (independent variable n. 2). The shape change over time (dependent variable) is compared using two-way ANOVA (2x2). The experimental design is similar to that of a study taken as a reference.
Conduct the experimental testing.	Four different bilayers are tested. Ten specimens per bilayer are produced. The shape change of each specimen, in mm, is measured at regular intervals over 24 h.
Plot the series of points for each specimen.	The series of points obtained for each specimen are plotted in a Cartesian reference frame.
Perform the curve fitting for each specimen.	Curve fitting is performed according to a function (model) widely accepted in literature. Residuals are randomly scattered around the zero line. The goodness-of-fit is assessed by (R^2). As a result, a curve is associated with each of the 10 specimens per panel.
Is linearization needed?	Linearization is not needed. The fitted curves are compared.
Measure the values of the dependent variable(s) for each curve.	The area under the curve (AUC) is calculated for each specimen. This results in 10 specimen-level AUC values for each bilayer type. These values are retained as the experimental observations used in the statistical analysis; group means are reported only as descriptive summaries.
Perform the statistical analysis.	Boxplots are drafted to have a visual representation, but they are not included in the article. A two-way ANOVA is conducted on the specimen-level AUC values to assess the effects of wood species, adhesive type, and their interaction.
Compare the results of the statistical analysis.	Non-significant and significant differences are discussed.

Linearization is one of several approaches available for analyzing nonlinear relationships and should be considered when the transformation produces an approximately linear relationship and the assumptions of the resulting statistical model are satisfied. Its main advantage is that parameters of a nonlinear model may become the slope and intercept of a straight line, facilitating graphical diagnostics and, when assumptions are met, statistical comparisons among experimental groups. For example, consider a family of empirical quadratic models of the form

$$y(x) = ax^2 + bx \quad [1]$$

where (a) and (b) are parameters estimated from the data and used to tune the model. Both parameters contribute to the shape of the curve: (a) controls its curvature, whereas (b) controls its linear component and, in particular, its slope at ($x = 0$). Therefore, comparing the fitted curves only through (a) would neglect the contribution of (b) and could lead to an incomplete or misleading interpretation. A rigorous comparison should instead consider the parameter vector ((a, b)), together with the possible statistical dependence between the two estimates.

When a simpler representation is desirable, the model can be linearized, for $x \neq 0$, by dividing both sides by x:

$$\frac{y(x)}{x} = ax + b \quad [2]$$

In the transformed coordinates, (a) and (b) become, respectively, the slope and the intercept of a straight line. This representation may facilitate the simultaneous comparison of both parameters using linear-model methods, provided that the transformation is appropriate for the data and that the assumptions on the transformed residuals are verified. In this view, ANCOVA can test differences in slopes through the interaction between the predictor and the group, and differences in intercepts through the group effect.

Linearization should not be applied automatically. The transformation must be defined over the observed range and should yield an approximately linear relationship with independent residuals and reasonably constant variance. Because transformations can alter the error structure and the relative weighting of observations, direct nonlinear regression is generally preferable when assumptions are better satisfied on the original scale, when asymptotic parameters must be estimated from the same data, or when uncertainty is required on the original measurement scale. The following subsections illustrate three common transformations.

Linearization of an exponential model

A standard exponential-type model has a solution of the following form:

$$y(x) = y_0 + C\, e^{-kx} \quad [3]$$

where x is a real number and C at [3] is a positive constant. By setting $Y(x) = \ln(y(x) - y_0)$ and $q = \ln C$, the previous equation reduces to:

$$Y(x) = -k\, x + q \quad [4]$$

which is the Cartesian equation of a line, in the $\widehat{XOZ}$-plane, having slope $-k$ and y-intercept q. Thus, by changing the parameters k and q, a two-parameter family of lines in a semi-logarithmic representation is obtained. Implementing this change of coordinates in the dataset provides a linear dependence between the variable x and the variable Y, as at [4].

This transformation requires $y(x) > y_0$ and treats y_0 as known or fixed independently; for a decreasing exponential curve, $k > 0$. Statistically, the slope estimates $-k$ and the intercept estimates $q = \ln C$. When several treatments or material groups are compared, ANCOVA can test whether their decay rates (slopes) or initial amplitudes (intercepts) differ. This requires independent observations and an adequate residual structure on the transformed scale. Repeated measurements from the same specimen should instead be analyzed with a repeated-measures or mixed-effects model. If y_0 must be estimated from the same observations, direct nonlinear regression is usually preferable.

Linearization of a super-exponential model

A different treatment is deserved for the super-exponential model, starting with

$$y(x) = y_0 + C\, e^{-kx^n} \quad [5]$$

where C, k, and n are positive constants, and $x \geq 0$. The following chain of inequalities holds:

$$y_0 < y(x) \leq y_0 + C \quad [6]$$

By setting $Y(x) = \ln\left(\frac{y(x) - y_0}{C}\right)$ and by considering the previous inequalities, one obtains Y(0) = 0, whereas for x > 0, $Y(x) < 0$. By setting $Z(x) = \ln(-Y(x))$, which is well defined for x > 0 because $Y(x) < 0$; by also setting $X = \ln x$, the previous super-exponential model reduces to the straight-line having Cartesian equation given by:

$$Z(X) = q + n\,X \quad [7]$$

where $q = \ln k$. Thus, the relationship is linear on a log-log scale. Once again, a two-parameter family of straight lines is obtained, where the parameters are the slope and the y-intercept.

The slope is n and the y-intercept is $q = \ln k$, so group differences in curve shape and rate can again be assessed by comparing slopes and intercepts. Particular care is required near $x = 0$ and when $y(x)$ approaches y_0, because the logarithms can amplify measurement error. If y_0 or C is estimated rather than known, its uncertainty propagates into the transformed variables; direct nonlinear regression may therefore be more reliable.

Linearization of a logarithmic-type model

A standard logarithmic-type model has a solution of the following form:

$$y(x) = y_0 - k\ln(x + 1) \quad [8]$$

where $x \geq 0$ and k is any nonzero constant. By setting $Z(x) = y(x) - y_0$ and $X(x) = \ln(x + 1)$, the previous equation reduces to a linear equation in the Cartesian $\widehat{XOZ}$-plane; namely:

$$Z(X) = -k\,X \quad [9]$$

Since $X \geq 0$, the previous equation defines a one-parameter family of half-lines through the origin of the transformed $\widehat{XOZ}$-plane, parametrized by k and lying in the right half-plane.

Here, $-k$ is the slope. If y_0 is known, the regression may be constrained to pass through the origin; if y_0 is estimated from the data, an intercept should be included or the original model should be fitted directly. For comparisons among groups, a group-by-X interaction tests differences in k.

In summary, linearization is useful when it yields an interpretable straight-line representation and an acceptable residual structure. It should be regarded as one possible branch of the workflow in Figure 3, not as a compulsory replacement for nonlinear fitting.

Common pitfalls and good practice

Although statistical methods for curve analysis and comparisons are well established, their practical application may still lead to misleading results if data are processed or interpreted improperly. This is particularly relevant in wood science, where experimental variability and complex material behavior require careful handling of data. While some issues, such as data scarcity and overfitting, were discussed earlier in the Types of curves section, the following points highlight additional pitfalls frequently encountered in practice and outline good practices that help ensure reliable and meaningful curve comparison.

1. Treating repeated points from the same specimen as independent observations should be avoided. This may be tempting when sample size is limited, but it violates the basic assumption of independent observations. It creates several distortions like artificially increased sample size, incorrect standard errors, narrower confidence intervals, and altered p-values. One example is that of collecting multiple spectra at different points of the same specimens in Fourier transform infrared spectroscopy (FTIR) analysis

and treating them as independent replicates. This risk may arise in various fields of wood science, especially when dealing with a limited number or small-sized prototypes or samples. This may occur for various reasons, including the constraints of the experimental design, the need to find a balance with the availability of partner industries, and the need to limit costs. Repeated observations need not be avoided, but their dependence must be accounted for in the statistical analysis. Measurements obtained from the same specimen should not be treated as independent replicates; depending on the experimental design, repeated-measures or mixed-effects models may instead be required.

2. Inappropriate data processing can compromise the results. For example, excessive smoothing of experimental curves is another frequent pitfall. Smoothing techniques can help reduce measurement noise, but applying them excessively may distort important features of the curve, such as local maxima, inflection points, or sudden changes in slope. As a result, the smoothed curve may no longer represent the actual behavior of the material. For example, sound absorption of wood-based panels may be measured at 2 Hz intervals by testing devices, and showing the data only for octave-thirds (63, 125, 250, 500, 1000, 2000, 4000, 8000 Hz) may result in overlooking relevant absorption peaks. Additionally, in FTIR spectra of wood and wood-based materials, excessive smoothing can broaden or reduce the intensity of absorption bands, merge closely spaced peaks, and obscure weak shoulders associated with subtle chemical changes. Smoothing should therefore be applied cautiously and only when it does not alter the relevant characteristics of the data.

3. It should also be noted that spectroscopic curves often require additional transformations of raw signals to improve comparability between samples and reduce instrumental effects such as baseline drift or differences in signal intensity. Common procedures include baseline correction and normalization of the spectra. Although these treatments can facilitate comparison between measurements, they may also modify the shape or relative intensity of spectral features if applied improperly. For example, aggressive baseline correction can remove meaningful peaks, while inappropriate normalization may amplify noise or distort peak ratios. These transformations should therefore be applied carefully and consistently to all samples. In addition, the procedures used should be clearly described in the methods section so that the analysis can be reproduced and correctly interpreted.

4. Curves should be plotted in a way that allows readers to easily understand the data. Overcrowded plots with too many curves, unclear legends, or indistinguishable line styles can make interpretation difficult. Showing representative curves together with variability indicators (e.g., error bands or boxplots of derived parameters) often improves clarity. In addition, curves should be presented using consistent units and scales. Differences in axis scaling, unit conversion, or normalization methods can create misleading visual impressions. When multiple curves are compared in the same figure, identical axes and clearly defined units help ensure a fair comparison. In wood science, it is common to investigate the properties of several different statistical groups, for example, in terms of wood species, type of engineered product, adhesive, etc. The risk of overcrowding graphs is therefore often present: when needed, graphical ways to split the plots and increase the readability of figures should be considered.

5. Another common issue concerns the interpretation and presentation of error bars. These are frequently used to show variability in experimental data, but their meaning is not always clearly stated. In particular, it is often unclear whether the bars represent the standard deviation, the standard error of the mean, or confidence intervals. Since these quantities describe different aspects of variability, failing to specify them can lead to incorrect interpretation of the results. In addition, overlapping error bars are sometimes interpreted as evidence that two curves are not significantly different. This assumption is not generally valid, because statistical significance depends on the specific statistical test and sample size rather than on visual overlap alone. A good practice is to clearly report what the error bars represent and to use formal statistical tests to support conclusions about differences between curves. Similarly, failing to report confidence intervals or uncertainty bands hides the accuracy of the results and encourages over-interpretation, especially when differences seem large enough at first glance.

6. Using linearization without recognizing that transformations can alter error structure and bias parameter estimates. Linearization, in fact, alters the error structure of the data and can lead to bias in estimates. Therefore, reasons for applying linearization and the deriving limitations should be clearly mentioned.

7. Comparing fitted parameters without checking whether the same model is appropriate for all groups can lead to misleading results because different groups may be governed by different relationships. In such cases, the analysis may reveal statistical differences, when the actual difference lies in the fact that the model fits some groups only. For example, engineered wood products bonded with different

adhesives may react differently to environmental conditions because thermoplastic and thermosetting adhesives behave according to different models.

8. Using high-order polynomials without physical justification, just to get nice fittings, may lead to several drawbacks, including overfitting. For example, polynomials may very well fit the data and oscillate widely between them at the same time. Also, polynomials may return inconsistent predictions, even slightly outside the range of the measured data.

9. Fitted curves are sometimes used to estimate values outside the range of experimental data. This can be risky because the model may not represent the physical behavior of the material outside the measured interval. In wood science, properties often change nonlinearly with variables such as MC, temperature, or strain, so extrapolated values may be unreliable. For example, the modulus of elasticity behaves differently within the proportionality limit (the maximum stress at which the stress-to-strain ratio remains linear) and above it, where different types of non-linear behavior occur. Similarly, dimensional changes in wood are proportional to MC change below the fiber saturation point (FSP). Above the FSP, further changes in MC generally produce negligible or no additional swelling or shrinkage. Interpretations should therefore be limited to the range of observed data unless the model has a clear theoretical basis.

Limitations

The purpose of this work is to provide an introductory reference for dealing with the most common cases of curve comparison in wood science. Therefore, this article has a deliberately focused scope. Accordingly, it does not aim at replacing the study of statistics at the postgraduate and PhD student level, nor at replacing the more comprehensive content of statistical handbooks. In particular, several statistical concepts are mentioned briefly here. This is because full discussion of these concepts would require more space, and would be better suited to a book chapter or a book. Similarly, the flowchart in Figure 3 is intended as a general guideline for the most common situations, while deepening into the various elements is left to the development of the research being conducted.

Conclusion

Curves are fundamental in wood science for describing the relationships between independent and dependent variables. However, understanding and effectively comparing curves is not always straightforward, which can limit their practical application. The methodological flowchart included in this article provides an operational reference to tackle the key decision points in curve comparison, including choosing independent and dependent variables, fitting curves, applying linearization if appropriate, and comparing curves. Common pitfalls, including excessive smoothing, overfitting, and failure to assess the meaning of the parameters considered, are also listed as a practical tool for performing sound research.

While open questions in curve comparison mainly concern advanced or application-specific cases, a broader methodological issue is the incomplete reporting of model selection, diagnostics, dependence structures, and uncertainty. The framework proposed here may help authors describe these aspects more clearly in the materials and methods sections of their papers, thereby improving the reproducibility and comparability of curve-based studies in wood science.

A proper understanding of curves goes beyond simply avoiding errors or following standard procedures. Instead, it enables a more proactive approach to research which allows researchers to handle curves of varying complexity with confidence. This, in turn, allows for a deeper and more precise description and comprehension of the phenomena under investigation, ultimately contributing to the advancement of knowledge in wood science.

References

Abe H, Watanabe K, Ishikawa A, Noshiro S, Fujii T, Iwasa M, Kaneko H, Wada H (2016) Simple separation of *Torreya nucifera* and *Chamaecyparis obtuse* wood using portable visible and near-infrared spectrophotometry: differences in light-conducting properties. J Wood Sci 62:210–212. https://doi.org/10.1007/s10086-016-1541-z

Altgen M, Altgen D, Pasca D, Zimmer K (2026) Temporary property changes and moisture-driven recovery in thermo-mechanically densified birch and aspen wood. Eur J Wood Wood Prod 84:35. https://doi.org/10.1007/s00107-026-02400-w

Adutwum JO, Sakagami H, Koga S, Matsumura J (2023) An application of mixed-effects model to evaluate the role of age and size on radial variation in wood specific gravity in teak (*Tectona grandis*). J Wood Sci 69:9. https://doi.org/10.1186/s10086-023-02076-3

Belt T, Treu A, Möttönen V, Altgen M (2026) Moisture dynamics during *Coniophora puteana* brown rot degradation of Scots pine sapwood. Int Biodeterior Biodegrad 209:106296. https://doi.org/10.1016/j.ibiod.2026.106296

Bozkurt Ö, Özbay G (2026) Artificial neural networks as a decision-support system for predicting the quality attributes of thermally modified wood. Eur J Wood Prod 84:125. https://doi.org/10.1007/s00107-026-02478-2

Calvano S, Bombieri A, Rizza D, Bergante S, Chiarabaglio PM, Cremonini C, Negro F, Zanuttini R (2026a) New poplar clones from conventional and agroforestry plantations in Northern Italy: preliminary results on peeling attitude and properties of solid wood and plywood. Forests 17:130. https://doi.org/10.3390/f17010130

Calvano S, Negro F, Goli G, Togni M, Cremonini C, Zanuttini R (2026b) Active behavior of poplar wood bilayers in response to changes in relative humidity. J Build Eng 118:115087. https://doi.org/10.1016/j.jobe.2025.115087

Chen F, Peng J, Jiang Y, Shi L, Ma J, Ma XQ, Cao Z, Li M (2026) Multi-trait evaluation and selection of elite *Cunninghamia lanceolata* provenances for high-quality, large-diameter and knot-free timber. Ind Crops Prod 241:122868. https://doi.org/10.1016/j.indcrop.2026.122868

Dai C., Yu C, Jin J (2008) Theoretical modeling of bonding characteristics and performance of wood composites. Part IV. Internal bond strength. Wood Fiber Sci 40(2):146–160.

Dang YQ, Zhang YL, Wang XY, Xin B, Quinn NF, Duan JJ (2021) Retrospective analysis of factors affecting the distribution of an invasive wood-boring insect using native range data: the importance of host plants. J Pest Sci 94:981–990. https://doi.org/10.1007/s10340-020-01308-5

Eslamdoust J, Vasiliauskas S, Little T, Ashiq MW (2026) Height–diameter modeling of tree species in boreal and mixed forests using a mixed-effects approach and stand-level variables. For Sci Technol 22(1):217–230. https://doi.org/10.1080/21580103.2025.2571222

EN 326-1 (1994). Wood-based panels - Sampling, cutting and inspection - Part 1: Sampling and cutting of test pieces and expression of test results. European Standards. https://www.en-standard.eu/bs-en-326-1-1994-wood-based-panels-sampling-cutting-and-inspection-sampling-and-cutting-of-test-pieces-and-expression-of-test-results/

Hedderich J, Sachs L (2024) Applied Statistics. Methods using R. Springer Berlin, Heidelberg. 1023 p. https://doi.org/10.1007/978-3-662-70074-7

Hu W, Guan H, Zhang J (2018) Finite element analysis of tensile load resistance of mortise-and-tenon joints considering tenon FIT effects. Wood Fiber Sci 50(2):121–131. https://doi.org/10.22382/wfs-2018-014

Hukka A, Viitanen HA (1999) A mathematical model of mould growth on wooden material. Wood Sci Technol 33:475–485. https://doi.org/10.1007/s002260050131

ISO 3129 (2019). Wood - Sampling methods and general requirements for physical and mechanical testing of small clear wood specimens. International Standards. https://www.iso.org/standard/74839.html

Jang ES, Park HJ (2026) Horizontal flame spread of flame-retardant-treated Japanese cedar (*Cryptomeria japonica*) exterior siding material. Wood Fiber Sci 58(1):53–59. https://doi.org/10.22382/wfs-2026-06

Liang H, Zhang M, Gao C, Zhao Y (2018) Non-destructive methodology to determine modulus of elasticity in static bending of *Quercus mongolica* using Near-Infrared Spectroscopy. Sensors 18:1963. https://doi.org/10.3390/s18061963

Longford NT (2010) Analysis of Covariance. In: Peterson P., Baker E., McGaw B. International Encyclopedia of Education (Third edition). Elsevier, Amsterdam, pp. 18–24. https://doi.org/10.1016/B978-0-08-044894-7.01304-X

Martins C, Ferreira C, Monteiro SRS, Dias AMPG (2025) Mechanical properties of sweet chestnut sawn wood and glulam performance. Eur J Wood Wood Prod 83:112. https://doi.org/10.1007/s00107-025-02266-4

Miyamoto BT, Sinha A (2025) Time-temperature effects on early-stage primary thermal creep of plywood and oriented strand board (OSB) at elevated temperatures. Wood Fiber Sci 57(1):15–26. https://doi.org/10.22382/wfs-2025-02

Niemz P, Teischinger A, Sandberg D (2024) Springer Handbook of Wood Science and Technology. Springer Nature Switzerland, Cham. 2069 p. https://doi.org/10.1007/978-3-030-81315-4

Nugroho WD, Anjayani GD, Tampubolon AF, Pradhana AW, Cipta H, Tiyasa NP, Yamagishi Y, Kudo K, Rahman MH, Nakaba S, Funada R (2025) Stem gravitropism and tension wood formation in three tropical woody species with different wood densities. J Wood Sci 71:23. https://doi.org/10.1186/s10086-025-02196-y

Nyobe CJ, Nyobe NS, Nkibeu JB, Oum Lissouck R, Ayina Ohandja LM (2024) Effect of slope of grain on mechanical properties of some tropical wood species. Wood Mater Sci Eng 20(3):448–494. https://doi.org/10.1080/17480272.2024.2356047

Pečenko R, Hozjan T, Huč S (2023). Modelling charring of timber exposed to natural fire. J Wood Sci 69:19. https://doi.org/10.1186/s10086-023-02091-4

Pulgar JA, Riesco G (2024) Implementing linear mixed effects models to enhance estimation of the dimensional stability of wood of *Laurus nobilis* L. For Syst 33(2):e05. https://doi.org/10.5424/fs/2024332-20854

Robinson N, Drever CR, Gibbs DA, Lister K, Esquivel-Muelbert A, Heinrich V, Ciais P, Silva-Junior, CHL, Liu Z, Pugh, TAM, Saatchi S, Xu Y, Cook-Patton SC (2025) Protect young secondary forests for optimum carbon removal. Nat Clim Chang 15:793–800. https://doi.org/10.1038/s41558-025-02355-5

Rezakalla AI (2025) The impact of water exposure on the mechanical properties of a wood-plastic composite. Wood Fiber Sci 57(4):205–212. https://doi.org/10.22382/wfs-2025-18

Schuler Frantzen B, Silveira EA, Cruz Lamas G, de Oliveira TF (2026) Intermittent versus continuous kiln drying of hardwood boards: comparable-stage analysis of energy use, kinetics, quality, and climate impacts. Biomass Bioenerg 213:109443. https://doi.org/10.1016/j.biombioe.2026.10944

Svoboda T, Gaffová Z, Rajnoha R, Šatanová A, Kminiak R (2017). Bending forces at the proportionality limit and the maximum - technological innovations for better performance in wood processing companies. BioResources 12(2):4146–4165. https://doi.org/10.15376/biores.12.2.4146-4165

Hu W, Liu Y, Li S (2021) Characterizing mode I Fracture behaviors of wood using compact tension in selected system crack propagation. Forests 12:1369. https://doi.org/10.3390/f12101369

Xu X, Pan R, Chen R (2021) Combustion characteristics, kinetics, and thermodynamics of pine wood through thermogravimetric analysis. Appl Biochem Biotechnol 193:1427–1446. https://doi.org/10.1007/s12010-020-03480-x

Zhang Y, Peng Z, Song Z, Schilling JS (2025) Repeated measures of decaying wood reveal the success and influence of fungal wood endophytes. mSystems 10:e00382-25. https://doi.org/10.1128/msystems.00382-25

Assessment of polycyclic aromatic hydrocarbons (PAHs) migration from creosote-treated Douglas-fir and southern pine posts over a 38-month period

Kaelin Quigley
Department of Wood Science and Engineering
Oregon State University
Email: kaelin.quigley@oregonstate.edu

Matthew Konkler
Department of Wood Science and Engineering
Oregon State University
Email: Matthew.Konkler@oregonstate.edu

Skyler Foster
Department of Wood Science and Engineering
Oregon State University
Email: skyler.foster@oregonstate.edu

Gerald Presley *†
Department of Wood Science and Engineering
Oregon State University
Email: gerald.presley@oregonstate.edu

(Received 18 June 2026)

Abstract: Creosote is a widely used industrial wood preservative largely used for infrastructure-related applications such as utility poles, railway ties, and marine pilings. Polycyclic aromatic hydrocarbons (PAHs) are the predominant component, and some PAHs in creosote have been identified by the Environmental Protection Agency (EPA) as priority pollutants. While research on PAHs found in aquatic environments is widespread, studies on terrestrial PAH migration from creosote-treated wood commodities are less common. This study sought to quantify the extent (quantity, distance, and depth in soil column) of PAH migration from creosote-treated wood in ground contact by measuring the concentration of 16 EPA-regulated PAHs in soil around creosote-treated Douglas-fir and southern pine posts over a 38-month period. The concentrations of PAHs were highly variable from chemical to chemical and timepoint to timepoint, but a few trends were discernible. Where differences were apparent between the two wood species, soils around southern pine posts tended to have higher PAH concentration than soils around Douglas-fir posts, likely due to the differences in chemical retention in the outer 25 mm of the wood, at 143 kg/m^3 and 52 kg/m^3, respectively. Lighter PAHs, particularly naphthalene and acenaphthene, were often found in controls. This indicates that some of the lighter PAHs likely originated from a combination of environmental inputs such as wildfire smoke and vehicle emissions in addition to creosote. Distance from the post surface also played a role in determining PAH concentration for several PAHs. Several higher molecular weight PAHs (fluoranthene, pyrene, benz [a] anthracene, chrysene, benzo [a] pyrene and others) were more frequently identified in samples taken 15 cm from the post than in samples taken 30 cm from the posts in the later sampling times. This field study is ongoing and will continue to examine PAH migration from creosote-treated commodities.

Keywords: Wood preservative; Soil; Ground contact.

Introduction

Creosote is a widely used industrial wood preservative for protecting utility poles, marine pilings, railroad ties, and other commodities against fungi, insects, and marine borers. Creosote has seen historically wide usage as an effective wood preservative since its patent was filed by Franz Moll, a German chemist in 1836, and its subsequent inception in the United States in 1865 (Webster 1992). In 1952, approximately 227 million gallons of creosote and creosote solutions were used in the United States (Baechler and Stamm 1954), though that number has declined more recently, with North American industry estimates totaling around 82.9 million gallons of all creosote formulations used in 2007 (Vlosky 2009).

Chemically, coal tar creosote is formed from the destructive distillation (pyrolysis) of bituminous coal. This process, commonly known as coking, is the process of heating coal at elevated temperatures to form a high-carbon form of coal

* Corresponding author
† Society of Wood Science & Technology member

Wood and Fiber Science, 58(4), 2026, pp. 230–248.
https://doi.org/10.22382/wfs-2026-20

ultimately used to smelt steel. The viscous byproduct formed from coking, creosote, is a variable and complex mixture of hundreds of chemicals, including polycyclic aromatic hydrocarbons or PAHs (up to 85% of mass), phenolic compounds (10% of mass), and heterocyclic aromatic compounds (5% of mass) (Mueller et al. 1989; Nestler 1974). An analysis of creosote used in a former commercial wood treatment facility also detected up to 1505 individual compounds and 231 additional derivatized compounds (Gallacher et al. 2017).

As the largest constituent of creosote, PAHs are a structurally related class of compounds globally and are not specific to creosote as a wood preservative. Processes that include the partial and inefficient combustion of organic matter, such as forest fires, release PAHs in smoke (Navarro et al. 2019; O'Malley et al. 2024), and anthropogenic sources such as the burning of fossil fuels (Wilson and Jones 1993) act as a release of PAHs into the environment. Some PAHs are either known, probable, or suspected carcinogens that have also been shown to negatively impact the function of various organisms in different ecosystems (Eisler 1987) such as fish and other aquatic invertebrates (Duncan et al. 2017; Gewurtz et al. 2000). Because of the potentially toxic characteristics of some PAHs, 16 PAHs ranging from two to six fused aromatic rings are classified and regulated as priority pollutants by the US Environmental Protection Agency (EPA) under the Clean Water Act (US EPA 1981). Because many of these PAHs have several possible sources in the environment, quantifying the relative contribution of creosote-treated commodities is important in quantifying their environmental impact.

Historically, creosote-treated pilings were widespread, and prior literature regarding the environmental performance of creosote is somewhat limited to that of aquatic environments (Bestari et al. 1998; Brooks 2004; Kang et al. 2005; Murphy and Brown 2005; Shupe et al. 2006). While some studies have shown limited impacts of creosote on aquatic life living on or around creosote-treated pilings, today new construction using creosote pilings is limited, and terrestrial applications are more widespread (Goyette and Brooks 1998). Terrestrial applications commonly used include railroad crossties/sleepers and utility poles, with 98% of railway ties in the US having been treated with creosote or creosote solution (RTA 2025).

Prior work to quantify PAH migration from railroad ties shows that increases in PAH from creosote railroad ties in wetland sediments were detectable up to at least 0.75 m away from an experimental railroad ballast (Brooks 2004). Total PAH losses were small, however, and resulted in only about a 0.3 µg/g increase in total PAH concentration in neighboring wetland sediment and fell well below any thresholds expected to negatively impact biological systems. At the end of their service life, it is estimated that 65% of the creosote remains in the treated railway tie (Bolin and Smith 2013). Railroad ballasts suspending the treated ties have a buffering effect for treated commodities, and creosote-treated wood found in direct ground contact may represent a greater environmental risk.

Several studies have examined PAH migration from creosote-treated railroad ties or utility poles in service or in storage. Cargouët et al. (2018) found that the maximum sum of all measured PAH concentrations in soil derived from old creosote-treated railway ties in storage ranged from 2 mg/kg up to 140 mg/kg on a dry weight basis, but decreased dramatically within a few centimeters from the railway ties in storage. Similarly, a study on PAHs found in soil and olives near derelict creosote-treated railroad ties ranged from around 115 to 2160 µg/kg in total for light PAHs up to 1 m from the railway tie, but measured PAH concentration decreased dramatically with distance (Moret et al. 2007). Later work also showed that PAH migration from creosote-treated utility poles was limited to about a 20-cm radius around each pole (Brooks 2020). However, the number of direct studies on PAH migration from wood in ground contact remains relatively limited. Further study of PAH migration from creosote-treated wood in a service-replicated scenario can help disentangle its impact from that of other environmental pollutants.

In this study, the migration of 16 PAHs classified as EPA Priority Pollutants and constituents of creosote-treated Douglas-fir and southern pine posts was examined at a field test site near Corvallis, Oregon over a 38-mo period. The data presented in this study provides data on the species- and time-dependent migration pattern(s) of 16 PAHs at different distances from the treated wood surface and depths within the soil column.

Experimental methods

Acquisition and analysis of creosote-treated posts

In this study, five coastal Douglas-fir (*Pseudotsuga menziesii*) and five southern pine posts 15–20 cm in diameter and 2.4 m long were treated with a P1/P13 creosote fraction at commercial facilities in Oregon (Douglas-fir) and in the southeastern United States (southern pine). Posts were stored under cover prior to installation at the field site. Creosote retention levels in the outer 0–25 mm of the posts were assayed according to the AWPA A6 standard method for the determination of retention of oil-type preservatives from small samples (AWPA



Figure 1. Photo of field test setup showing southern pine and Douglas-fir posts set below ground in soil at Peavy Arboretum. Untreated control posts were located above creosote-treated posts along the gradual hillside to prevent downslope migration of PAHs in the soil column from creosote-treated posts.

2020) as an aggregate sample for all posts included in the test. Creosote-treated Douglas-fir posts contained 52 kg/m^3 creosote and southern pine posts contained 143 kg/m^3 creosote in the outer 25 mm assay zone.

Experimental design

A field-scale migration study was performed at the Peavy Arboretum about 10 km north of Corvallis, Oregon (Figure 1). The field site is located in a maritime climate with average daily high temperatures ranging from 7.7°C in January to 28.3°C in August. Annual rainfall at the site is about 1084 mm, with the majority falling from October to May. Soil at the Peavy Arboretum field site was subjected to a full soil panel at the Soil Health Laboratory at Oregon State University, Corvallis. Results of the physical and chemical analyses are shown in Table 1. The soil is a clay texture and is rich in organic matter, with relatively high microbial respiration rates.

Creosote-treated posts were placed 0.6 m below groundline at the Peavy Arboretum field site. In addition, two untreated Douglas-fir posts were used as controls. Soil taken from the hole dug for each post was analyzed for the presence of 16 PAHs found in creosote, and these were labeled as 0-mo samples for each post. Soil samples were taken using a 2.5 × 61 cm (1.0 × 24-in.) stainless steel soil corer to obtain 46 cm (18-in.) soil cores. Soil cores were taken with the center of the soil sampler centered at each sampling distance. Soil sampling times included 0-mo (background), 3-mo, 6-mo, 12-mo, and 38-mo after post installation. For each sampling period, the soil cores were taken at a different part of the radius around the post to reduce disturbances between samplings.

Table 1. Soil characteristics at the Peavy Arboretum field test site, Corvallis, Oregon.

Characteristic	Quantity
% Moisture	9
% Sand	22
% Silt	34
% Clay	44
% Water stable aggregates	99
% C	13.28
% N	0.6
% Organic matter	26.56
Active carbon (ppm)	1073.44
CO_2 respiration 24 h (µg CO_2-C/g dry soil/day)	273.85
CO_2 respiration 96 h (µg CO_2-C/g dry soil/day)	131.63
Potentially mineralizable nitrogen (ppm NO_3-N time 0)	1.77
Potentially mineralizable nitrogen (ppm NO_3-N time 28)	4.01
Potentially mineralizable nitrogen (mg N/kg soil/day)	0.08
pH	5.61
P (ppm)	29.81
K (ppm)	233.24
Ca (ppm)	6235.49
Mg (ppm)	1152.82
Cation exchange capacity (meq/100g)	41.38

For the background (0-mo) samples, soil was collected from soil augured out of the ground to set the post. For the 3- and 6-mo sampling point, soil was sampled 15 cm from the treated post. For the 12- and 38-mo sampling points, soil samples were taken at two distances, 15 and 30 cm from the treated post. The total 46 cm (18 in.) long soil cores were divided into three 15-cm (6 in.) sections, an upper 0–15 cm, middle 15–30 cm, and lower 30–46 cm section (Figure 2). The 46 cm (18 in.) soil cores were difficult to obtain intact so they could be reliably sectioned into 15 cm sections, and the sampling method required some distance from the post to maneuver the soil corer. This limited the closest distance to 15 cm from the outside surface of the post. The 30 cm sampling distance was added to help identify distance-dependent trends in PAH accumulation in soil around creosote-treated roundwood.

Each soil section (upper, middle, or lower) was homogenized and retained for PAH extraction. The soil coring apparatus was cleaned of all soil between each core taken by wiping off excess soil, rinsing the coring apparatus with water while cleaning it with a brush, and finally spraying it down with ethanol and wiping it to dry. All soil samples taken in this study were frozen until extracted for 16-PAHs, as described in the section below.

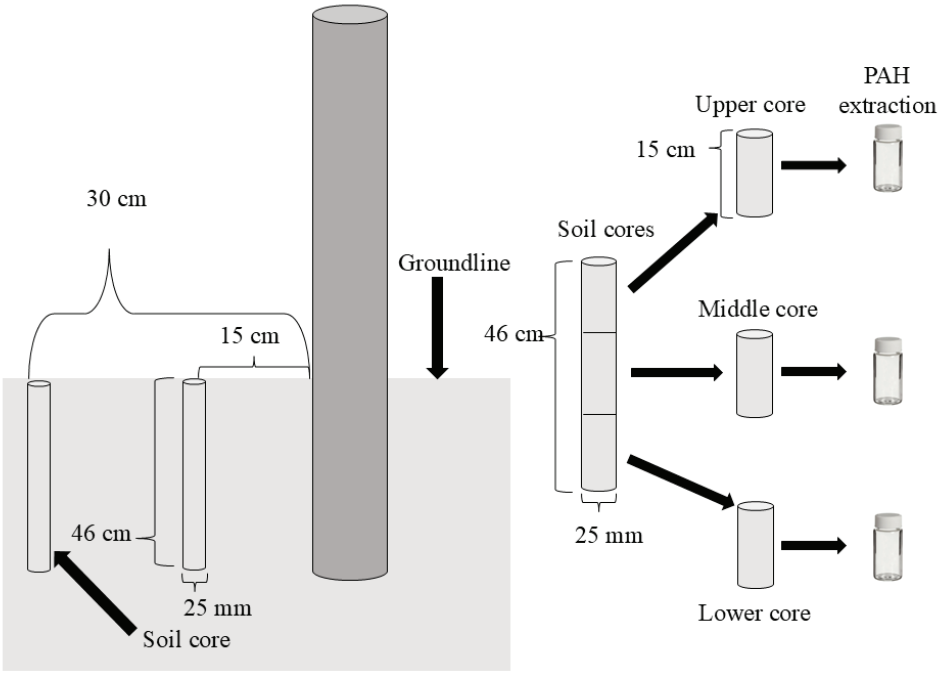


Figure 2. Diagram of soil sampling regime and division of complete soil sampling core into three respective segments below the groundline.

PAH soil extraction procedure

Triplicate 10 g subsamples of each soil sample were extracted and analyzed for PAH content. Soil samples were not dried prior to extraction to help retain volatile PAHs, and they were not ground sieved or otherwise fractionated before extraction. Each 10 g subsample was placed into a pre-weighed 50 mL Falcon tube. Twenty mL of a 2:2:1 acetone: ethyl acetate: isooctane (v/v) mixture was added to each Falcon tube and weighed again. The samples were hand shaken to remove any sediment stuck to the bottom of the tube then sonicated for 5 min. The samples were then treated with a single QuEChERS packet consisting of a salt mixture containing 6 g of magnesium sulfate and 1.5 g of sodium acetate (Agilent Technologies, Santa Clara, CA). After the addition of the QuEChERS packet, the tubes were weighed (after drying the tubes after the initial sonication) and sonicated for another 5 min, followed by 5 min of centrifugation at 5,000 RPM.

All supernatants were transferred to a pre-weighed 20 mL amber glass scintillation vial and weighed to determine solvent recovery on a weight basis. Samples were then concentrated under a gentle stream of house air for approximately 15 min and weighed again. A 1.5 mL aliquot was then transferred to a 2 mL dispersive solid phase extraction (SPE) microcentrifuge tube and sonicated for 5 min. The SPE tube was then centrifuged for 5 min at 5,000 RPM and a final 1 mL aliquot of supernatant was transferred to an amber autosampler vial and frozen until GC-MS analysis. The remaining supernatant in scintillation vials was retained and frozen, should future analysis be necessary.

GC-MS Analysis

Sixteen different PAHs were quantified in each extract using GC-MS. All standards and samples were analyzed using a Shimadzu GCMS-QP2010S GC-MS (Shimadzu, Kyoto, Japan) utilizing selective ion monitoring (SIM) and a Restek DB-5MS column 30.0 m long, 0.25 µmm thick, and 0.25 mm internal diameter (Restek Corp. Bellefonte, PA). Instrument injection was operated in spitless mode with a 3.5 mm glass liner with de-activated glass wool. A 1 µL injection was performed at 275°C. Chromatography of the 16 PAHs of interest was attained at a column flow rate of 2.50 mL/min using HP-5 grade ultra-high purity helium as the carrier gas. Column oven temperature was set to 70°C, held for 2 min, increased to 265°C at a rate of 10.0K/min, and held for 18.5 min for a total run time of 40 min. Mass spectrometer ion source and interface temperature were 225°C and 275°C, respectively, with a solvent cut time of 5 min. If no signal was detected using GC-MS, a value of zero was assigned to the PAH concentration in the extract, and these were included in the calculation of average values shown below.

Calibration curves were generated by preparing standards from a 2000 µg/mL 16-PAH reference standard from Sigma Aldrich (St. Louis, Missouri) in dichloromethane. Concentration of

Table 2. The 16 polycyclic aromatic hydrocarbons (PAHs) measured in this study, with quantification limits for the GC-MS method used. Concentrations are listed for extracts of soil.

PAH name	Quantification limit on instrument (µg/ml)
Naphthalene	0.010
Acenaphthylene	0.010
Acenaphthene	0.010
Fluorene	0.010
Phenanthrene	0.025
Anthracene	0.025
Fluoranthene	0.010
Pyrene	0.010
Benz[a]anthracene	0.075
Chrysene	0.075
Benzo[b]fluoranthene & Benzo[k]fluoranthene	0.025
Benzo[a]pyrene	0.050
Indeno[1,2,3-cd]pyrene	0.100
Benzo[g,h,i]perylene	0.050
Dibenz[a,h]anthracene	0.100

PAH standards prepared from the 2000 µg/mL stock solution were 0.005, 0.01, 0.1, 0.5, and 1.0 µg/mL. Quantification limits based on the lowest reliably detectable standard for each PAH in extracts varied, ranging from 0.01 to 0.1 µg/ml, and are shown in Table 2.

Results and discussion

Concentrations of PAH found in soils around the creosote-treated posts varied widely among the 16 different PAHs of interest, sampling locations, and sampling times. Discernible patterns were sometimes but not always present across these variables for each PAH. PAH concentrations in soil were often highly variable, which made average PAH levels around creosote-treated wood difficult to differentiate statistically from those found around controls at each timepoint. Particularly for the heavier PAHs, frequency of detection among replicate samples was a more useful indicator of relative abundance. In the interest of brevity, 4 of the 16 PAHs are discussed below, which span most of the molecular weight range of the 16 PAHs in the study. These are naphthalene, acenaphthene, chrysene, and benzo [a] pyrene. Concentrations of all 16 PAHs in soil samples analyzed in this study over the 38-mo study period can be found in supplemental Tables S1–S5.

Naphthalene

Naphthalene was found at the highest levels in the background samples taken before installation and in the non-treated control sample 30 cm from the outer surface of the post at 15–30 cm deep in the soil (Figure 3). This suggests that at the time of installation, soils likely had acquired some naphthalene from sources other than creosote. As the field site is in an area that experiences seasonal wildfires, naphthalene could have been deposited from wildfire smoke. Wildfire smoke is a known source of PAHs and their alkylated derivatives in the environment, such as naphthalene, 2-methyl naphthalene, phenanthrene, and retene (Navarro et al. 2019; O'Malley et al. 2024). Naphthalene is also a component of vehicle exhaust, and the initial impulse of naphthalene could have come from the skid steer used to install the posts (Baimatova et al. 2017).

Average naphthalene concentrations in soil trended higher in the 3-mo sampling than in the 6-mo timepoint at all sampling locations (Figure 3). This could be a result of a lingering effect of the 2020 wildfire season at the field site, which was exceptionally intense. Naphthalene in the gaseous phase may have been deposited into the soil in 2020 wildfire smoke and since dissipated over time, either through volatilization (Kim et al. 2011) or biodegradation. Average concentrations of naphthalene found 12- to 38-mo after installation all trended lower than the initial 3- to 6-mo period at all heights and distances from the post surface and were generally identical, with no evident trend of elevated naphthalene concentrations through time.

Naphthalene concentrations in samples taken around controls in the initial 6 mo were similar to those of samples taken around creosote-treated posts, except for the 3-mo sampling, where they were somewhat lower than in samples taken around treated posts. From the 12-mo period onward, average concentrations of naphthalene in controls were consistently lower, apart from the 38-mo timepoint, at 30 cm from the post surface, whereas concentrations in the middle 15–30 cm sample were similar to background control concentrations found prior to installation. This suggests that if creosote is contributing to overall naphthalene concentrations in soils, it does so in an impulse of naphthalene migration within the initial months following installation, and migration remains consistent. This is in line with previous observations of creosote-treated wood exposed to simulated rainfall, where the highest PAH losses resulted from the first volumes of rainfall exposure (Konkler et al. 2020). No obvious trends were present in naphthalene concentrations at the different soil depths and distances.

Another factor that may have contributed to higher naphthalene concentrations at the 3- and 6-mo sampling points is seasonality. The site where this study was performed receives most of its rainfall in the winter months, where soil temperatures

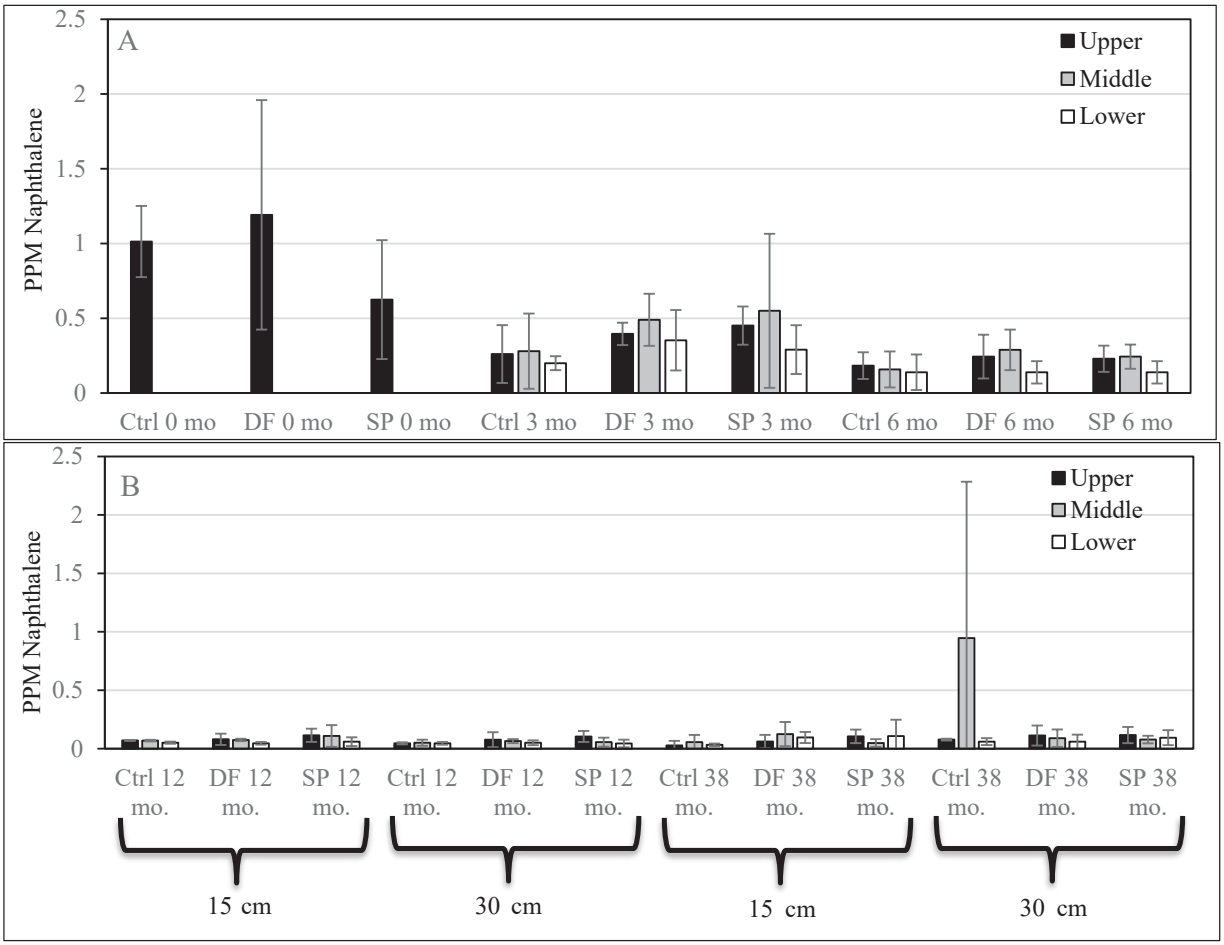


Figure 3. Average naphthalene concentrations (ppm, wet weight basis) found in soils around creosote-treated Douglas-fir (DF) and southern pine (SP) posts at (A) 0–6 mo, 15 cm from the post surface; and (B) 12–38 mo after installation, 15 and 30 cm from the post surface. Soil was sampled at three depths in the soil column: 0–15 cm (upper), 15–30 cm (middle), and 30–46 cm (lower). Error bars are plus or minus one standard deviation.

are lowest as well. The 3- and 6-mo samplings were done in December and March, respectively. The combination of high levels of water runoff and lower microbial metabolism rates of naphthalene in the cooler soils (Coulon et al. 2005) may have contributed to higher naphthalene recovery in these sampling points, as opposed to the 12- and 38-mo sampling points, which occurred in warmer and drier parts of the year.

Acenaphthene

Acenaphthene concentrations in soils were generally lower in the early months of the study compared to naphthalene (Figure 4). Average acenaphthene concentrations 30 cm from the control posts at the 38-mo sampling point were elevated in the middle 15–30 cm soil sample due to high levels around one of the replicate controls, similar to the pattern seen with naphthalene. This suggests that the site has some environmental source or pre-existing acenaphthene that is not attributable to creosote. Trends in acenaphthene migration also differed from naphthalene in that the 12-mo sampling point around southern pine posts showed similar or higher concentrations to the 3-mo sampling point, indicating that PAH migration is either continuing from the posts in the later timepoint or did not dissipate from the initial impulse coming from the treated wood. Samples taken from around southern pine treated posts 15 cm from the post surface had average acenaphthene concentrations that trended higher than levels found in samples taken 30 cm from the post surface. This trend was not as clear around pine posts in soils sampled 38 mo after installation, but a few replicate samples had relatively higher acenaphthene levels at the closer 15-cm sampling point than the 30-cm sampling point around Douglas-fir posts. Overall, the spatial differences were small and acenaphthene levels had a lot of overlap across sampling locations for each post type.

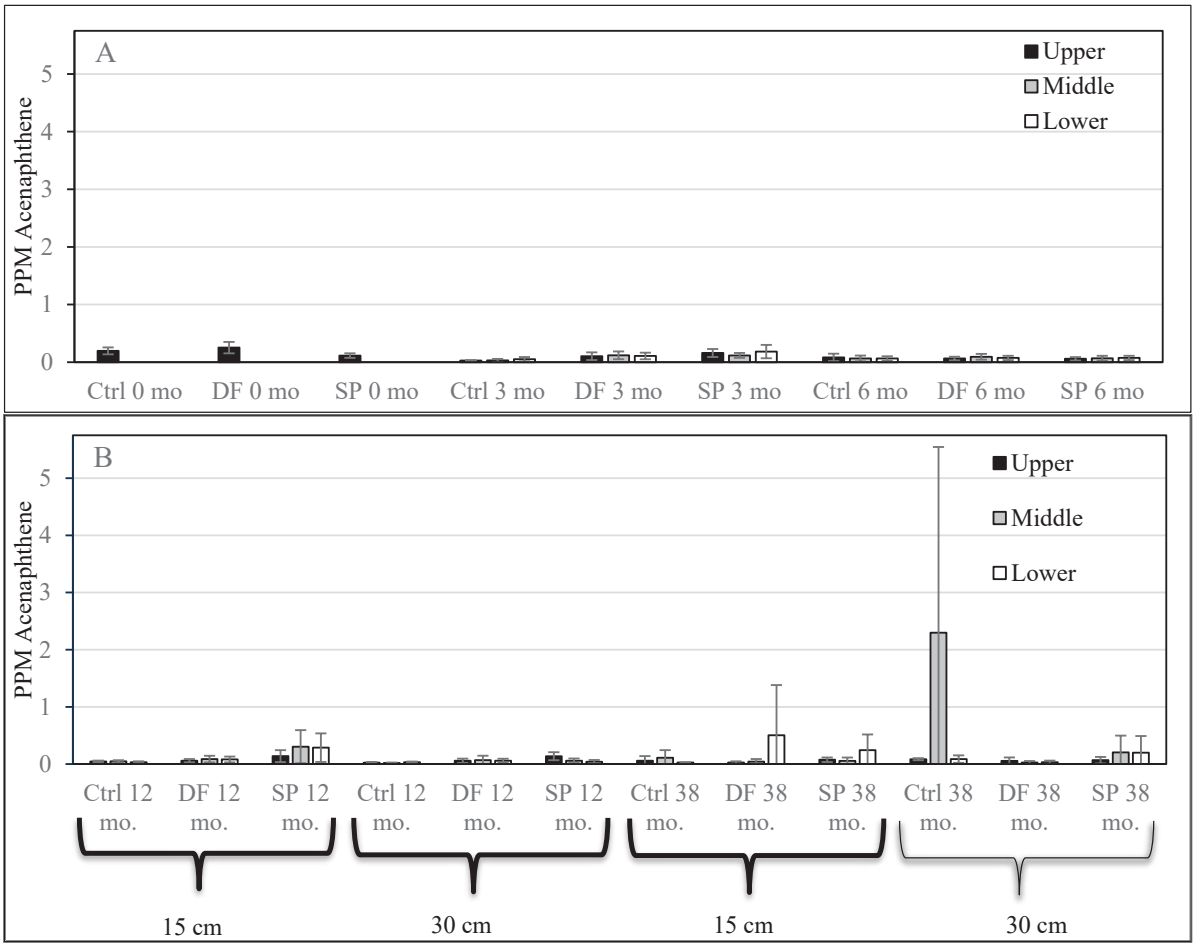


Figure 4. Average acenaphthene concentrations found in soils around creosote-treated Douglas-fir and southern pine posts at (A) 0–6 mo, 15 cm from the post surface; and (B) 12–38 mo after installation, 15 and 30 cm from the post surface. Soil was sampled at three depths in the soil column: 0–15 cm (upper), 15–30 cm (middle), and 30–46 cm (lower). Error bars are plus or minus one standard deviation.

Chrysene

Heavier PAHs such as chrysene (Figure 5) showed a different pattern of migration compared to naphthalene and acenaphthene. Average chrysene levels in background samples were generally similar to those found in controls throughout the sampling period in the first 12 mo. Average chrysene levels in controls remained near the detection limit for replicate samples in the first 12 mo. It was more common to detect chrysene in the samples taken around treated posts in most cases, which resulted in higher average chrysene levels, although levels were very similar around controls and untreated posts in the first 12 mo. Increases of the average chrysene concentration in both Douglas-fir and southern pine posts post 15 cm from the surface were apparent after 38-mo. Average concentrations in southern pine posts 38 mo after installation 15 cm from the post were somewhat sporadic, but higher than Douglas-fir posts, ranging from around 2.0 to 6 ppm. Average concentrations 30 cm from the post in both species trended lower, but similarly, higher average concentrations were found in southern pine posts ranging from around 0.2 ppm to 1.8 ppm. Higher average concentrations found around southern pine posts are perhaps evidence of the higher creosote retention in treated southern pine posts than in Douglas-fir, at 143 kg/m^3 and 52 kg/m^3, respectively, in the 25 mm assay zone.

Benzo [a] pyrene

Another heavy PAH, five ring benzo [a] pyrene (Figure 6) showed a similar migration pattern as chrysene, except that overall average concentrations in soil were generally lower, crossing 0.05 ppm in only two sampling locations/times in treated posts within the first 12 mo of the study. Benzo [a] pyrene was not found 30 cm from the post surfaces, except in one instance, around Douglas-fir posts in the initial 12-mo

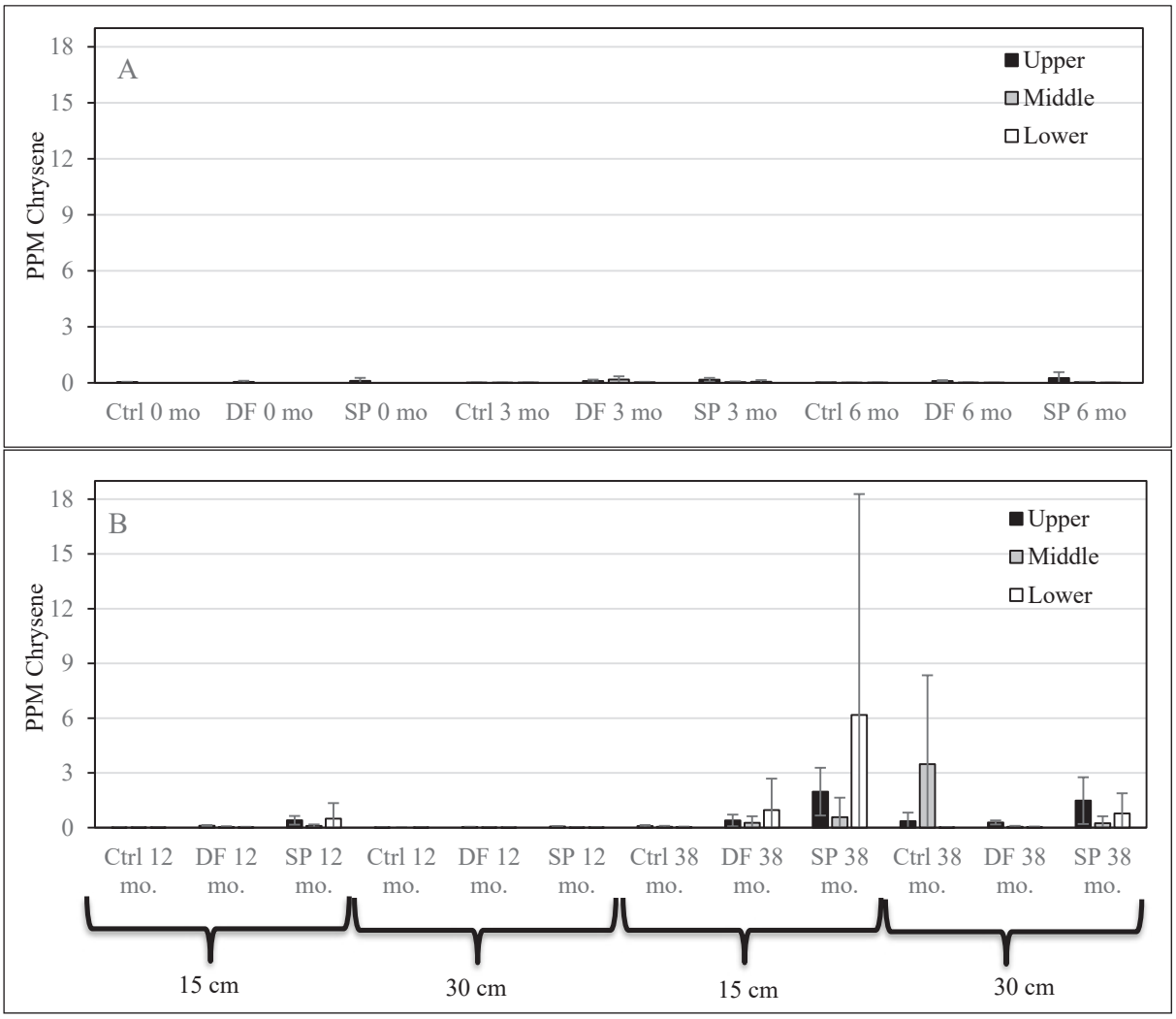


Figure 5. Average chrysene concentrations found in soils around creosote-treated Douglas-fir and southern pine posts at (A) 0–6 mo, 15 cm from the post surface; and (B) 12–38 mo after installation, 15 and 30 cm from the post surface. Soil was sampled at three depths in the soil column: 0–15 cm (upper), 15–30 cm (middle), and 30–46 cm (lower). Error bars are plus or minus one standard deviation.

period. This suggests that migration in the first 12 mo was largely limited to within a 15-cm radius.

An increase in benzo [a] pyrene concentrations in soil was detectable 38 mo after installation. Benzo [a] pyrene concentrations in Douglas-fir posts 15 cm from the post surface were similar to those found in previous sampling periods, except for an increase in the lower 30–46 cm sampled. In the same 38-mo sampling period at 30 cm from the post surface, benzo [a] pyrene concentrations also increased for Douglas-fir posts, but were around concentration levels found in the background and in the 3-mo sampling period. Similarly, an increase in benzo [a] pyrene soil concentrations was apparent after 38-mo in the 0–15 and 30–46 cm of the soil column sampled; however, concentrations were higher in southern pine posts. Benzo [a] pyrene concentrations 15 cm from the post surface in southern pine posts ranged from around 0.4 ppm to around 1.0 ppm after 38 mo, but decreased substantially 30 cm from the post, averaging around 0.1 ppm.

Soil concentrations of all 16 PAHs analyzed in this study over a 38-mo sampling period are shown in Tables S1-S5. Most of the PAHs followed one of the two trends described above for lower and higher molecular weight PAHs. These data can be used to further identify trends in PAH migration from creosote-treated commodities in ground contact. For example, these data show rapidly declining PAH concentrations with increasing distance from roundwood surfaces, even within 30 cm of the wood surface, which suggests near background levels are likely reached only a short distance farther from the posts. Previous

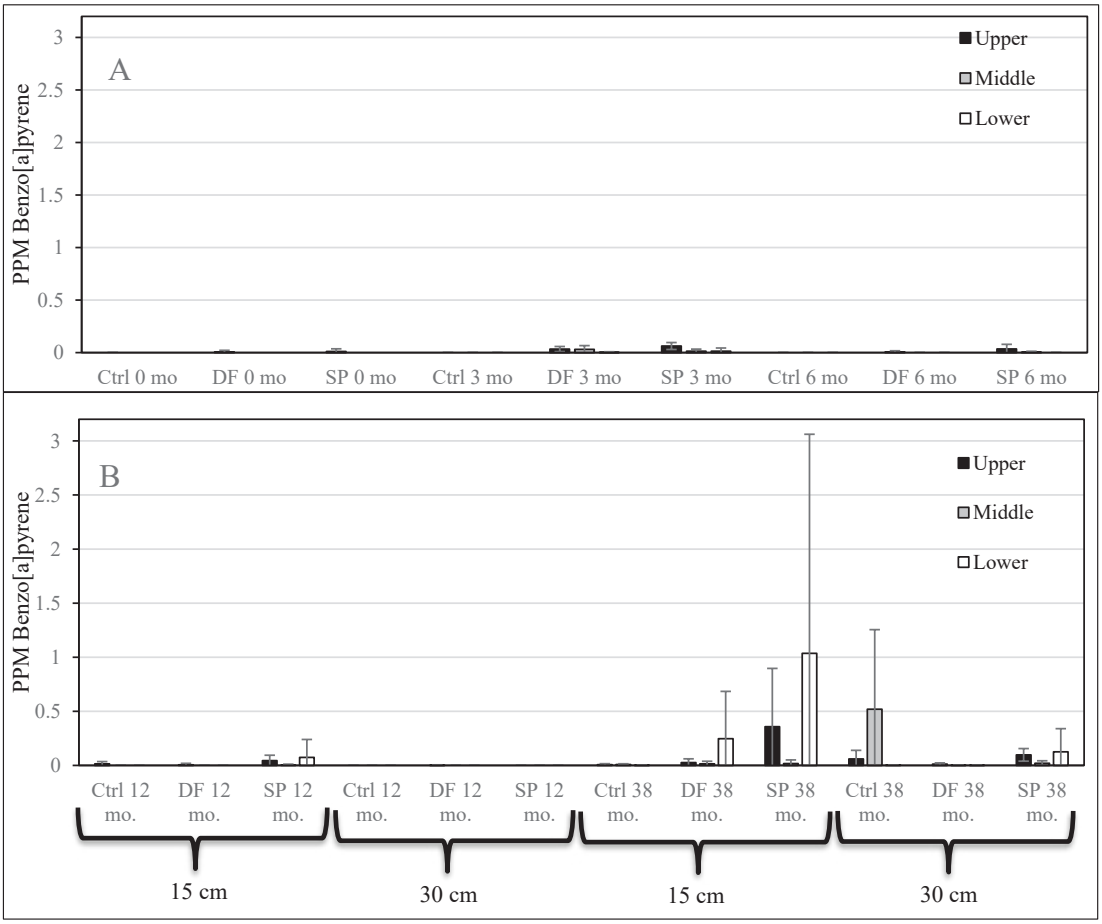


Figure 6. Average benzo [a] pyrene concentrations found in soils around creosote-treated Douglas-fir and southern pine posts at (A) 0–6 mo, 15 cm from the post surface; and (B) 12–38 mo after installation, 15 and 30 cm from the post surface. Soil was sampled at three depths in the soil column: 0–15 cm (upper), 15–30 cm (middle), and 30–46 cm (lower). Error bars are plus or minus one standard deviation.

studies have shown that PAH migration from creosote-treated utility poles was spatially limited, with migration of nearly all of the 13 PAHs assessed limited to within 20 cm of the pole surface (EPRI 1997; NAWPC 2020).

To date, the trends identified show higher initial accumulation of lighter PAHs near the post surfaces, followed by dissipation to background levels or lower. Heavier PAHs show a different pattern where they were found in greater abundance in the latest sampling point, which suggests that mobilization of these chemicals from the post surfaces is slower, reflecting their lower solubility in water. This work provides a better understanding of how creosote-treated roundwood can impact soils and provides utilities with a benchmark to assess the impact of creosote-treated utility poles in the initial years after installation. This study is still in the ground and is continuing to be sampled. Subsequent samplings will expand to a distance of 46 cm from the post surface to attempt to delineate the outer limits of detectable PAH increases around the creosote-treated posts.

Conclusions

PAH migration from Douglas-fir and southern pine posts was highly varied among PAHs over the 38-mo sampling period, and in many cases, concrete patterns were not discernible. Overall, southern pine posts tended to yield higher soil PAH concentrations around the posts due to the higher creosote loading in the species for samples utilized in this study. For some of the lighter PAHs, significant environmental inputs not attributable to creosote were detected at the study start and during the sampling period. This indicates that for those PAHs found in controls or at the initial sampling point, the proportion of PAH originating from creosote versus other environmental inputs could not be quantified.

Lighter PAHs found around creosote-treated posts in some cases showed an initial impulse in the early sampling points that dissipated in magnitude in the later sampling periods. Heavier PAHs showed a different pattern of migration and

were more frequently found around creosote-treated posts, but were detected less often overall across the samples. Some of the heavier PAHs were more often identified among replicate samples taken from soils closer to the post surface, although some were still detected at the more distant sampling point after 38 mo. This study shows a complex migration dynamics among different PAH components that is in part dependent on creosote concentration, distance from the posts, time since installation, and non-creosote environmental inputs.

Acknowledgements

We thank the Creosote Council and their supporting organizations for providing the creosote-treated posts that were used in this study. This work was funded by the Oregon State University Environmental Performance of Treated Wood Research Cooperative.

References

AWPA (2020) A6-20 Standard method for the determination of retention of oil-type preservatives from small samples. American Wood Protection Association, Birmingham, AL.

Baechler RH, Stamm AJ (1954) Wood. I Eng Chem 46(10):2127–2130. https://doi.org/10.1021/ie50538a038

Baimatova N, Koziel JA, Kenessov B (2017) Passive sampling and analysis of naphthalene in internal combustion engine exhaust with retracted SPME Device and GC-MS. Atmosphere 8(7). https://doi.org/10.3390/atmos8070130

Bestari K, Robinson R, Solomon K, Steele T, Day K, Sibley P (1998) Distribution and composition of polycyclic aromatic hydrocarbons within experimental microcosms treated with creosote-impregnated Douglas-fir pilings. Environ Toxicol Chem 17(12):2369–2377. https://doi.org/10.1002/etc.5620171202

Bolin CA, Smith ST (2013) Life Cycle Assessment of Creosote-Treated Wooden Railroad Crossties in the US with Comparisons to Concrete and Plastic Composite Railroad Crossties. 2013. https://doi.org/10.4236/jtts.2013.32015

Brooks K (2004) Polycyclic aromatic hydrocarbon migration from creosote-treated railway ties into ballast and adjacent wetlands (No. FPL−RP−617; p. 53). U.S. Department of Agriculture Forest Service, Forest Products Laboratory.

Brooks K (2020) Preserved Wood Utility Poles and the Environment (Technical Bulletin Nos. 19-E-302; p. 12). North American Wood Pole Council.

Cargouët M, Jeannee N, Vidart B, Gregori P (2018) Polycyclic aromatic hydrocarbon (PAH) levels in environmental media potentially impacted by reused or stored creosote-treated railway ties. Environ Sci Pollut Res 25(18):17409–17424. https://doi.org/10.1007/s11356-018-1910-9

Coulon F, Pelletier E, Gourhant L, Delille D (2005) Effects of nutrient and temperature on degradation of petroleum hydrocarbons in contaminated sub-Antarctic soil. Chemosphere 58(10):1439–1448. https://doi.org/10.1016/j.chemosphere.2004.10.007

Duncan DL, Carls MG, Rice SD, Stekoll MS (2017) The toxicity of creosote-treated wood to Pacific herring embryos and characterization of polycyclic aromatic hydrocarbons near creosoted pilings in Juneau, Alaska. Environ Toxicol Chem 36(5), 1261–1269. https://doi.org/10.1002/etc.3653

Eisler R (1987) Polycyclic aromatic hydrocarbon hazards to fish, wildlife, and invertebrates: A synoptic review (Biological Report 85 No. 11; p. 81). U.S. Fish and Wildlife Service.

Electric Power Research Institute (EPRI). (1997). Pole preservatives in soils adjacent to in-service utility poles in the United States (Report No. TR-108598). https://www.epri.com/research/products/TR-108598.

Gallacher C, Thomas R, Taylor C, Lord R, Kalin RM (2017) Comprehensive composition of Creosote using comprehensive two-dimensional gas chromatography time-of-flight mass spectrometry (GCxGC-TOFMS). Chemosphere 178:34–41. https://doi.org/10.1016/j.chemosphere.2017.03.050

Gewurtz SB, Lazar R, Douglas Haffner G (2000) Comparison of polycyclic aromatic hydrocarbon and polychlorinated biphenyl dynamics in benthic invertebrates of Lake Erie, USA. Environ Toxicol Chem 19(12):2943–2950. https://doi.org/10.1002/etc.5620191215

Goyette D, Brooks KM (1998) Creosote Evaluation: Phase II Sooke Basin Study – Baseline to 535 Days Post Construction 1995–1996. Prepared for the Creosote Evaluation Steering Committee Regional Program, Report PR98-04.

Kang, S-M, Morrell JJ, Simonsen J, Lebow S (2005). Creosote movement from treated wood immersed in fresh water. *Forest Prod J 55*(12):42–46.

Kim EJ, Choi S-D, Chang Y-S (2011) Levels and patterns of polycyclic aromatic hydrocarbons (PAHs) in soils after forest fires in South Korea. Environ Sci Pollut Res 18(9):1508–1517. https://doi.org/10.1007/s11356-011-0515-3

Konkler MJ, Cappellazzi J, Presley G, Morrell JJ (2020) Migration of creosote components from timbers treated with creosote and processed using Best Management Practices. J Environ Manag 276. https://doi.org/10.1016/j.jenvman.2020.111270

Moret S, Purcaro G, Conte LS (2007) Polycyclic aromatic hydrocarbon (PAH) content of soil and olives collected in areas contaminated with creosote released from old railway ties. Sci Total Environ 386(1):1–8. https://doi.org/10.1016/j.scitotenv.2007.07.008

Mueller JG, Chapman PJ, Pritchard PH (1989). Creosote-contaminated sites. Their potential for bioremediation. Environ Sci Technol 23(10):1197–1201. https://doi.org/10.1021/es00068a003

Murphy BL, Brown J (2005) Environmental forensics aspects of PAHs from wood treatment with creosote compounds. Environ Forensics 6(2):151–159. https://doi.org/10.1080/15275920590952829

Navarro KM, Cisneros R, Schweizer D, Chowdhary P, Noth EM, Balmes JR, Hammond SK (2019) Incident command post exposure to polycyclic aromatic hydrocarbons and particulate matter during a wildfire. J Occup Environ Hyg 16(11):735–744. https://doi.org/10.1080/15459624.2019.1657579

Nestler FH Max (1974) Characterization of wood-preserving coal-tar creosote by gas-liquid chromatography. Anal Chem 46(1):46–53. https://doi.org/10.1021/ac60337a008

North American Wood Pole Council (NAWPC). (2020). Preserved wood utility poles and the environment (Technical Bulletin No. 19-E-302). https://woodpoles.org/wp-content/uploads/TB_Pole_Enviro.pdf

O'Malley KE, Ghetu CC, Rohlman D, Anderson KA (2024) Assessing wildfire impact on diffusive flux of parent and alkylated PAHs: A pilot study of soil-air chemical movement before, during, and after wildfires. Environ Sci Technol 58(52):23117–23126. https://doi.org/10.1021/acs.est.4c09139

RTA (2025) Questions About the Railway Tie Association. Railway Tie Association. https://www.rta.org/faq

Shupe, T. F., Hse, C. Y., & Roliadi, H. (2006). Removal of creosote from wood particles at different horizontal and vertical locations of decommissioned poles using steam treatment. *Wood and Fiber Science, 38*(2), 345–350

US EPA (1981) Priority Pollutant List. 40 CFR Part 423, Appendix A

Vlosky RP (2009, February 16). Statistical Overview of the U.S. Wood Preserving Industry: 2007. Louisiana Forest Products Development Center, Louisiana State University Agricultural Center, Baton Rouge. https://www.researchgate.net/publication/343921608_STATISTICAL_OVERVIEW_OF_THE_US_WOOD_PRESERVING_INDUSTRY_2007

Webster, P.D. 1992. The Wood Crosstie, A 150 Year Success Story: The Railway Tie Association & the National Association of Railroad Tie Producers, A Three-Quarters of a Century History. Railway Tie Association, Gulf Shores, AL. 272 p.

Wilson S, Jones K (1993) Bioremediation of soil contaminated with polynuclear aromatic-hydrocarbons (PAHS)—A Review. Environ Pollut 81(3):229–249. https://doi.org/10.1016/0269-7491(93)90206-4

Appendix: Supplemental data

Table S1. Average concentrations of 16 polycyclic aromatic hydrocarbons measured in this study in soils isolated from post holes dug for the installation of creosote-treated Douglas-fir and southern pine posts, as well as untreated Douglas-fir control posts at the beginning of this study.

Naphthalene concentration (ppb)[a]		
Post type to be installed (species)	Creosote treatment [b]	Post hole (background)
Douglas-fir	−	1013.4 (238.1)
Douglas-fir	+	1191.9 (767.5)
Southern pine	+	624.9 (397.6)
Acenaphthylene concentration (ppb)[a]		
Species	Creosote	Post hole (background)
Douglas-fir	−	0.0 (0.0)
Douglas-fir	+	0.1 (0.1)
Southern pine	+	0.0 (0.0)
Acenaphthene concentration (ppb)[a]		
Species	Creosote	Post hole (background)
Douglas-fir	−	196.7 (60.0)
Douglas-fir	+	252.5 (98.9)
Southern pine	+	114.9 (39.5)
Fluorene concentration (ppb)[a]		
Species	Creosote	Post hole (background)
Douglas-fir	−	49.2 (14.9)
Douglas-fir	+	69.6 (24.3)
Southern pine	+	48.6 (36.9)
Phenanthrene concentration (ppb)[a]		
Species	Creosote	Post hole (background)
Douglas-fir	−	58.6 (6.7)
Douglas-fir	+	53.1 (51.6)
Southern pine	+	75.7 (85.0)
Anthracene concentration (ppb)[a]		
Species	Creosote	Post hole (background)
Douglas-fir	−	23.9 (3.8)
Douglas-fir	+	18.4 (19.2)
Southern pine	+	41.9 (66.3)
Fluoranthene concentration (ppb)[a]		
Species	Creosote	Post hole (background)
Douglas-fir	−	54.9 (3.3)
Douglas-fir	+	57.4 (37.0)
Southern pine	+	92.0 (93.5)

Pyrene concentration (ppb)[a]		
Species	Creosote	Post hole (background)
Douglas-fir	−	36.0 (3.9)
Douglas-fir	+	37.2 (21.6)
Southern pine	+	57.8 (59.9)
Benz[a]anthracene concentration (ppb)[a]		
Species	Creosote	Post hole (background)
Douglas-fir	−	26.3 (1.4)
Douglas-fir	+	20.3 (11.7)
Southern pine	+	32.8 (32.4)
Chrysene concentration (ppb)[a]		
Species	Creosote	Post hole (background)
Douglas-fir	−	44.4 (12.6)
Douglas-fir	+	47.5 (64.3)
Southern pine	+	103.3 (164.0)
Benzo[b + k] fluoranthene concentration (ppb)[a]		
Species	Creosote	Post hole (background)
Douglas-fir	−	44.4 (12.6)
Douglas-fir	+	47.5 (64.3)
Southern pine	+	103.3 (164.0)
Benzo[a]pyrene concentration (ppb)[a]		
Species	Creosote	Post hole (background)
Douglas-fir	−	0.0 (0.0)
Douglas-fir	+	6.7 (15.0)
Southern pine	+	11.1 (24.9)
Indeno[1,2,3-cd]pyrene concentration (ppb)[a]		
Species	Creosote	Post hole (background)
Douglas-fir	−	0.0 (0.0)
Douglas-fir	+	8.7 (19.4)
Southern pine	+	0.0 (0.0)
Benzo[g,h,i]perylene concentration (ppb)[a]		
Species	Creosote	Post hole (background)
Douglas-fir	−	0.0 (0.0)
Douglas-fir	+	8.3 (18.6)
Southern pine	+	0.0 (0.0)
Dibenz[a,h]anthracene concentration (ppb)[a]		
Species	Creosote	Post hole (background)
Douglas-fir	–	29.3 (41.4)
Douglas-fir	+	9.4 (20.9)
Southern pine	+	0.0 (0.0)

[a]Values are means of three replicate samples with one standard deviation in parentheses.
[b]Untreated posts indicated with − ; creosote treated posts indicated with + .

Table S2. Average concentrations of 16 polycyclic aromatic hydrocarbons measured in this study found in soils around creosote-treated Douglas-fir and southern pine posts 3 mo after post installation. Soil was collected 15 cm from the post surface and at three depths in the soil column: 0–15 cm (upper), 15–30 cm (middle), and 30–46 cm (lower). Standard deviations for five replicate soil samples around treated posts and two replicate extracts around untreated posts are also shown.

Naphthalene concentration (ppb)[a]				
Species	Creosote	Soil sampling depth		
		0–15 cm	15–30 cm	30–45 cm
Douglas-fir	−	260.7 (193.4)	280.0 (251.7)	199.5 (46.6)
Douglas-fir	+	395.6 (74.8)	489.8 (174.2)	352.9 (202.1)
Southern pine	+	451.0 (127.8)	549.9 (515.2)	290.4 (163.2)
Acenaphthylene concentration (ppb)[a]				
Species	Creosote	Soil sampling depth		
		0–15 cm	15–30 cm	30–45 cm
Douglas-fir	−	0.0 (0.0)	0.0 (0.0)	0.0 (0.0)
Douglas-fir	+	0.0 (0.1)	0.1 (0.1)	0.0 (0.0)
Southern pine	+	0.1 (0.1)	0.1 (0.1)	0.2 (0.1)
Acenaphthene concentration (ppb)[a]				
Species	Creosote	Soil sampling depth		
		0–15 cm	15–30 cm	30–45 cm
Douglas-fir	−	29.3 (3.4)	31.8 (25.3)	52.5 (37.5)
Douglas-fir	+	104.2 (66.7)	119.2 (67.7)	108.0 (57.2)
Southern pine	+	159.5 (69.5)	117.9 (42.6)	184.3 (115.9)
Fluorene concentration (ppb)[a]				
Species	Creosote	Soil sampling depth		
		0–15 mm	15–30 cm	30–45 cm
Douglas-fir	−	13.0 (4.3)	9.5 (5.9)	16.0 (13.7)
Douglas-fir	+	45.7 (21.0)	53.3 (27.9)	34.2 (17.6)
Southern pine	+	84.3 (33.2)	40.4 (8.9)	79.0 (71.8)
Phenanthrene concentration (ppb)[a]				
Species	Creosote	Soil sampling depth		
		0–15 cm	15–30 cm	30–45 cm
Douglas-fir	−	11.8 (6.5)	5.8 (2.4)	11.7 (9.7)
Douglas-fir	+	117.7 (53.2)	128.6 (90.6)	41.0 (33.1)
Southern pine	+	168.0 (80.5)	59.3 (60.0)	84.7 (87.7)
Anthracene concentration (ppb)[a]				
Species	Creosote	Soil sampling depth		
		0–15 cm	15–30 cm	30–45 cm
Douglas-fir	−	3.4 (4.8)	3.8 (1.6)	3.8 (3.6)
Douglas-fir	+	404.8 (512.3)	299.1 (595)	273.2 (648.1)
Southern pine	+	30.3 (17.3)	13.5 (14.1)	16.5 (15.8)
Fluoranthene concentration (ppb)[a]				
Species	Creosote	Soil sampling depth		
		0–15 cm	15–30 cm	30–45 cm
Douglas-fir	−	33.9 (15.1)	27.5 (7.8)	32.0 (7.1)
Douglas-fir	+	327.0 (141.2)	347.5 (268.4)	108.5 (66.7)
Southern pine	+	430.7 (200.1)	165.4 (180.0)	136.0 (158.6)

[a]Values are means of three replicate samples with one standard deviation in parentheses.

Table S2 (*continued*). Average concentrations of 16 polycyclic aromatic hydrocarbons measured in this study found in soils around creosote-treated Douglas-fir and southern pine posts 3 mo after post installation.

Pyrene concentration (ppb)[a]				
Species	Creosote	Soil sampling depth		
		0–15 cm	15–30 cm	30–45 cm
Douglas-fir	−	14.3 (11.0)	12.1 (2.7)	21.4 (3.8)
Douglas-fir	+	195.7 (83.0)	207.8 (158.8)	69.0 (39.8)
Southern pine	+	265.2 (122.9)	104.9 (107.7)	85.5 (95.9)
Benz[a]anthracene concentration (ppb)[a]				
Species	Creosote	Soil sampling depth		
		0–15 cm	15–30 cm	30–45 cm
Douglas-fir	−	12.9 (6.1)	10.9 (3.5)	12.0 (1.3)
Douglas-fir	+	51.8 (19.5)	71.9 (60.1)	20.0 (12.4)
Southern pine	+	85.1 (51.6)	26.4 (18.1)	29.1 (29.3)
Chrysene concentration (ppb)[a]				
Species	Creosote	Soil sampling depth		
		0–15 cm	15–30 cm	30–45 cm
Douglas-fir	−	10.1 (12.1)	6.3 (3.8)	10.2 (7.3)
Douglas-fir	+	95.3 (78.4)	174.5 (174.6)	29.3 (26.7)
Southern pine	+	166.6 (100.1)	38.6 (38.1)	56.8 (92.0)
Benzo[j] and [k] fluoranthene concentration (ppb)[a]				
Species	Creosote	Soil sampling depth		
		0–15 cm	15–30 cm	30–45 cm
Douglas-fir	−	10.1 (12.1)	6.3 (3.8)	10.2 (7.3)
Douglas-fir	+	95.3 (78.4)	174.5 (174.6)	29.3 (26.7)
Southern pine	+	166.6 (100.1)	38.6 (38.1)	56.8 (92.0)
Benzo[a]pyrene concentration (ppb)[a]				
Species	Creosote	Soil sampling depth		
		0–15 cm	15–30 cm	30–45 cm
Douglas-fir	−	0.0 (0.0)	0.0 (0.0)	0.0 (0.0)
Douglas-fir	+	34.0 (24.3)	30.2 (36.3)	2.5 (5.6)
Southern pine	+	62.7 (33.1)	13.6 (19.7)	13.5 (30.3)
Indeno[1,2,3-cd]pyrene concentration (ppb)[a]				
Species	Creosote	Soil sampling depth		
		0–15 cm	15–30 cm	30–45 cm
Douglas-fir	−	0.0 (0.0)	0.0 (0.0)	0.0 (0.0)
Douglas-fir	+	0.0 (0.0)	14.4 (19.8)	0.0 (0.0)
Southern pine	+	9.1 (20.4)	0.0 (0.0)	0.0 (0.0)
Benzo[g,h,i]perylene concentration (ppb)[a]				
Species	Creosote	Soil sampling depth		
		0–15 cm	15–30 cm	30–45 cm
Douglas-fir	−	0.0 (0.0)	0.0 (0.0)	0.0 (0.0)
Douglas-fir	+	0.0 (0.0)	9.7 (13.3)	0.0 (0.0)
Southern pine	+	7.9 (17.6)	0.0 (0.0)	0.0 (0.0)
Dibenz[a,h]anthracene concentration (ppb)[a]				
Species	Creosote	Soil sampling depth		
		0–15 cm	15–30 cm	30–45 cm
Douglas-fir	−	0.0 (0.0)	0.0 (0.0)	0.0 (0.0)
Douglas-fir	+	0.0 (0.0)	0.0 (0.0)	0.0 (0.0)
Southern pine	+	7.3 (16.4)	0.0 (0.0)	0.0 (0.0)

[a]Values are means of three replicate samples with one standard deviation in parentheses.

Table S3. Concentrations of 16 polycyclic aromatic hydrocarbons measured in this study found in soils around creosote-treated Douglas-fir and southern pine posts 6 mo after post installation. Soil was collected 15 cm from the post surface and at three depths in the soil column: 0–15 cm (upper), 15–30 cm (middle), and 30–46 cm (lower). Standard deviations for five replicate soil samples around treated posts and two replicate extracts around untreated posts are also shown.

Naphthalene concentration (ppb)[a]				
Species	Creosote	Soil sampling depth		
		0–15 cm	15–30 cm	30–45 cm
Douglas-fir	−	183.1 (89.3)	157.8 (120.3)	139.0 (119.0)
Douglas-fir	+	243.8 (146.5)	288.6 (135.7)	138.3 (74.7)
Southern pine	+	229.2 (87.7)	243.3 (80.8)	138.3 (74.7)
Acenaphthylene concentration (ppb)[a]				
Species	Creosote	Soil sampling depth		
		0–15 cm	15–30 cm	30–45 cm
Douglas-fir	−	0.0 (0.0)	0.0 (0.0)	0.0 (0.0)
Douglas-fir	+	0.0 (0.0)	0.0 (0.0)	0.0 (0.0)
Southern pine	+	0.1 (0.1)	0.0 (0.0)	0.0 (0.0)
Acenaphthene concentration (ppb)[a]				
Species	Creosote	Soil sampling depth		
		0–15 cm	15–30 cm	30–45 cm
Douglas-fir	−	84.1 (63.6)	65.4 (49.9)	64.4 (38.3)
Douglas-fir	+	63.7 (31.2)	94.2 (49.9)	74.2 (37.5)
Southern pine	+	58.9 (29.2)	68.2 (42.7)	74.2 (37.5)
Fluorene concentration (ppb)[a]				
Species	Creosote	Soil sampling depth		
		0–15 cm	15–30 cm	30–45 cm
Douglas-fir	−	30.8 (8.7)	14.6 (12.1)	20.6 (13.6)
Douglas-fir	+	25.9 (19.4)	20.8 (10.7)	17.4 (12.3)
Southern pine	+	65.0 (91.1)	18.7 (8.8)	17.4 (12.3)
Phenanthrene concentration (ppb)[a]				
Species	Creosote	Soil sampling depth		
		0–15 cm	15–30 cm	30–45 cm
Douglas-fir	−	35.2 (25.2)	12.6 (6.7)	25.7 (21.6)
Douglas-fir	+	65.1 (10.0)	18.5 (7.2)	12.2 (4.0)
Southern pine	+	153.7 (147.6)	26.9 (12.9)	12.2 (4.0)
Anthracene concentration (ppb)[a]				
Species	Creosote	Soil sampling depth		
		0–15 cm	15–30 cm	30–45 cm
Douglas-fir	−	6.6 (9.4)	0.0 (0.0)	3.3 (4.7)
Douglas-fir	+	36.1 (26.2)	0.9 (2.1)	3.1 (4.7)
Southern pine	+	140.1 (260.4)	8.7 (7.9)	3.1 (4.7)
Fluoranthene concentration (ppb)[a]				
Species	Creosote	Soil sampling depth		
		0–15 cm	15–30 cm	30–45 cm
Douglas-fir	−	44.8 (22.0)	25.9 (6.2)	54.2 (42.0)
Douglas-fir	+	251.4 (140.1)	67.3 (55.0)	26.5 (6.3)
Southern pine	+	437.3 (428.4)	108.9 (109.5)	26.5 (6.3)

[a]Values are means of three replicate samples with one standard deviation in parentheses.

Table S3 (*continued*). Concentrations of 16 polycyclic aromatic hydrocarbons measured in this study found in soils around creosote-treated Douglas-fir and southern pine posts 6 mo after post installation. Soil was collected 15 cm from the post surface and at three depths in the soil column: 0–15 cm (upper), 15–30 cm (middle), and 30–46 cm (lower).

Pyrene concentration (ppb)[a]				
Species	Creosote	Soil sampling depth		
		0–15 cm	15–30 cm	30–45 cm
Douglas-fir	−	27.6 (10.6)	14.7 (0.1)	39.5 (45.7)
Douglas-fir	+	162.9 (84.3)	41.7 (29.7)	12.9 (10.6)
Southern pine	+	311.8 (302.3)	74.1 (73.8)	12.9 (10.6)
Benz[a]anthracene concentration (ppb)[a]				
Species	Creosote	Soil sampling depth		
		0–15 cm	15–30 cm	30–45 cm
Douglas-fir	−	25.6 (8.2)	25.4 (4.4)	27.9 (5.8)
Douglas-fir	+	105.4 (27.1)	198.8 (182.5)	30.0 (20.7)
Southern pine	+	148.0 (124.0)	54.1 (45.3)	30.0 (20.7)
Chrysene concentration (ppb)[a]				
Species	Creosote	Soil sampling depth		
		0–15 cm	15–30 cm	30–45 cm
Douglas-fir	−	22.9 (9.5)	4.9 (6.9)	9.6 (13.5)
Douglas-fir	+	95.1 (49.4)	11.8 (17.8)	2.5 (3.5)
Southern pine	+	253.2 (320.8)	31.9 (24.9)	2.5 (3.5)
Benzo[j] and [k] fluoranthene concentration (ppb)[a]				
Species	Creosote	Soil sampling depth		
		0–15 cm	15–30 cm	30–45 cm
Douglas-fir	−	22.9 (9.5)	4.9 (6.9)	9.6 (13.5)
Douglas-fir	+	95.1 (49.4)	11.8 (17.8)	2.5 (3.5)
Southern pine	+	253.2 (320.8)	31.9 (24.9)	2.5 (3.5)
Benzo[a]pyrene concentration (ppb)[a]				
Species	Creosote	Soil sampling depth		
		0–15 mm	15–30 cm	30–45 cm
Douglas-fir	−	0.0 (0.0)	0.0 (0.0)	0.0 (0.0)
Douglas-fir	+	7.3 (10.1)	0.0 (0.0)	0.0 (0.0)
Southern pine	+	34.7 (44.2)	3.9 (8.8)	0.0 (0.0)
Indeno[1,2,3-cd]pyrene concentration (ppb)[a]				
Species	Creosote	Soil sampling depth		
		0–15 cm	15–30 cm	30–45 cm
Douglas-fir	−	0.0 (0.0)	0.0 (0.0)	0.0 (0.0)
Douglas-fir	+	5.5 (12.3)	0.0 (0.0)	0.0 (0.0)
Southern pine	+	35.9 (57.6)	4.0 (9.0)	0.0 (0.0)
Benzo[g,h,i]perylene concentration (ppb)[a]				
Species	Creosote	Soil sampling depth		
		0–15 cm	15–30 cm	30–45 cm
Douglas-fir	−	0.0 (0.0)	0.0 (0.0)	0.0 (0.0)
Douglas-fir	+	0.0 (0.0)	0.0 (0.0)	0.0 (0.0)
Southern pine	+	10.8 (24.1)	0.0 (0.0)	0.0 (0.0)
Dibenz[a,h]anthracene concentration (ppb)[a]				
Species	Creosote	Soil sampling depth		
		0–15 cm	15–30 cm	30–45 cm
Douglas-fir	−	0.0 (0.0)	0.0 (0.0)	0.0 (0.0)
Douglas-fir	+	0.0 (0.0)	0.0 (0.0)	0.0 (0.0)
Southern pine	+	0.0 (0.0)	0.0 (0.0)	0.0 (0.0)

[a]Values are means of three replicate samples with one standard deviation in parentheses.

Table S4. Concentrations of 16 polycyclic aromatic hydrocarbons measured in this study found in soils around creosote-treated Douglas-fir and southern pine posts 12 mo after post installation. Soil was collected 15 cm from the post surface and at three depths in the soil column: 0–15 cm (upper), 15–30 cm (middle), and 30–46 cm (lower). Standard deviations for five replicate soil samples around treated posts and two replicate extracts around untreated posts are also shown.

Naphthalene concentration (ppb)[a]							
Species	Creosote	Soil sampling depth (15 cm away)			Soil sampling depth (30 cm away)		
		0–15 cm	15–30 cm	30–45 cm	0–15 cm	15–30 cm	30–45 cm
Douglas-fir	−	70.2 (4.1)	68.9 (7.0)	51.4 (9.0)	45.9 (8.7)	50.8 (26.2)	45.5 (11.4)
Douglas-fir	+	80.1 (48.4)	74.7 (9.9)	45.9 (11.2)	76.8 (64.1)	64.6 (17.1)	50.7 (20.6)
Southern pine	+	114.6 (56.5)	108.5 (93.0)	59.8 (37.3)	104.3 (47.2)	55.6 (38.6)	44.3 (33.0)
Acenaphtylene concentration (ppb)[a]							
Species	Creosote	Soil sampling depth (15 cm away)			Soil sampling depth (30 cm away)		
		0–15 cm	15–30 cm	30–45 cm	0–15 cm	15–30 cm	30–45 cm
Douglas-fir	−	0.0 (0.0)	0.0 (0.0)	0.0 (0.0)	0.0 (0.0)	0.0 (0.0)	0.0 (0.0)
Douglas-fir	+	10.7 (17.6)	19.5 (21.4)	13.4 (12.5)	10.3 (14.5)	14.3 (21.2)	10.9 (9.1)
Southern pine	+	30.1 (14.2)	37.0 (21.9)	26.5 (17.9)	33.6 (20.6)	16.9 (12.8)	10.6 (13.5)
Acenaphthene concentration (ppb)[a]							
Species	Creosote	Soil sampling depth (15 cm away)			Soil sampling depth (30 cm away)		
		0–15 cm	15–30 cm	30–45 cm	0–15 cm	15–30 cm	30–45 cm
Douglas-fir	−	44.1 (16.4)	48.7 (18.6)	30.7 (17.4)	25.2 (10.9)	18.9 (8.4)	30.8 (12.7)
Douglas-fir	+	59.2 (28.7)	86.5 (58.4)	80.2 (51.3)	57.1 (37.8)	67.6 (78.0)	58.7 (34.4)
Southern pine	+	138.9 (104.4)	303.8 (289.4)	286.4 (250.1)	137.4 (70.2)	57.6 (40.0)	38.5 (33.1)
Fluorene concentration (ppb)[a]							
Species	Creosote	Soil sampling depth (15 cm away)			Soil sampling depth (30 cm away)		
		0–15 cm	15–30 cm	30–45 cm	0–15 cm	15–30 cm	30–45 cm
Douglas-fir	−	48.7 (1.3)	45.4 (11.1)	28.6 (12.9)	20.5 (12.4)	15.3 (5.2)	20.0 (10.9)
Douglas-fir	+	44.4 (12.0)	61.9 (39.0)	76.4 (63.6)	37.3 (15.0)	60.8 (83.8)	47.0 (44.2)
Southern pine	+	67.4 (21.1)	209.6 (133.5)	355.0 (372.4)	83.8 (44.1)	42.6 (27.6)	32.7 (20.7)
Phenanthrene concentration (ppb)[a]							
Species	Creosote	Soil sampling depth (15 cm away)			Soil sampling depth (30 cm away)		
		0–15 cm	15–30 cm	30–45 cm	0–15 cm	15–30 cm	30–45 cm
Douglas-fir	−	50.1 (9.3)	32.3 (9.0)	30.6 (5.8)	35.6 (16.4)	30.6 (9.0)	18.8 (26.7)
Douglas-fir	+	70.4 (18.6)	112.5 (119.3)	349.2 (472.1)	47.1 (11.8)	110.6 (185.8)	61.1 (70.0)
Southern pine	+	178.0 (70.0)	323.3 (231.9)	1402.2 (2139.8)	92.0 (31.5)	33.0 (9.8)	33.4 (16.1)
Anthracene concentration (ppb)[a]							
Species	Creosote	Soil sampling depth (15 cm away)			Soil sampling depth (30 cm away)		
		0–15 cm	15–30 cm	30–45 cm	0–15 cm	15–30 cm	30–45 cm
Douglas-fir	−	3.3 (4.6)	0.0 (0.0)	4.0 (5.6)	0.0 (0.0)	0.0 (0.0)	0.0 (0.0)
Douglas-fir	+	8.2 (6.8)	6.5 (6.9)	14.8 (12.8)	1.7 (1.5)	1.6 (3.5)	1.3 (1.9)
Southern pine	+	20.3 (5.8)	21.1 (16.5)	114.0 (145.6)	5.3 (7.2)	2.1 (4.6)	0.6 (1.3)
Flouranthene concentration (ppb)[a]							
Species	Creosote	Soil sampling depth (15 cm away)			Soil sampling depth (30 cm away)		
		0–15 cm	15–30 cm	30–45 cm	0–15 cm	15–30 cm	30–45 cm
Douglas-fir	−	63.3 (9.8)	23.3 (32.9)	37.3 (7.7)	35.6 (15.8)	33.1 (15.1)	17.3 (24.4)
Douglas-fir	+	168.3 (37.8)	104.9 (44.3)	158.3 (147.9)	71.3 (16.5)	39.3 (13.0)	33.5 (22.7)
Southern pine	+	441.7 (200.0)	178.3 (110.0)	1714.1 (3341.8)	130.1 (57.6)	36.6 (12.1)	44.9 (27.6)

[a]Values are means of three replicate samples with one standard deviation in parentheses.

Table S4 (*continued*). Concentrations of 16 polycyclic aromatic hydrocarbons measured in this study found in soils around creosote-treated Douglas-fir and southern pine posts 12 mo after post installation. Soil was collected 15 cm from the post surface and at three depths in the soil column: 0–15 cm (upper), 15–30 cm (middle), and 30–46 cm (lower).

Pyrene concentration (ppb)[a]							
Species	Creosote	Soil sampling depth (15 cm away)			Soil sampling depth (30 cm away)		
		0–15 cm	15–30 cm	30–45 cm	0–15 cm	15–30 cm	30–45 cm
Douglas-fir	−	54.0 (4.2)	21.6 (30.5)	29.9 (11.7)	25.5 (16.4)	29.9 (15.7)	10.2 (14.4)
Douglas-fir	+	115.3 (22.0)	74.8 (27.3)	102.0 (90.5)	52.6 (12.1)	31.6 (8.1)	18.2 (18.9)
Southern pine	+	312.1 (143.2)	121.5 (72.6)	1173.3 (2285.9)	96.4 (42.2)	28.1 (10.8)	30.5 (22.3)
Benz[a]anthracene concentration (ppb)[a]							
Species	Creosote	Soil sampling depth (15 cm away)			Soil sampling depth (30 cm away)		
		0–15 cm	15–30 cm	30–45 cm	0–15 cm	15–30 cm	30–45 cm
Douglas-fir	−	11.1 (15.7)	8.8 (12.5)	2.1 (3.0)	6.2 (8.7)	0.0 (0.0)	1.9 (2.7)
Douglas-fir	+	31.2 (10.7)	13.9 (13.5)	6.3 (9.5)	14.2 (2.2)	0.6 (1.4)	1.4 (3.2)
Southern pine	+	106.3 (69.8)	26.3 (18.4)	550.8 (1162.6)	24.2 (18.8)	2.0 (3.0)	3.7 (6.4)
Chrysene concentration (ppb)[a]							
Species	Creosote	Soil sampling depth (15 cm away)			Soil sampling depth (30 cm away)		
		0–15 cm	15–30 cm	30–45 cm	0–15 cm	15–30 cm	30–45 cm
Douglas-fir	−	9.0 (2.7)	3.2 (4.5)	0.9 (1.3)	6.8 (9.5)	0.0 (0.0)	3.6 (5.0)
Douglas-fir	+	100.7 (42.5)	33.8 (43.1)	24.1 (22.6)	35.0 (10.8)	1.4 (1.9)	9.0 (20.2)
Southern pine	+	401.7 (238.7)	95.3 (80.1)	490.4 (854.6)	59.1 (31.8)	4.7 (3.6)	10.6 (21.9)
Benzo[j] and [k] fluoranthene concentration (ppb)[a]							
Species	Creosote	Soil sampling depth (15 cm away)			Soil sampling depth (30 cm away)		
		0–15 cm	15–30 cm	30–45 cm	0–15 cm	15–30 cm	30–45 cm
Douglas-fir	−	9.0 (2.7)	3.2 (4.5)	0.9 (1.3)	6.8 (9.5)	0.0 (0.0)	3.6 (5.0)
Douglas-fir	+	100.7 (42.5)	33.8 (43.1)	24.1 (22.6)	35.0 (10.8)	1.4 (1.9)	9.0 (20.2)
Southern pine	+	401.7 (238.7)	95.3 (80.1)	490.4 (854.6)	59.1 (31.8)	4.7 (3.6)	10.6 (21.9)
Benzo[a]pyrene concentration (ppb)[a]							
Species	Creosote	Soil sampling depth (15 cm away)			Soil sampling depth (30 cm away)		
		0–15 cm	15–30 cm	30–45 cm	0–15 cm	15–30 cm	30–45 cm
Douglas-fir	−	14.7 (20.8)	0.0 (0.0)	0.0 (0.0)	0.0 (0.0)	0.0 (0.0)	0.0 (0.0)
Douglas-fir	+	5.9 (13.2)	0.0 (0.0)	0.0 (0.0)	1.7 (3.7)	0.0 (0.0)	0.0 (0.0)
Southern pine	+	43.7 (50.6)	3.5 (7.9)	74.1 (165.8)	0.0 (0.0)	0.0 (0.0)	0.0 (0.0)
Indeno[1,2,3-cd]pyrene concentration (ppb)[a]							
Species	Creosote	Soil sampling depth (15 cm away)			Soil sampling depth (30 cm away)		
		0–15 cm	15–30 cm	30–45 cm	0–15 cm	15–30 cm	30–45 cm
Douglas-fir	−	0.0 (0.0)	0.0 (0.0)	0.0 (0.0)	0.0 (0.0)	0.0 (0.0)	0.0 (0.0)
Douglas-fir	+	0.0 (0.0)	0.0 (0.0)	0.0 (0.0)	0.0 (0.0)	0.0 (0.0)	0.0 (0.0)
Southern pine	+	14.2 (31.7)	0.0 (0.0)	0.0 (0.0)	0.0 (0.0)	0.0 (0.0)	0.0 (0.0)
Benzo[g,h,i]perylene concentration (ppb)[a]							
Species	Creosote	Soil sampling depth (15 cm away)			Soil sampling depth (30 cm away)		
		0–15 cm	15–30 cm	30–45 cm	0–15 cm	15–30 cm	30–45 cm
Douglas-fir	−	0.0 (0.0)	0.0 (0.0)	0.0 (0.0)	0.0 (0.0)	0.0 (0.0)	0.0 (0.0)
Douglas-fir	+	0.0 (0.0)	0.0 (0.0)	0.0 (0.0)	0.0 (0.0)	0.0 (0.0)	0.0 (0.0)
Southern pine	+	0.0 (0.0)	0.0 (0.0)	0.0 (0.0)	0.0 (0.0)	0.0 (0.0)	0.0 (0.0)
Dibenz[a,h]anthracene concentration (ppb)[a]							
Species	Creosote	Soil sampling depth (15 cm away)			Soil sampling depth (30 cm away)		
		0–15 cm	15–30 cm	30–45 cm	0–15 cm	15–30 cm	30–45 cm
Douglas-fir	−	0.0 (0.0)	0.0 (0.0)	0.0 (0.0)	0.0 (0.0)	0.0 (0.0)	0.0 (0.0)
Douglas-fir	+	0.0 (0.0)	0.0 (0.0)	0.0 (0.0)	0.0 (0.0)	0.0 (0.0)	0.0 (0.0)
Southern pine	+	0.0 (0.0)	0.0 (0.0)	0.0 (0.0)	0.0 (0.0)	0.0 (0.0)	0.0 (0.0)

[a]Values are means of three replicate samples with one standard deviation in parentheses.

Table S5. Concentrations of 16 polycyclic aromatic hydrocarbons measured in this study found in soils around creosote-treated Douglas-fir and southern pine posts 38 mo after post installation. Soil was collected 15 cm from the post surface and at three depths in the soil column: 0–15 cm (upper), 15–30 cm (middle), and 30–46 cm (lower). Standard deviations for five replicate soil samples around treated posts and two replicate extracts around untreated posts are also shown.

Naphthalene concentration (ppb)[a]							
Species	Creosote	Soil sampling depth (15 cm away)			Soil sampling depth (30 cm away)		
		0–15 cm	15–30 cm	30–45 cm	0–15 cm	15–30 cm	30–45 cm
Douglas-fir	−	27.7 (39.1)	56.2 (61.5)	32.9 (10.8)	77.7 (7.6)	946.1 (1338.0)	60.4 (29.7)
Douglas-fir	+	60.8 (57.3)	124.9 (103.6)	95.7 (47.4)	112.5 (85.8)	89.8 (74.8)	0.0 (0.0)
Southern pine	+	105.3 (57.9)	48.1 (33.4)	107.3 (140.4)	116.6 (69.4)	78.0 (32.3)	94.1 (64.1)
Acenaphthylene concentration (ppb)[a]							
Species	Creosote	Soil sampling depth (15 cm away)			Soil sampling depth (30 cm away)		
		0–15 cm	15–30 cm	30–45 cm	0–15 cm	15–30 cm	30–45 cm
Douglas-fir	−	0.1 (0.2)	0.1 (0.1)	0.0 (0.0)	1.0 (1.4)	32.5 (45.9)	1.4 (1.4)
Douglas-fir	+	59.3 (92.5)	0.0 (0.0)	0.2 (0.4)	2.4 (2.8)	1.9 (4.0)	0.0 (0.0)
Southern pine	+	47.3 (78.4)	5.2 (8.2)	12.4 (16.9)	25.9 (38.9)	40.9 (87.0)	4.8 (6.9)
Acenaphthene concentration (ppb)[a]							
Species	Creosote	Soil sampling depth (15 cm away)			Soil sampling depth (30 cm away)		
		0–15 cm	15–30 cm	30–45 cm	0–15 cm	15–30 cm	30–45 cm
Douglas-fir	−	57.7 (81.6)	110.1 (133.3)	25.8 (0.2)	84.9 (18.3)	2297.2 (3248.7)	86.5 (65.7)
Douglas-fir	+	26.3 (21.2)	42.8 (45.4)	502.6 (878.8)	56.2 (59.8)	25.5 (27.3)	0.0 (0.0)
Southern pine	+	75.4 (39.7)	55.1 (59.2)	244.3 (273.4)	67.9 (56.8)	204.3 (293.5)	199.8 (290.4)
Fluorene concentration (ppb)[a]							
Species	Creosote	Soil sampling depth (15 cm away)			Soil sampling depth (30 cm away)		
		0–15 cm	15–30 cm	30–45 cm	0–15 cm	15–30 cm	30–45 cm
Douglas-fir	−	45.1 (63.7)	50.0 (55.7)	9.9 (3.3)	56.2 (32.3)	848.0 (1199.2)	42.6 (41.6)
Douglas-fir	+	8.0 (6.7)	9.7 (14.0)	451.5 (1014.7)	13.3 (9.1)	8.5 (10.8)	0.0 (0.0)
Southern pine	+	53.5 (36.5)	31.9 (41.7)	228.9 (268.4)	37.5 (27.4)	136.7 (202.8)	144.6 (240.7)
Phenanthrene concentration (ppb)[a]							
Species	Creosote	Soil sampling depth (15 cm away)			Soil sampling depth (30 cm away)		
		0–15 cm	15–30 cm	30–45 cm	0–15 cm	15–30 cm	30–45 cm
Douglas-fir	−	294.8 (416.9)	79.7 (78.8)	33.1 (13.0)	158.4 (164.0)	1859.6 (2629.9)	45.8 (37.0)
Douglas-fir	+	389.6 (454.8)	310.8 (523.7)	297.3 (537.8)	236.8 (152.0)	30.9 (32.7)	0.0 (0.0)
Southern pine	+	522.7 (299.4)	220.4 (250.7)	747.3 (709.0)	458.0 (333.2)	301.6 (259.7)	692.3 (1022.4)
Anthracene concentration (ppb)[a]							
Species	Creosote	Soil sampling depth (15 cm away)			Soil sampling depth (30 cm away)		
		0–15 cm	15–30 cm	30–45 cm	0–15 cm	15–30 cm	30–45 cm
Douglas-fir	−	303.3 (428.9)	39.4 (48.7)	26.0 (15.8)	14.2 (6.8)	258.5 (365.6)	15.6 (21.0)
Douglas-fir	+	404.8 (512.3)	299.1 (595.0)	273.2 (648.1)	157.5 (237.7)	1.9 (3.2)	0.0 (0.0)
Southern pine	+	526.5 (407.1)	204.5 (291.4)	666.3 (593.4)	289.4 (315.7)	210.0 (281.9)	421.8 (910.0)
Fluoranthene concentration (ppb)[a]							
Species	Creosote	Soil sampling depth (15 cm away)			Soil sampling depth (30 cm away)		
		0–15 cm	15–30 cm	30–45 cm	0–15 cm	15–30 cm	30–45 cm
Douglas-fir	−	74.5 (105.4)	79.0 (95.5)	16.0 (3.3)	258.2 (334.2)	3202.6 (4529.2)	31.8 (18.1)
Douglas-fir	+	1206.6 (1404.1)	820.2 (1410.0)	3086.3 (7075.0)	627.5 (438.0)	59.1 (68.5)	0.0 (0.0)
Southern pine	+	1734.3 (1714.7)	545.6 (775.6)	5300.8 (9786.2)	1194.2 (975.2)	250.4 (303.3)	791.2 (943.8)

[a]Values are means of three replicate samples with one standard deviation in parentheses.

Table S5 (*continued*). Concentrations of 16 polycyclic aromatic hydrocarbons measured in this study found in soils around creosote-treated Douglas-fir and southern pine posts 38 mo after post installation. Soil was collected 15 cm from the post surface and at three depths in the soil column: 0–15 cm (upper), 15–30 cm (middle), and 30–46 cm (lower).

Pyrene concentration (ppb)[a]							
Species	Creosote	Soil sampling depth (15 cm away)			Soil sampling depth (30 cm away)		
		0–15 cm	15–30 cm	30–45 cm	0–15 cm	15–30 cm	30–45 cm
Douglas-fir	−	28.7 (40.6)	53.0 (63.2)	8.3 (5.2)	167.6 (212.6)	1937.6 (2740.2)	22.0 (12.2)
Douglas-fir	+	741.3 (858.8)	506.3 (854.7)	2083.2 (4770.5)	379.8 (263.5)	35.3 (40.6)	0.0 (0.0)
Southern pine	+	1190.3 (1096.5)	356.2 (506.5)	3631.3 (6747.4)	818.1 (657.0)	159.7 (200.2)	495.9 (604.2)
Benz[a]anthracene concentration (ppb)[a]							
Species	Creosote	Soil sampling depth (15 cm away)			Soil sampling depth (30 cm away)		
		0–15 cm	15–30 cm	30–45 cm	0–15 cm	15–30 cm	30–45 cm
Douglas-fir	−	0.4 (0.5)	10.8 (12.2)	1.5 (2.1)	351.9 (493.7)	351.9 (497.6)	2.7 (2.1)
Douglas-fir	+	322.6 (320.3)	216.6 (346.0)	972.9 (1776.7)	114.8 (136.5)	1.3 (2.2)	0.0 (0.0)
Southern pine	+	1498.7 (1560.0)	434.6 (1025.4)	6296.4 (12442.8)	756.2 (930.0)	122.2 (260.1)	659.8 (1200.7)
Chrysene concentration (ppb)[a]							
Species	Creosote	Soil sampling depth (15 cm away)			Soil sampling depth (30 cm away)		
		0–15 cm	15–30 cm	30–45 cm	0–15 cm	15–30 cm	30–45 cm
Douglas-fir	−	83.7 (57.7)	43.4 (55.6)	29.7 (28.4)	352.0 (472.3)	3478.6 (4871.1)	15.2 (5.1)
Douglas-fir	+	393.6 (320.8)	263.5 (361.3)	961.7 (1724.8)	285.1 (110.7)	44.7 (53.6)	0.0 (0.0)
Southern pine	+	1973.5 (1308.3)	571.8 (1071.4)	6178.1 (12101.8)	1480.4 (1281.6)	244.1 (380.7)	780.1 (1103.1)
Benzo[j] and [k] fluoranthene concentration (ppb)[a]							
Species	Creosote	Soil sampling depth (15 cm away)			Soil sampling depth (30 cm away)		
		0–15 cm	15–30 cm	30–45 cm	0–15 cm	15–30 cm	30–45 cm
Douglas-fir	−	33.7 (23.6)	36.8 (40.7)	11.6 (6.0)	176.8 (233.6)	1899.4 (2666.7)	22.9 (21.9)
Douglas-fir	+	358.7 (345.5)	247.9 (365.4)	918.0 (1741.6)	221.6 (119.4)	26.9 (30.0)	0.0 (0.0)
Southern pine	+	1650.3 (2083.7)	281.5 (471.3)	5474.0 (10689.7)	786.1 (670.5)	155.2 (242.8)	449.0 (630.6)
Benzo[a]pyrene concentration (ppb)[a]							
Species	Creosote	Soil sampling depth (15 cm away)			Soil sampling depth (30 cm away)		
		0–15 cm	15–30 cm	30–45 cm	0–15 cm	15–30 cm	30–45 cm
Douglas-fir	−	6.6 (9.3)	8.3 (7.1)	1.5 (2.1)	60.1 (79.4)	519.9 (735.3)	3.2 (0.4)
Douglas-fir	+	26.7 (34.2)	15.2 (23.3)	247.0 (437.4)	12.4 (10.7)	1.4 (2.0)	0.0 (0.0)
Southern pine	+	358.0 (538.8)	17.7 (33.2)	1036.4 (2024.9)	97.6 (58.2)	19.5 (23.4)	125.9 (214.1)
Indeno[1,2,3-cd]pyrene concentration (ppb)[a]							
Species	Creosote	Soil sampling depth (15 cm away)			Soil sampling depth (30 cm away)		
		0–15 cm	15–30 cm	30–45 cm	0–15 cm	15–30 cm	30–45 cm
Douglas-fir	−	0.0 (0.0)	0.6 (0.8)	0.0 (0.0)	22.5 (31.9)	178.0 (251.7)	0.0 (0.0)
Douglas-fir	+	8.6 (11.8)	8.7 (17.2)	88.4 (151.4)	4.8 (6.5)	0.0 (0.0)	0.0 (0.0)
Southern pine	+	181.1 (240.5)	16.3 (39.8)	473.4 (934.6)	84.9 (72.9)	8.3 (14.4)	44.8 (78.7)
Benzo[g,h,i]perylene concentration (ppb)[a]							
Species	Creosote	Soil sampling depth (15 cm away)			Soil sampling depth (30 cm away)		
		0–15 cm	15–30 cm	30–45 cm	0–15 cm	15–30 cm	30–45 cm
Douglas-fir	−	0.0 (0.0)	0.0 (0.0)	0.0 (0.0)	25.4 (35.9)	238.5 (337.3)	0.0 (0.0)
Douglas-fir	+	6.6 (9.1)	5.6 (11.2)	77.1 (131.8)	4.4 (5.5)	0.0 (0.0)	0.0 (0.0)
Southern pine	+	162.8 (227.5)	11.9 (29.2)	401.4 (792.7)	66.8 (57.1)	9.4 (11.3)	41.9 (75.5)
Dibenz[a,h]anthracene concentration (ppb)[a]							
Species	Creosote	Soil sampling depth (15 cm away)			Soil sampling depth (30 cm away)		
		0–15 cm	15–30 cm	30–45 cm	0–15 cm	15–30 cm	30–45 cm
Douglas-fir	−	0.0 (0.0)	0.0 (0.0)	0.0 (0.0)	0.3 (0.5)	0.8 (1.1)	0.0 (0.0)
Douglas-fir	+	0.0 (0.0)	0.0 (0.0)	9.2 (15.3)	0.0 (0.0)	0.0 (0.0)	0.0 (0.0)
Southern pine	+	26.9 (47.1)	0.0 (0.0)	94.6 (188.0)	3.4 (6.4)	0.0 (0.0)	3.0 (6.8)

[a]Values are means of three replicate samples with one standard deviation in parentheses.

Structural and chemical characterization of Douglas-fir and red alder biochar

Samuel Olajide
Department of Wood Science and Engineering, Oregon State University, Corvallis, OR 97331, USA Email: samuel.olajide@oregonstate.edu

Tomiwa Haruna
Department of Wood Science and Engineering, Oregon State University, Corvallis, OR 97331, USA Email: harunatomijeje2000@gmail.com

Alhassan Ibrahim
Department of Wood Science and Engineering, Oregon State University, Corvallis, OR 97331, USA Email: hassanbinrazak157@yahoo.com

Robert J. Macias
Department of Wood Science and Engineering, Oregon State University, Corvallis, OR 97331, USA Email: maciasnr@oregonstate.edu

Gerald Presley†
Department of Wood Science and Engineering, Oregon State University, Corvallis, OR 97331, USA Email: gerald.presley@oregonstate.edu

*Islam Hafez**
Department of Wood Science and Engineering, Oregon State University, Corvallis, OR 97331, USA Email: islam.hafez@oregonstate.edu

(Received 23 July 2026)

Abstract: Biochar properties are often interpreted primarily as a function of pyrolysis temperature, but feedstock compositional differences can also influence the structural evolution of woody biochar. This study provides a complementary characterization of biochar produced from Douglas-fir (*Pseudotsuga menziesii*) softwood and red alder (*Alnus rubra*) hardwood forest residues under comparable pyrolysis conditions. Douglas-fir biochar was produced at 350°C, 500°C, and 700°C, while red alder biochar was produced at 500°C, using fast pyrolysis in a custom-built fluidized bed reactor. The biochar was characterized using proximate and elemental analysis, CO_2 BET surface area, pH, Raman spectroscopy, Fourier transform infrared spectroscopy, and thermogravimetric analysis. Within the Douglas-fir series, increasing pyrolysis temperature decreased biochar yield, volatile matter, and oxygenated functional groups, while increasing gas yield, fixed carbon, alkalinity, surface area, and thermal stability. Under identical pyrolysis conditions at 500°C, red alder biochar retained greater C-H and O-H functionality and higher O/C and H/C ratios than Douglas-fir biochar. These differences were consistent with feedstock compositional differences, particularly the higher hemicellulose content and syringyl-guaiacyl lignin composition of red alder, which may favor retention of hydrogenated and oxygenated structures. In contrast, the higher guaiacyl lignin content of Douglas-fir may have contributed to greater carbon condensation, deoxygenation, and aromatization. Raman analysis showed increasing I_D/I_G ratio with pyrolysis temperature, indicating changes in carbon structure during thermal reorganization. Feedstock differences were evaluated at 500°C, while temperature effects were assessed only for Douglas-fir. The results from this study link feedstock composition with differences in functional-group retention, carbon condensation, and thermal stability.

Keywords: Biochar; Pyrolysis temperature; Biomass feedstock; Characterization; Thermal stability; Functional groups.

Introduction

Biochar is a carbon-rich, porous by-product of biomass pyrolysis under oxygen-limited conditions (Manyà 2012; Kamarudin et al. 2022). It is widely used as a multifunctional material in soil fertilization, metal immobilization, water treatment, and construction applications (Chen et al. 2011; Awad et al. 2012; Bolan et al. 2022). Its utility arises from tunable properties, including high porosity, large surface area, variable surface chemistry, and chemical stability (Liu et al. 2015; Hassan et al. 2020). As a soil amendment, biochar improves productivity by increasing soil organic matter, water retention, microbial activity, and nutrient retention (Glaser et al. 2002; Sopeña et al. 2012; Bian et al. 2013; Sun et al. 2017; Yaashikaa et al.

* Corresponding author
† Society of Wood Science & Technology member

2020). Its sorption properties also enable removal of pollutants, including toxic heavy metals, from water (Ahmad et al. 2014; Shakoor et al. 2020). In construction, biochar has been incorporated into concrete and cement composites to improve thermal insulation, chemical stability, and flammability resistance (Gupta et al. 2018; Restuccia et al. 2020; Legan et al. 2022), and into polymer composites to enhance mechanical strength and thermal resistance (Das et al. 2015; Zhang et al. 2022).

Despite its broad applicability, biochar properties are highly variable and are strongly influenced by biomass feedstock and pyrolysis conditions (Ahmad et al. 2012; Zhao et al. 2013). Feedstock type influences the chemical composition, structural features, and functional potential of the resulting biochar (Gaskin et al. 2008; Yuan et al. 2011). Common feedstocks include animal waste, industrial waste, sewage sludge, wood chips, food waste, agricultural residues, and forest residues (Bedia et al. 2018). Leng et al. (2021) classified biochar feedstocks as wood and woody biomass, herbaceous and agricultural biomass, manure/waste biomass, and algae biomass. Lignocellulosic feedstocks differ in cellulose, hemicellulose, lignin, extractives, and inorganic contents, which influence biochar yield, elemental composition, and carbon stability (Tomczyk et al. 2020; Chaturvedi et al. 2023).

Biochar characteristics are also shaped by reactor design and production conditions, particularly pyrolysis temperature (Sun et al. 2014; Ahmad et al. 2014; Manyà et al. 2018). Higher temperatures generally reduce biochar yield through increased organic matter volatilization and secondary cracking, while promoting CO_2/CH_4 evolution, carbon densification, and formation of more aromatic, carbon-rich structures (Novak et al. 2009; Sun et al. 2012). Elemental composition typically shifts toward higher carbon content and aromaticity, with lower hydrogen and oxygen contents, producing a less polar and more hydrophobic material (Ahmad et al. 2014). The effects of feedstock and pyrolysis temperature are complex and may act independently or interactively (Tripathi et al. 2016; Ippolito et al. 2020; Tomczyk et al. 2020). For example, the temperature that maximizes surface area can vary with feedstock properties (Sharma et al. 2015; Kan et al. 2016).

Although the effects of feedstock type and pyrolysis temperature on biochar properties have been widely studied, direct comparative studies of Douglas-fir and red alder forest-residue biochar produced under comparable pyrolysis conditions appear to be limited. This species-specific comparison is relevant because Douglas-fir and red alder are two important softwood and hardwood resources in the US with different lignocellulosic composition, ash content, extractives, and lignin chemistry. These differences may influence the extent of functional-group retention, deoxygenation, mineral-associated residue formation, aromatization, and carbon condensation during pyrolysis. Therefore, this study provides a complementary characterization of Douglas-fir biochar across different pyrolysis temperatures and of Douglas-fir and red alder biochar produced at 500°C. The 500°C comparison was used to explore potential relationships between feedstock composition of these two species and variation in surface functionality, elemental composition, thermal stability, and Raman spectral features.

Materials and methods

Douglas-fir (*Pseudotsuga menziesii)* softwood and red alder (*Alnus rubra)* hardwood, composed of mixed size branches, bark and bole wood, were used as raw materials for pyrolysis. These raw materials were sourced from multiple locations in Oregon.

Production of biochar

Wood particles were air-dried to 10% dry-basis moisture content (MC). The particles were ground using a 3 hp CF 198 model electric hammer mill (PelletMasters, WI, USA), and sieved through a 0.5 mm W.S Tyler Incorporated standard testing sieve before pyrolysis. Biochar was produced in a custom-built fluidized bed pyrolyzer previously described in detail by Macias et al. (2026). The reactor core consisted of a 304 stainless-steel, Schedule 40 tube approximately 54 in. (1.37 m) in length and 3 in. (7.62 cm) in nominal diameter. The reactor was heated externally by two independently controlled furnace sections equipped with four Watlow electric heating elements (2 × 1.8 kW and 2 × 2.5 kW; 8.6 kW total installed power) and PID temperature controllers. Internal thermocouples positioned along the reactor were used to continuously monitor reactor temperature. No silica sand or other inert bed material was used in these experiments because the recovered biochar was intended for subsequent physicochemical characterization. Fluidization was therefore achieved directly with the biomass and char particles present in the reactor, avoiding contamination or dilution of the recovered biochar with an external mineral bed material. High-purity nitrogen was introduced through the bottom plenum and gas-distribution screen and supplied using an Alicat mass-flow controller at approximately 4 SLPM. The standard volumetric flow rate was referenced to 25°C and approximately 1 atm. Based on the internal cross-sectional area (3-in.) of the reactor, there was a correction of the gas volumetric flow for reactor temperature. The corresponding superficial nitrogen velocities were approximately 0.029, 0.036, and 0.046 m s^{-1} at 350°C,

500C°, and 700°C, respectively. For the 0.5-mm biomass particles, the minimum fluidization velocity was estimated using the Kunii and Levenspiel fluidization correlations and was on the order of 0.01 m s^{-1}, depending on feedstock properties and operating temperature (Kunii and Levenspiel 1997). The selected nitrogen flow therefore maintained the solids above the estimated minimum fluidization condition throughout the experiments.

Before biomass feeding, the desired pyrolysis temperature was entered into the PID controllers and the reactor was heated under continuous nitrogen flow. Once the internal thermocouples reached the prescribed target temperature, the reactor was maintained at that temperature for an additional 2 h to ensure thermal equilibrium and a stable temperature profile throughout the reactor. Biomass feeding was initiated only after this stabilization period. The same procedure was followed for all pyrolysis temperatures investigated.

Approximately 2 kg of each biomass was subsequently fed into the reactor at 40 g/min, corresponding to a feeding period of approximately 50 min, while the reactor was maintained at the prescribed pyrolysis temperature. Following completion of biomass feeding, the reactor was maintained at the target temperature for an additional 30 min to allow further devolatilization of residual material. Douglas-fir biochar produced at 350°C, 500°C, and 700°C was referred to as DF 350, DF 500, and DF 700, respectively, whereas red alder biochar produced at 500°C was referred to as RA 500. Three independent pyrolysis runs were conducted for each condition.

After pyrolysis, the electric heaters were switched off while nitrogen flow was continuously maintained during cooling. The biochar therefore remained under an inert atmosphere until the reactor approached room temperature, minimizing oxidation of the freshly produced char prior to collection and storage.

Biochar and biomass characterization

Proximate analysis, BET surface area analysis, and pH measurement

Moisture content, volatile matter (VM), and ash content (AC) were determined using Equations (1-3) and a modified ASTM D1762-84 Standard Test Method for Chemical Analysis of Wood Charcoal (ASTM International 2021) adapted for biochar analysis in a muffle furnace (Aldayyat et al. 2021; Chisté et al. 2024). Crucibles were pre-fired at 750°C for 6 h and cooled to 105°C to volatilize residual organic substances before analysis. MC was determined by oven-drying samples at 105°C for 48 h. VM was measured by heating oven-dried samples in lidded crucibles in a preheated muffle furnace at 950°C for approximately 7 min, followed by cooling in a desiccator and recording weight loss. AC was determined from the residue remaining after combusting oven-dried samples in open crucibles at 750°C for 6 h.

$$MC\ (\%) = \frac{Wet\ weight - Dry\ weight\ at\ 105\ °C}{Dry\ weight\ at\ 105\ °C}\ x\ 100 \quad [1]$$

$$VM\ (\%) = \frac{Dry\ weight\ at\ 105\ °C - Dry\ weight\ at\ 950\ °C}{Dry\ weight\ at\ 105\ °C}\ x\ 100 \quad [2]$$

$$AC\ (\%) = \frac{Wet\ weight - Dry\ weight\ at\ 750\ °C}{Dry\ weight\ at\ 105\ °C}\ x\ 100 \quad [3]$$

Fixed carbon (FC) and biochar yield (Y) were calculated according to equations (4) and (5), respectively. All values were expressed on a dry weight basis.

$$FC\ (\%) = 100 - (MC + VM + AC) \quad [4]$$

$$Y\ (\%) = \frac{Biochar\ mass}{Dry\ weight\ of\ biomass\ at\ 105\ °C}\ x\ 100 \quad [5]$$

Carbon dioxide adsorption isotherms were measured at 273 K using a Micromeritics TriStar II PLUS Surface Area and Porosity Analyzer (Norcross, GA, USA). Before analysis, samples were degassed for 18 h at 453 K under vacuum using a Micromeritics VacPrep 061 Degassing System. CO_2 adsorption isotherms were collected over $p/p_0 = 10^{-5} - 0.03$ using 75 equilibration points to capture low-pressure adsorption associated with microporosity. Apparent CO_2 BET surface area was calculated from the adsorption isotherms (Dubinin and Radushkevich 1947; Dubinin et al. 1947).

Biochar pH was measured following Singh et al. (2017). Approximately 5 g of biochar was dispersed in 50 mL distilled water and shaken for 1 h at room temperature using an ONiLAB orbital shaker (Walnut, CA) at 150 rpm. The suspension was allowed to equilibrate for 30 min before pH measurement with an OHAUS Starter 2200 bench pH meter (Parsippany, NJ).

Biomass characterization

The detailed biomass characterization of the material used in this study has been previously reported by Macias et al. (2026). Cellulose, hemicellulose, lignin, ash, and extractives contents were determined according to the standard compositional analysis procedures (Sluiter et al. 2012). Briefly, extractives were removed prior to analysis, and the remaining structural

biomass was fractionated to quantify cellulose, hemicellulose, and lignin contents. Lignin was determined as the sum of acid-insoluble and acid-soluble fractions, while ash was measured gravimetrically after combustion. All compositional values were expressed on an oven-dry weight basis.

Raman and Fourier transform infrared spectroscopy

Raman spectra were collected using a Shimadzu Airsight Raman Microscope (Columbia, MD) to assess carbon structure. Spectra were acquired with a 532 nm laser and 50× objective over 500-4000 cm^{-1}, averaging 80 scans. All spectra were baseline corrected. Fourier transform infrared spectroscopy (FT-IR) spectra were collected using a Shimadzu IRTracer-100 (Columbia, MD) to identify functional groups. Spectra were acquired in absorbance mode at 4 cm^{-1} resolution from 500 to 4000 cm^{-1}, averaging 45 scans. All FT-IR spectra were baseline corrected and normalized to the maximum absorbance peak to enable comparison among samples.

Elemental analysis

The relative carbon, hydrogen, nitrogen, and oxygen contents of biochar were determined using a LECO CHN828 series analyzer (St. Joseph, MI). Approximately 75 mg of biochar was used per run, consistent with the instrument calibration range of 70–140 mg. Oxygen content was calculated by difference after measuring carbon, hydrogen, and nitrogen.

Thermogravimetric analysis

Thermogravimetric analysis (TGA) was performed using a TA Instrument thermogravimetry analyzer (New Castle, DE), TGA 550, to assess the biochar's thermal stability and degradation profile. Approximately 7 to 10 mg of biochar was heated from room temperature to 800°C at a 10°C/min heating rate, under a nitrogen atmosphere.

Scanning electron microscopy

The morphology of the samples was observed through scanning electron microscopy (SEM) (FEI Quanta 600 FEG) with a high voltage of 3.0 kV and a working distance ranging from 9.8 mm to 10 mm. The SEM images were obtained from Douglas-fir and red alder biochar produced in a separate slow pyrolysis experiment and were not collected from the fast-pyrolysis biochar used for the other characterization analyses in this study. Samples were sputter-coated with gold before imaging, and images were acquired at magnifications ranging from 250x to 2500x.

Statistical analysis

A two-sample t-test was used to compare two independent groups, and one-way ANOVA was used to compare means among more than two independent groups. Tukey's honest significant difference test was used for post hoc pairwise comparisons. All analyses were performed in R at a 95% confidence level.

Results and discussion

Proximate analysis, BET surface area analysis, and pH measurement

The three pyrolysis product yields are shown in Figure 1. Biochar, bio-oil, and gas yields varied with pyrolysis temperature and feedstock. Biochar yield decreased with increasing temperature (Figure 1b), consistent with trends reported for apa wood, iroko wood, and palm kernel shell by Titiladunayo et al. (2012). DF 350 produced the highest biochar yield (34%), whereas DF 500 and DF 700 each produced approximately 18%. This reduction is consistent with increased thermal cracking and decomposition of lignocellulosic components at higher temperatures (Cárdenas-Aguiar et al. 2017). RA 500 produced a slightly higher biochar yield (21%) than DF 500 (18%), showing a relatively small difference in biochar yield between the two feedstocks.

Similar to biochar yield, DF 500 and RA 500 showed similar bio-oil yield at 500°C, producing 56% and 58%, respectively. Tang et al. (2020) similarly reported a 60% bio-oil yield from a machine-learning analysis of 264 bio-oil yield datasets, influenced by feedstock composition. In contrast, pyrolysis temperature strongly affected DF bio-oil yield. DF 500 produced the highest bio-oil yield (56%), compared with 45% for DF 350 which is consistent with lower degree of devolatilization at the lower temperature. Bio-oil yield declined further to 38% for DF 700, indicating additional devolatilization and greater gas formation. Accordingly, DF 700 had the highest gas yield (44%), whereas DF 350 and DF 500 produced 22% and 25%, respectively, consistent with trends reported by Chhiti et al. (2012) and He et al. (2009). RA 500 produced 21% gas, compared with 25% for DF 500. suggesting that feedstock composition may reduce gas formation. Proximate analysis was therefore conducted to further evaluate the effects of feedstock and pyrolysis temperature.

Proximate analysis provides the compositional breakdown of biochar into MC, VM, AC, and FC. Table 1 presents the proximate composition of the four biochar samples. Two-sample t-tests showed significant differences in VM ($p = 0.003$) and FC ($p = 0.0074$) between DF 500 and RA 500. One-way ANOVA showed no significant difference in MC among the DF biochar ($p = 0.3328$), but significant differences in VM ($p = 0.0016$), AC ($p = 0.0002$), and FC ($p = 0.0041$) among DF 350, DF 500, and DF 700.

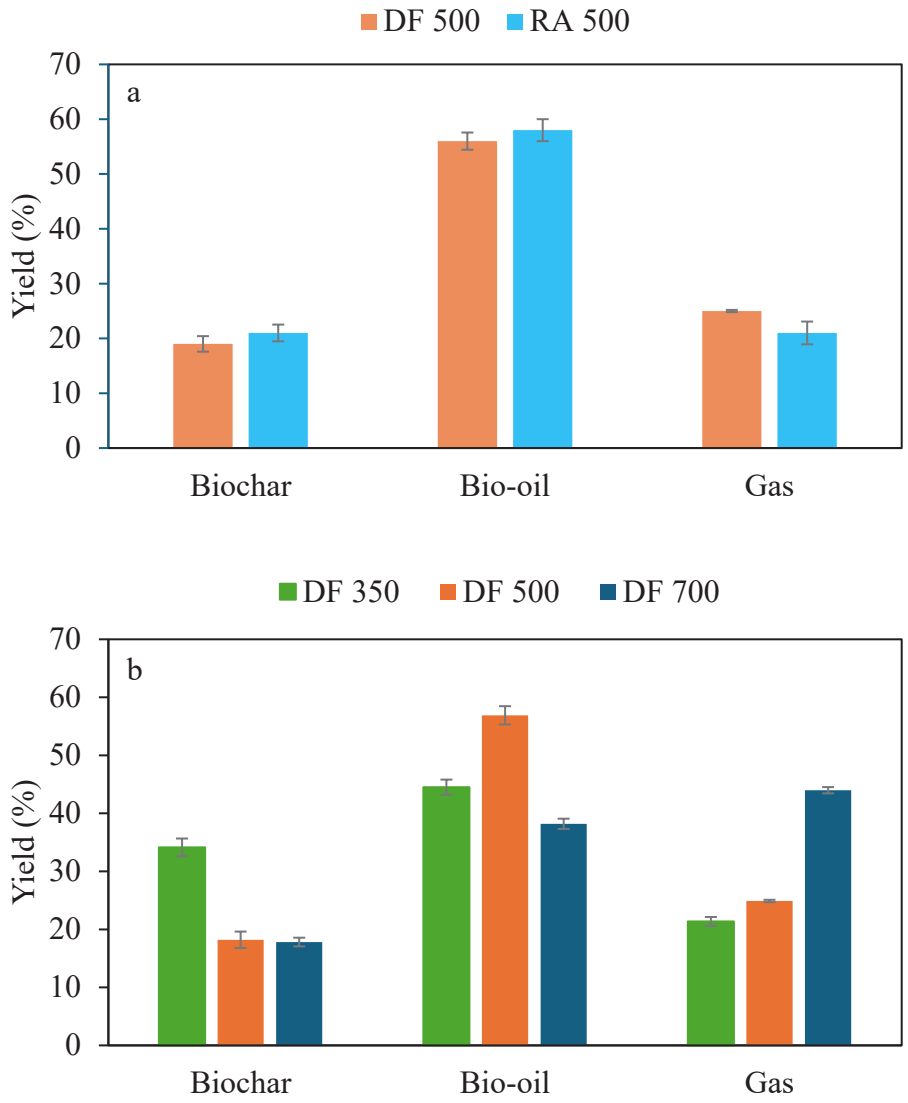


Figure 1. Mean and one standard deviation of (a) biomass feedstock effects on pyrolysis product yields on DF 500 and RA 500; and (b) temperature effects on pyrolysis product yields on DF 350, DF 500, and DF 700.

Table 1. Biochar properties as influenced by biomass feedstock and pyrolysis temperatures.

Sample	Proximate analysis (%) *			
	MC	VM	AC	FC
DF 350	3.06 ± 1.05 ^{a}	37.35 ± 7.85 ^{a}	2.03 ± 0.02 ^{a}	57.56 ± 8.84 ^{a}
DF 500	3.77 ± 0.61 ^{a}	14.04 ± 1.51 ^{b}	10.95 ± 2.07 ^{b}	71.24 ± 2.54 ^{bc}
DF 700	3.07 ± 1.05 ^{a}	11.54 ± 4.12 ^{b}	2.38 ± 0.61 ^{a}	83.01 ± 2.78 ^{c}
RA 500	2.37 ± 0.60	22.03 ± 1.54	11.86 ± 0.56	63.73 ± 0.52

* mean ± one standard deviation of three replicates. One-way ANOVA followed by Tukey's post hoc test was performed separately for each property using DF 350, DF 500, and DF 700. Within each column, means sharing at least one letter are not significantly different ($\alpha = 0.05$); letters are assigned independently for each column. Separate t-test comparisons between DF 500 and RA 500 are reported in the Results and discussion.

All biochar samples had low MC values (2.37%–3.77%), typical of biochar (Das et al. 2015). The lower MC of RA 500 (2.37%) compared with DF 500 (3.77%) may reflect feedstock-dependent pore structure differences. CO_2 BET analysis supported this interpretation where DF 500 had a higher equivalent surface area (337.53 $m^2\ g^{-1}$) than RA 500 (249.04 $m^2\ g^{-1}$), which may contribute to a greater moisture retention.

VM decreased significantly with increasing pyrolysis temperature in DF biochar, from 37.35% in DF 350 to 11.54% in DF 700. This trend is consistent with reports that higher temperatures promote devolatilization and removal of thermally unstable compounds (Ahmad et al. 2014; Suliman et al. 2016; Tomczyk et al. 2020). The sharp decrease from DF

350 to DF 500 (14.04%) indicates a transition from low-temperature biochar to a more condensed carbon structure. VM was also significantly higher in RA 500 (22.03%) than in DF 500 (14.04%), reflecting feedstock differences in composition and thermal degradation behavior; RA may contain more volatilization-prone components (Zhao et al. 2013).

AC varied among samples. DF 500 (10.95%) and RA 500 (11.86%) had the highest ash contents, with no significant difference between them by two-sample t-test ($p = 0.5017$). The higher AC in DF 500 than in DF 350 (2.03%) and DF 700 (2.38%) may indicate incomplete combustion or retention of thermally stable mineral matter.

Ash content decreased at 700°C, likely due to mineral volatilization (Mohan et al. 2014). In contrast, FC increased with pyrolysis temperature, consistent with previous studies (Demirbas 2007; Keiluweit et al. 2010). DF 700 had the highest FC (83.01%), indicating a highly carbonized and stable biochar, whereas DF 350 had the lowest FC (57.56%). Additionally, DF 500 and RA 500 showed substantial carbon retention, with FC values of 71.24% and 63.73%, respectively; however, RA 500 had a significantly lower mean FC than DF 500, again reflecting feedstock compositional differences. The inverse relationship between VM and FC confirms progressive carbon enrichment as volatiles are released during pyrolysis.

Biochar pH ranged from moderately alkaline at lower pyrolysis temperature to strongly alkaline at higher temperatures. DF 350 had an average pH of 8.04, reflecting partial retention of carboxylic acids, phenolic groups, and high residual VM, as indicated by proximate analysis (Domingues et al. 2017; Chisté et al. 2024). With the progressive loss of acidic functional groups and VM, pH increased significantly to 10.34 in DF 500 and remained slightly lower in DF 700 (10.11). RA 500 showed a similar pH to DF 500, averaging 10.20. These results indicate that pyrolysis temperature strongly influences surface chemistry by shifting the balance between acidic and basic functional groups, making it a key factor controlling biochar alkalinity. Higher-temperature biochar generally exhibited stronger alkaline reactions, consistent with previous studies (Silber et al. 2010; Yuan et al. 2011; Manyà 2012; Xu et al. 2012; Keshvardoostchokami et al. 2023).

Raman and FT-IR spectroscopy

Raman spectroscopy characterizes the structural evolution of carbon-based materials. Biochar and other carbonaceous materials exhibit several diagnostic Raman bands. The D band (~1350 cm^{-1}) is commonly associated with disordered carbon structures (Tagliaferro et al. 2020). The G band, typically near 1580 cm^{-1}, is associated with aromatic carbon structures (Datsyuk et al. 2008). The D/G intensity ratio (I_D/I_G) is commonly used to evaluate changes in biochar carbon structure. However, its relationship with structural ordering is not necessarily monotonic in disordered carbon materials. The 2D band, located near 2850 cm^{-1}, is a second-order overtone of the D band and can provide additional information on changes in carbon structures (Childres et al. 2013; De Sousa et al. 2020).

Figure 2a shows the Raman spectra of RA 500 and DF 500 highlighting the D, G, and 2D bands. RA 500 and DF 500 exhibited similar overall Raman features, although differences in peak intensity were observed under the measurement conditions. Figure 2b shows the Raman spectra of DF biochar produced at 350°C, 500°C, and 700°C; DF 700 showed lower Raman intensity than DF 350 and DF 500. These peak features indicate the presence of aromatic clusters in all samples (Fuertes et al. 2010). The I_D/I_G ratios are presented in Table 2. RA 500 and DF 500 had comparable I_D/I_G ratios of 0.70 and 0.68, respectively,

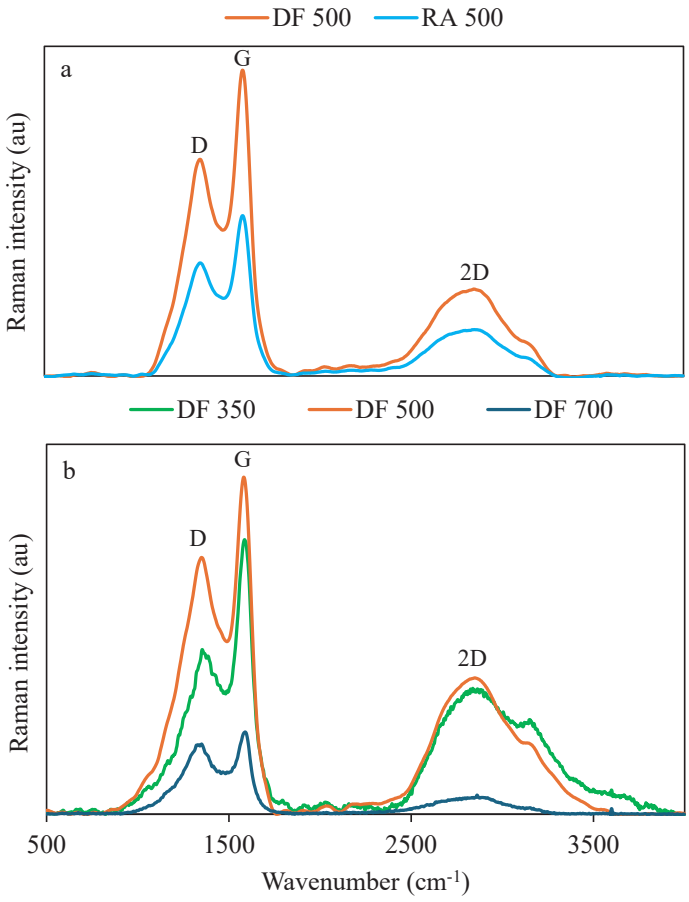


Figure 2. Raman spectra comparing the D, G, and 2D bands on (a) the effects of biomass feedstock on DF 500 and RA 500; and (b) temperature effects on DF 350, DF 500, and DF 700.

Table 2. I_D/I_G ratio results of biochar samples.

Sample	Pyrolysis temperature (°C)	I_D/I_G ratio *
RA 500	500	0.70 ± 0.04
DF 350	350	0.66 ± 0.05
DF 500	500	0.68 ± 0.04
DF 700	700	0.80 ± 0.03

* mean ± one standard deviation of three replicates.

showing similar Raman D/G characteristics at 500°C. This suggests that feedstock-related differences between RA 500 and DF 500 were not strongly expressed in the Raman I_D/I_G ratios. The I_D/I_G ratios of DF 350, DF 500, and DF 700 were 0.66, 0.68, and 0.80, respectively. Within the temperature range examined, the increase in the I_D/I_G ratio indicates changes in the relative contributions of the D and G bands as the carbon structure underwent thermal reorganization. A similar increase at higher pyrolysis temperatures was reported by Chatterjee et al. (2020) for biochar produced from miscanthus (0.65–0.88), switchgrass (0.70–0.88), corn stover (0.58–0.83), and sugarcane bagasse (0.59–1.01) at 500°C–800°C.

The observed trend may partly reflect structural changes associated with volatile and gas evolution during pyrolysis. This process can contribute to structural rearrangement within the carbon matrix. This same trend was also reported in a study carried out by Barszcz et al. (2024). Their study reported that biochar structure became disordered as the pyrolysis temperature increased, despite exhibiting better thermal properties. The increase in I_D/I_G observed between 350°C and 700°C should therefore be interpreted as changes in carbon structure during thermal reorganization rather than evidence for or against extensive graphitization. The temperatures examined in this study are relatively low for extensive graphitic ordering of biomass-derived carbon.

In addition to Raman spectroscopy, FT-IR was used to evaluate biochar surface functional groups. Figure 3 shows the FT-IR spectra, with Figure 3a comparing DF 500 and RA 500. The main spectral difference occurred near ~1400 cm^{-1}, which corresponds to C-H deformation in cellulose and hemicellulose (Woźniak et al. 2022) and was more pronounced in RA 500. This suggests that RA retained more aliphatic C-H bonds than DF after pyrolysis at 500°C. This region may also overlap with

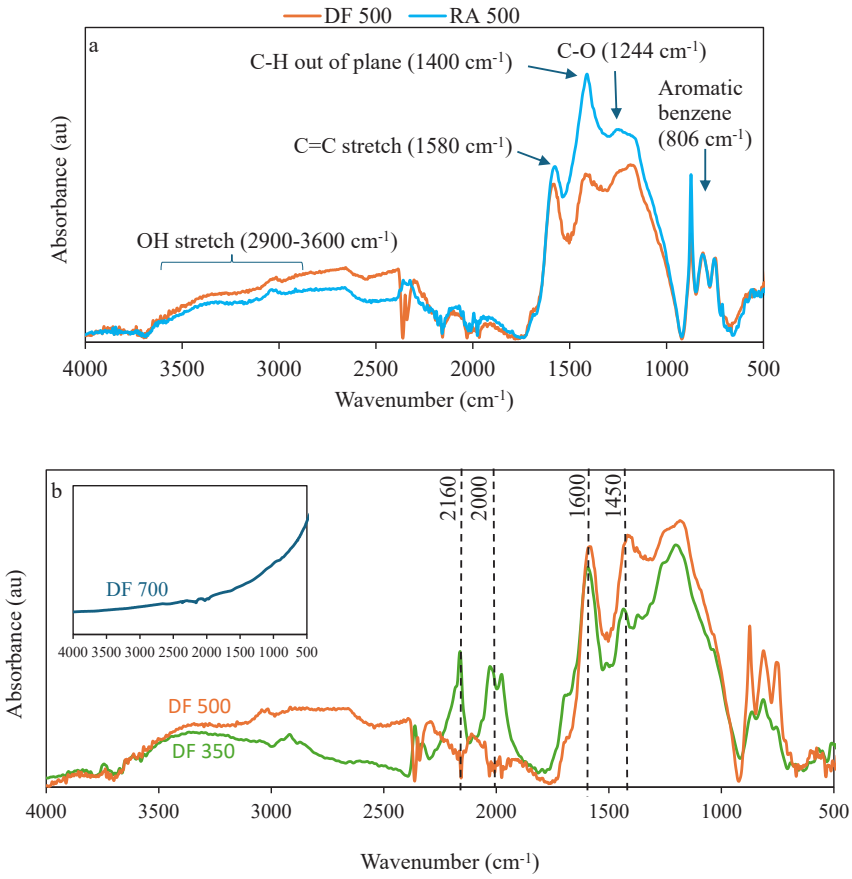


Figure 3. FT-IR spectra comparing the functional group peaks on (a) the effects of biomass feedstock on DF 500 and RA 500; and (b) the temperature effects on DF 350, DF 500, and DF 700.

aliphatic C-H from lignin retained after pyrolysis. The stronger RA 500 band may reflect the hardwood lignin composition of RA, which contains syringyl lignin in addition to guaiacyl lignin. Syringyl lignin is less cross-linked than guaiacyl lignin, which is dominant in softwoods such as DF (Stewart 2008). These differences in lignin structure may influence carbon condensation and functional-group retention during pyrolysis and may therefore contribute to the contrasting FT-IR features of RA 500 and DF 500. The role of feedstock composition in these differences is discussed further in the Effect of chemical composition section. Jackson et al. (2013) similarly reported that pine softwood biochar was more oxidation-resistant at higher temperatures than hardwood oak biochar because of its higher lignin content. DF 500 and RA 500 also showed similar peaks between 1000 and 1250 cm^{-1}, indicating C-H in-plane bending (Li et al. 2023), with the peak near 1100 cm^{-1} attributed to aromatic ester C-O bonds (Vaughn et al. 2013). Considering the MC results in Table 1 and the FT-IR findings, the lower MC of RA 500 is likely more strongly related to pore structure than surface chemistry.

Narrow bands with strong signals were observed near 1600 cm^{-1}, corresponding to aromatic C=C stretching. Weaker bands at 750–900 cm^{-1} are attributed to aromatic structures. Broad absorption at 3200–3400 cm^{-1}, attributed to O-H stretching, indicated hydroxyl groups from residual cellulose, hemicellulose, or absorbed water (Leng et al. 2021). This band was slightly stronger in DF than RA, although the difference was less pronounced than for the C-H band discussed above. Weak peaks at 2800–3000 cm^{-1} corresponded to aliphatic C-H stretching (Lu et al. 2005), while peaks near 2000–2200 cm^{-1} were likely due to aromatic combination bands or overtones, or C≡C functionalities (Kumar 2006).

Among the three pyrolysis temperatures shown in Figure 3b, DF 700 showed no significant peaks, suggesting minimal detectable surface functional groups and less polar surface chemistry. In contrast, DF 350 and DF 500 displayed distinct peaks, with DF 350 showing stronger absorbance. The more pronounced O-H stretching in DF 350 suggests greater retention of hydroxyl-containing structures from residual cellulose, hemicellulose, or adsorbed water. Stronger C-H in-plane bending and C-O bands further indicate higher oxygen-containing functional group abundance, consistent with increased deoxygenation at higher pyrolysis temperatures. For DF 700, dehydration, deoxygenation, and aromatization likely contributed to the substantial reduction in detectable functional groups signals (Liu et al. 2018). Elemental analysis was therefore conducted to help interpret the FT-IR results.

Elemental analysis

Elemental analysis (EA) provides information on the chemical composition of biomass and biochar, including changes in carbon, hydrogen, and oxygen contents with pyrolysis temperature and treatment. These results complement the spectroscopy analyses by indicating the degree of carbonization and changes in elemental composition as a function of pyrolysis conditions. Table 3 presents the elemental composition of DF biomass; DF biochar produced at 350°C, 500°C, and 700°C; RA biomass; and RA biochar produced at 500°C. Carbon content increased from 48% in raw DF biomass to 75% after pyrolysis at 350°C, then increased further to 81% at 500°C and 87% at 700°C. Similarly, carbon content in RA increased from 48% in raw biomass to 71% after pyrolysis at 500°C.

RA 500 had lower relative carbon content than all DF biochar, consistent with the FT-IR results showing greater retention of aliphatic C-H in RA 500 and greater aromatization in DF 500. Oxygen content showed the opposite trend, decreasing with increasing pyrolysis temperature. RA 500 had the highest post-pyrolysis oxygen content (25%), suggesting greater retention of oxygen-containing structures, consistent with the FT-IR evidence for hydroxyl-containing groups. Fuertes et al. (2010) reported a similar finding for corn stover hydrochar, which retained stable functional groups and had an O/C atomic ratio of 0.27. Oxygen-to-carbon (O/C) and hydrogen-to-carbon (H/C) ratios are commonly used to assess biochar chemical stability and polarity. The Van Krevelen diagram in Figure 4

Table 3. Relative elemental composition of DF and RA biomass and biochar.

	Relative composition (%)				Ratio	
Sample	C	H	N	O	O/C	H/C
DF biomass	47.81	6.42	0.34	45.43	0.71	1.60
RA biomass	48.40	6.21	0.31	45.08	0.70	1.53
RA 500	70.84	3.18	1.24	24.74	0.26	0.54
DF 350	74.63	4.24	0.44	20.70	0.21	0.68
DF 500	80.65	2.96	0.76	15.63	0.15	0.44
DF 700	87.34	1.61	0.60	10.46	0.09	0.22

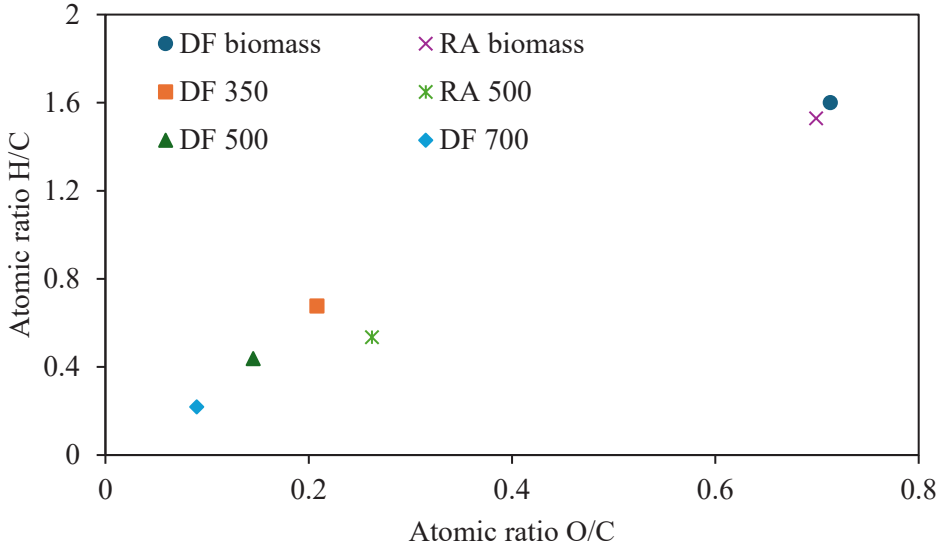


Figure 4. Plot of atomic ratio H/C vs. O/C of the biomass and biochar samples.

plots atomic H/C against O/C ratios for all samples. DF and RA biomass had the highest H/C and O/C ratios, characteristic of raw lignocellulosic biomass (Zhang et al. 2024). With increasing pyrolysis temperature, both ratios decreased, reflecting progressive dehydration and decarboxylation, hydrogen and oxygen loss, carbon enrichment, and increased aromaticity (Wang et al. 2022).

These results indicate that low-temperature biochar retained more oxygenated groups, consistent with FT-IR results, and may therefore offer more reactive sites for subsequent chemical modification. Additionally, this means that the polarity of the biochar was reduced with increasing pyrolysis temperature (Novak et al. 2009; Sun et al. 2012).

Referring to the Raman and FT-IR results, the comparable I_D/I_G ratios of RA 500 and DF 500 indicate that the differences observed in functional group retention and elemental composition were not accompanied by a large difference in the Raman I_D/I_G ratio at 500°C.

Thermogravimetric analysis

TGA provided insight into the thermal decomposition behavior and stability of the raw biomass and biochar samples by monitoring weight loss as a function of temperature. The TGA results provide complementary information on thermal stability that can be compared with the FT-IR and elemental analysis results. As shown in Figure 5a, the thermograms of DF and RA biomass resembled those of typical lignocellulosic materials. The initial stage, from room temperature to ~100°C, corresponded to moisture evaporation, followed by steep degradation associated with thermal decomposition of cellulose and hemicellulose (Yang et al. 2007). Table 4 summarizes the onset temperatures and residue percentages of the samples.

The onset of steep degradation differed between DF and RA biomass, occurring at 263°C for DF and 305°C for RA, followed by gradual lignin degradation over a broader temperature range. The lower onset temperature of DF indicates earlier thermal decomposition of its lignocellulosic components. For the biochar, DF 500 had a higher degradation onset temperature than RA 500 (529°C vs. 502°C), indicating greater resistance to thermal degradation. This is consistent with the lower H/C and O/C ratios and weaker aliphatic and oxygen-containing FT-IR features observed for DF 500. In addition, DF biochar had lower residual mass than RA biochar.

TGA of biochar produced at 350°C, 500°C, and 700°C showed that thermal stability increased with pyrolysis temperature. DF 700 exhibited the lowest weight loss, indicating a carbon-rich

Table 4. TGA onset temperature and residue of the biomass and biochar samples.

Sample	Onset temperature (°C)	Residue (%)
DF biomass	263	81
RA biomass	305	89
RA 500	502	35
DF 350	363	47
DF 500	529	22
DF 700	546	10

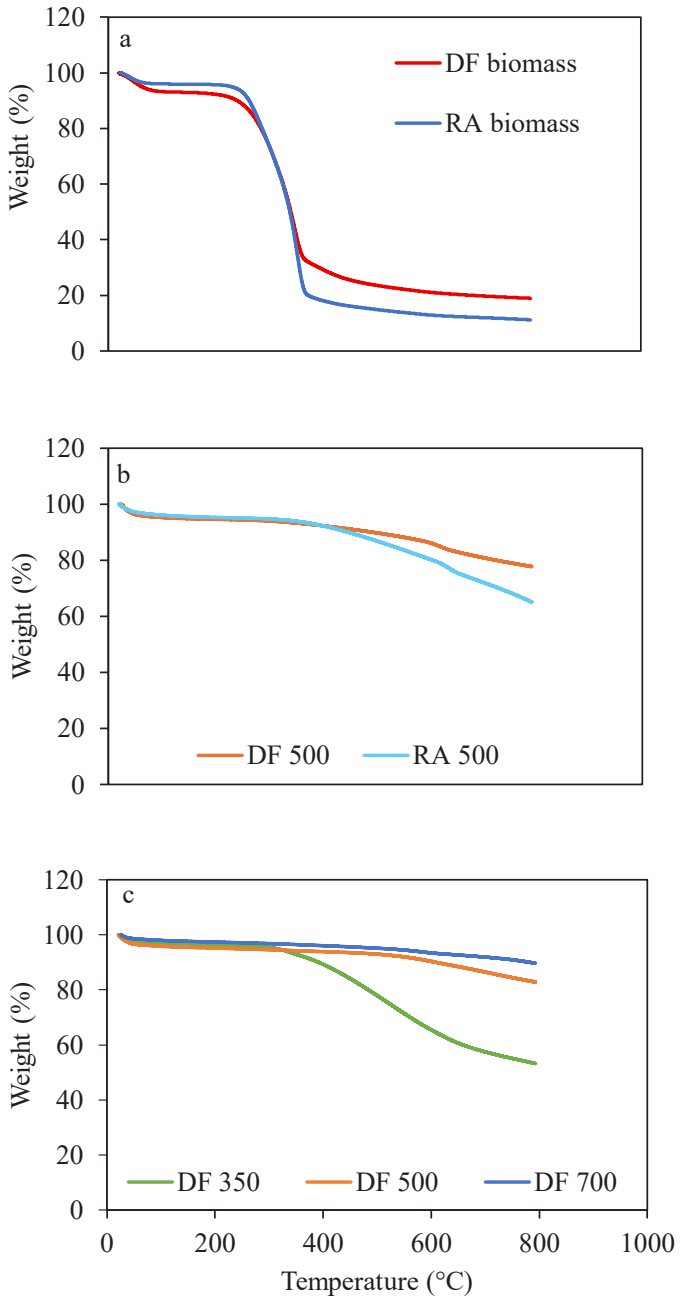


Figure 5. TGA profiles comparing (a) DF and RA biomass; (b) DF and RA biochar produced at 500°C; and (c) DF biochar produced at three different temperatures (350°C, 500°C, and 700°C).

structure, consistent with the low O/C and H/C ratios from elemental analysis (Table 3) and the FT-IR results (Figure 3b). In contrast, DF 350 showed lower thermal stability due to retained functional groups, with degradation onset at 363°C associated with cellulose and hemicellulose decomposition. This result also agrees with the elemental and FT-IR analyses. Residual mass at 800°C decreased substantially with pyrolysis temperature, from 47% for DF 350 to 10% for DF 700. This trend is consistent with previous studies showing that higher pyrolysis temperatures produce biochar with greater carbon content and thermal resilience (Keiluweit et al. 2010; Ahmad et al. 2012).

Effect of chemical composition

RA used in this study contained 34.4 ± 5.3% cellulose, 23.5 ± 4.5% hemicellulose, and 32.3 ± 2.3% lignin, whereas DF contained 35.8 ± 2.4% cellulose, 19.2 ± 7.8% hemicellulose, and 36.8 ± 0.9% lignin (Macias et al. 2026). Cellulose content was similar between the two feedstocks, suggesting that the contrasting behavior at 500°C is more likely associated with differences in hemicellulose content, lignin chemistry, ash, and extractives than with differences in initial cellulose content. The higher hemicellulose content of RA, together with its syringyl-guaiacyl lignin composition, may provide a larger initial pool of oxygen- and hydrogen-rich precursors during pyrolysis. Hemicellulose, the most thermally labile structural biopolymer, degrades at approximately 220°C–315°C and can contribute residual aliphatic C-H fragments to the char matrix at 500°C. Syringyl lignin, which contains two methoxy groups per aromatic ring and is linked mainly by labile β-O-4 ether bonds, can also release aliphatic and oxygenated fragments during cleavage rather than fully condensing into an aromatic structure. Consistent with these compositional differences, RA 500 showed less extensive deoxygenation and aromatization at 500°C, retaining pronounced C-H (~1400 cm^{-1}) and O-H (3200-3600 cm^{-1}) FT-IR bands, as well as elevated O/C (0.26) and H/C (0.54) ratios.

In contrast, the higher guaiacyl lignin content of DF may contribute to carbon condensation. Guaiacyl units contain one methoxy group and are connected by more thermally resistant 5-5 and β-5 carbon-carbon bonds, which resist cleavage and favor aromatic ring fusion as temperature increases. At 500°C, this structure promotes elimination of aliphatic and oxygenated functional groups, producing DF 500 with lower O/C (0.15) and H/C (0.44) ratios and lower TGA residue than RA 500 (22% vs. 35%). These results suggest a more aromatized, oxygen-depleted carbon skeleton in DF 500.

Differences in ash and extractives may have further contributed to the feedstock-dependent behavior. RA had a higher ash content than DF (1.260 ± 0.001% vs. 0.750 ± 0.001%) (Macias et al. 2026), indicating a greater initial mineral fraction that could contribute to the higher residue observed for RA 500 during TGA. Minerals may also influence pyrolysis reactions by catalyzing dehydration, decarboxylation, and char-forming reactions, which could partially affect the retention of oxygenated structures and the final carbon matrix. In contrast,

DF contained substantially higher extractives than RA (8.8 ± 1.3% vs. 3.5 ± 1.0%). These extractives may volatilize or thermally degrade during pyrolysis, contributing to volatile release. Therefore, hemicellulose content and lignin chemistry provide plausible explanations for the contrasting behavior of RA 500 and DF 500, while differences in ash and extractives may act as additional modifiers of thermal degradation, residue formation, and carbon condensation.

It is worth noting that a limitation of the present study is that red alder biochar was produced only at 500°C, whereas Douglas-fir biochar was evaluated across 350°C, 500°C, and 700°C. Consequently, temperature-dependent trends can be assessed only for Douglas-fir, while feedstock-related differences are limited to the direct comparison between Douglas-fir and red alder at 500°C. The current design therefore does not allow feedstock vs temperature interactions to be independently evaluated. Future work should evaluate both feedstocks across a common temperature range to more clearly separate feedstock effects from temperature-dependent responses.

Temperature-dependent structural evolution

The SEM micrographs were obtained from DF and RA biochar produced in a separate slow pyrolysis experiment and were not

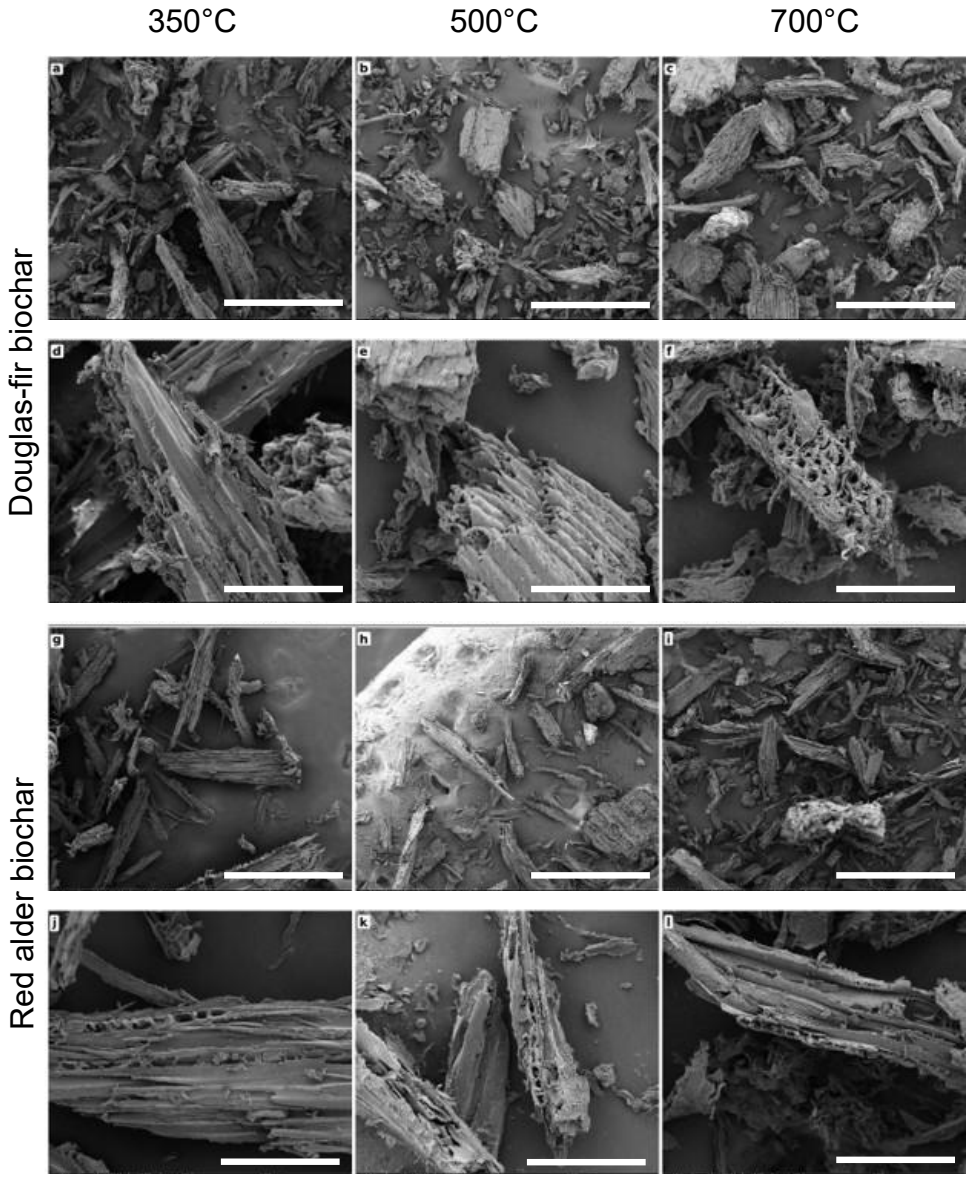


Figure 6. Scanning electron microscopy (SEM) images of biochar samples pyrolyzed at 350°C, 500°C, and 700°C. The top two rows correspond to DF biochar, while the bottom two rows correspond to RA biochar. For each wood species, the first row shows images acquired at 100× magnification (scale bar = 500 μm), and the second row shows higher magnification images at 500× (scale bar = 100 μm).

collected from the fast-pyrolysis biochar characterized earlier. These SEM images are included as complementary qualitative observations of temperature-dependent morphological changes and are not interpreted as direct morphological evidence for the fast pyrolysis samples. Qualitative SEM observations showed changes in DF and RA surface morphology (Figure 6). At 350°C, both DF and RA biochar retained the fibrous, elongated architecture of their wood precursors and displayed open longitudinal channels consistent with preserved cell lumens (Figure 6d,j). At 500°C, both biochar showed greater structural disruption. DF exhibited regular transverse surface corrugation, consistent with cell wall shrinkage and partial collapse (Figure 6e), whereas RA showed heterogeneous conversion, with macroporosity developing in some fiber fragments (Figure 6k). At 700°C, both species exhibited more extensive cellular disruption. DF showed greater collapse of cell walls and elongated elements (Figure 6f), while RA developed elongated interlamellar pores formed by longitudinal cell-wall delamination (Figure 6l).

These observations are consistent with the sequential thermochemical decomposition of hemicellulose, cellulose, and lignin with increasing temperature, where residual lignin provides structural support at 350°C and near-complete biopolymer volatilization at 700°C yields a porous carbon skeleton.

Conclusions

This assessment of Douglas-fir and red alder biochar revealed clear differences in physicochemical properties, thermal behavior, and structural features related to feedstock composition and pyrolysis temperature. A key finding, supported by FT-IR, elemental analysis, and TGA, was that RA 500 retained more hydrogenated and oxygenated structures than DF 500, as shown by stronger C-H and O-H bands and higher O/C and H/C ratios. These differences are consistent with the higher hemicellulose content and syringyl-guaiacyl lignin composition of RA, whereas the higher guaiacyl lignin content of DF may contribute to greater deoxygenation, aromatization, and carbon condensation. Across the Douglas-fir temperature series, biochar yield decreased with increasing temperature, whereas gas yield increased, particularly at 700°C. Proximate analyses showed that higher pyrolysis temperatures reduced volatile matter and increased fixed carbon, while pH shifted from moderately to strongly alkaline values. Raman analysis showed increasing I_D/I_G ratio with pyrolysis temperature, indicating changes in carbon structure during thermal reorganization. Feedstock differences were evaluated only at 500°C, while temperature effects were assessed only for Douglas-fir. Overall, the results show that differences in hemicellulose content, lignin chemistry, ash, and extractives may contribute to the contrasting properties of Douglas-fir and red alder biochar. These relationships provide a basis for further evaluation of woody biomass and pyrolysis conditions for biochar applications.

Data availability: Data will be made available upon request.

Competing interests: The authors declare no competing interests.

References

Ahmad M, Lee SS, Dou X, Mohan D, Sung J-K, Yang JE, Ok YS (2012) Effects of pyrolysis temperature on soybean stover- and peanut shell-derived biochar properties and TCE adsorption in water. Bioresour Technol 118:536–544. https://doi.org/10.1016/j.biortech.2012.05.042

Ahmad M, Rajapaksha AU, Lim JE, Zhang M, Bolan N, Mohan D, Vithanage M, Lee SS, Ok YS (2014) Biochar as a sorbent for contaminant management in soil and water: A review. Chemosphere 99:19–33 https://doi.org/10.1016/j.chemosphere.2013.10.071

Aldayyat EA, Saidan MN, Al-Hamamre Z, Al-Addous M, Alkasrawi M (2021) Pyrolysis of solid waste for bio-oil and char production in refugees' camp: A case study. Energies (Basel) 14 (13):3861. https://doi.org/10.3390/en14133861

ASTM International. (2021). ASTM D1762-84 Standard Test Method for Chemical Analysis of Wood Charcoal. American Society for Testing and Materials, West Conshohocken, PA, USA. https://doi.org/10.1520/D1762-84R21

Awad YM, Blagodatskaya E, Ok YS, Kuzyakov Y (2012) Effects of polyacrylamide, biopolymer, and biochar on decomposition of soil organic matter and plant residues as determined by 14C and enzyme activities. Eur J Soil Biol 48:1–10. https://doi.org/10.1016/j.ejsobi.2011.09.005

Barszcz W, Łożyńska M, Molenda J (2024) Impact of pyrolysis process conditions on the structure of biochar obtained from apple waste. Sci Rep 14:10501. https://doi.org/10.1038/s41598-024-61394-8

Bedia J, Peñas-Garzón M, Gómez-Avilés A, Rodriguez JJ, Belver C (2018) A Review on the Synthesis and Characterization of Biomass-Derived Carbons for Adsorption of Emerging Contaminants from Water. C (Basel) 4(4):63. https://doi.org/10.3390/c4040063

Bian R, Chen D, Liu X, Cui L, Pan G, Xie D, Zheng J, Zhang X, Zheng J, Chang A (2013) Biochar soil amendment as a solution to prevent Cd-tainted rice from China: Results from a cross-site field experiment. Ecol Eng 58:378–383. https://doi.org/10.1016/j.ecoleng.2013.07.031

Bolan N, Hoang SA, Beiyuan J, Gupta S, Hou D, Karakoti A, Joseph S, Jung S, Kim KH, Kirkham MB, Kua H, Kumar M, Kwon E, Ok YS, Perera V, Rinklebe J, Shaheen S, Sarkar B, Sarmah A, Van Zwieten L (2022) Multifunctional applications of biochar beyond carbon storage. International Materials Reviews 67(2):150–200 https://doi.org/10.1080/09506608.2021.1922047

Cárdenas-Aguiar E, Gascó G, Paz-Ferreiro J, Méndez A (2017) The effect of biochar and compost from urban organic waste on plant biomass and properties of an artificially copper polluted soil. Int Biodeterior Biodegradation 124:223–232. https://doi.org/10.1016/j.ibiod.2017.05.014

Chatterjee R, Sajjadi B, Chen WY, Mattern DL, Hammer N, Raman V, Dorris A (2020) Effect of Pyrolysis Temperature on PhysicoChemical Properties and Acoustic-Based Amination of Biochar for Efficient CO2 Adsorption. Front Energy Res 8. https://doi.org/10.3389/fenrg.2020.00085

Chaturvedi S, Singh SV, Dhyani VC, Govindaraju K, Vinu R, Mandal S (2023) Characterization, bioenergy value, and thermal stability of biochars derived from diverse agriculture and forestry lignocellulosic wastes. Biomass Convers Biorefin 13:879–892. https://doi.org/10.1007/s13399-020-01239-2

Chen B, Chen Z, Lv S (2011) A novel magnetic biochar efficiently sorbs organic pollutants and phosphate. Bioresour Technol 102(2):716–723. https://doi.org/10.1016/j.biortech.2010.08.067

Chhiti Y, Salvador S, Commandré JM, Broust F (2012) Thermal decomposition of bio-oil: Focus on the products yields under different pyrolysis conditions. Fuel 102:274–281. https://doi.org/10.1016/j.fuel.2012.06.098

Childres I, Jauregui LA, Park W, Cao H, Chen YP (2013) Raman spectroscopy of graphene and related materials. In: Jang, J.I., Ed., New Developments in Photon and Materials Research, NOVA Science Publishers, Inc., New York, 403–418. https://novapublishers.com/shop/new-developments-in-photon-and-materials-research/

Chisté L, Melo LCA, Jindo K, Silva CA (2024) Biochar-boron composites: synthesis, properties and agronomic effectiveness for eucalyptus seedlings. Chemical and Biological Technologies in Agriculture 11(154). https://doi.org/10.1186/s40538-024-00645-2

Das O, Sarmah AK, Bhattacharyya D (2015) A novel approach in organic waste utilization through biochar addition in wood/polypropylene composites. Waste Management 38:132–140. https://doi.org/10.1016/j.wasman.2015.01.015

Datsyuk V, Kalyva M, Papagelis K,Parthenios J, Tasis D, Siokou A, Kallitsis I, Galiotis C (2008) Chemical oxidation of multiwalled carbon nanotubes. Carbon N Y 46(6):833–840. https://doi.org/10.1016/j.carbon.2008.02.012

De Sousa DV, Guimarães LM, Félix JF, Ker JC, Schaefer CERG, Rodet MJ (2020) Dynamic of the structural alteration of biochar in ancient Anthrosol over a long timescale by Raman spectroscopy. PLoS One 15(3):e0229447. https://doi.org/10.1371/journal.pone.0229447

Demirbas A (2007) Effect of temperature on pyrolysis products from biomass. Energy Sources, Part A: Recovery, Utilization and Environmental Effects 29(4):329–336. https://doi.org/10.1080/009083190965794

Domingues RR, Trugilho PF, Silva CA, Melo ICNAd, Melo LCA, Magriotis ZM, Sánchez-Monedero MA (2017) Properties of biochar derived from wood and high-nutrient biomasses with the aim of agronomic and environmental benefits. PLoS One 12(5):e0176884. https://doi.org/10.1371/journal.pone.0176884

Dubinin MM, Radushkevich LV (1947) Equation of the characteristic curve of activated charcoal. Proceedings of the Academy of Sciences of the USSR: Physical Chemistry Section 55:331-337.

Dubinin MM, Zaverina ED, Radushkevich, L. V. (1947). Sorption and structure of active carbons. I. Adsorption of organic vapors. Zhurnal Fizicheskoi Khimii 21(3), 151–162.

Fuertes AB, Arbestain MC, Sevilla M, Maciá-Agulló JA, Fiol S, López R, Smernik RJ, Aitkenhead WP, Arce F, Macias F (2010) Chemical and structural properties of carbonaceous products obtained by pyrolysis and hydrothermal carbonisation of corn stover. Australian Journal of Soil Research 48(7):618–626. https://doi.org/10.1071/SR10010

Gaskin JW, Steiner C, Harris K, Das KC, Bibens B (2008) Effect of low-temperature pyrolysis conditions on biochar for agricultural use. Trans ASABE 51(6): 2061–2069. https://doi.org/10.13031/2013.25409

Glaser B, Lehmann J, Zech W (2002) Ameliorating physical and chemical properties of highly weathered soils in the tropics with charcoal - A review. Biol. Fertil. Soils 35:219–230. https://doi.org/10.1007/s00374-002-0466-4

Gupta S, Kua HW, Koh HJ (2018) Application of biochar from food and wood waste as green admixture for cement mortar. Science of the Total Environment 619–620:419–435. https://doi.org/10.1016/j.scitotenv.2017.11.044

Hassan M, Liu Y, Naidu R, Parikh SJ, Du J, Qi F, Willett IR (2020) Influences of feedstock sources and pyrolysis temperature on the properties of biochar and functionality as adsorbents: A meta-analysis. Science of the Total Environment 744:140714. https://doi.org/10.1016/j.scitotenv.2020.140714

He M, Hu Z, Xiao B, Li J, Guo X, Luo S, Yang F, Feng Y, Yang G, Liu S (2009) Hydrogen-rich gas from catalytic steam gasification of municipal solid waste (MSW): Influence of catalyst and temperature on yield and product composition. Int J Hydrogen Energy 34(1):195–203. https://doi.org/10.1016/j.ijhydene.2008.09.070

Ippolito JA, Cui L, Kammann C, Wrage-Mönnig N, Estavillo JM, Fuertes-Mendizabal T, Cayuela ML, Sigua G, Novak J, Spokas K, Borchard N (2020) Feedstock choice, pyrolysis temperature and type influence biochar characteristics: a comprehensive meta-data analysis review. Biochar 2:421–438. https://doi.org/10.1007/s42773-020-00067-x

Jackson MA, Eberhardt TL, Boateng AA, Mullen CA, Groom LH (2013) Evaluation of biochars by temperature programmed oxidation/mass spectrometry. Bioresources 8(4):5461–5474. https://doi.org/10.15376/biores.8.4.5461-5474

Kamarudin NS, Dahalan FA, Hasan M, An OS, Parmin NA, Ibrahim N, Hamdzah M, Zain NAM, Muda K, Wikurendra EA (2022) Biochar: A review of its history, characteristics, factors that influence its yield, methods of production, application in wastewater treatment and recent development. Biointerface Res Appl Chem 12(6):7914–7926. https://doi.org/10.33263/BRIAC126.79147926

Kan T, Strezov V, Evans TJ (2016) Lignocellulosic biomass pyrolysis: A review of product properties and effects of pyrolysis parameters. Renewable and Sustainable Energy Reviews 57:1126–1140. https://doi.org/10.1016/j.rser.2015.12.185

Keiluweit M, Nico PS, Johnson M, Kleber M (2010) Dynamic molecular structure of plant biomass-derived black carbon (biochar). Environ Sci Technol 44(4):1247–1253. https://doi.org/10.1021/es9031419

Keshvardoostchokami M, Braghiroli FL, Neculita CM, Koubaa A (2023) Advances in modified wood-based adsorbents for contaminant removal: Valorization methods, modification mechanisms, and environmental applications. Current Forestry Reports 9:444–460. https://doi.org/10.1007/s40725-023-00200-6

Kumar S (2006) Spectroscopy of Organic Compounds. Dept of Chemistry 66: https://www.scribd.com/doc/146831979/Spectroscopy-of-Organic-Compounds

Kunii D, Levenspiel O (1997) Circulating fluidized-bed reactors. Chem Eng Sci 52(15):2471–2482. https://doi.org/10.1016/S0009-2509(97)00066-3

Legan M, Gotvajn AŽ, Zupan K (2022) Potential of biochar use in building materials. J. Environ. Manage. 309:114704. https://doi.org/10.1016/j.jenvman.2022.114704

Leng L, Xiong Q, Yang L, Li H, Zhou Y, Zhang W, Jiang S, Li H, Huang H (2021) An overview on engineering the surface area and porosity of biochar. Science of the Total Environment 763:144204. https://doi.org/10.1016/j.scitotenv.2020.144204

Li S, Galoustian T, Trejo H (2023) Biochar pyrolyzed with concentrated solar radiation for enhanced nitrate adsorption. J Anal Appl Pyrolysis 174:106131. https://doi.org/10.1016/j.jaap.2023.106131

Liu WJ, Jiang H, Yu HQ (2015) Development of Biochar-based functional materials: Toward a sustainable platform carbon material. Chem Rev 115:(22):12251–12285. https://doi.org/10.1021/acs.chemrev.5b00195

Liu Z, Niu W, Chu H, Zhou T, Niu Z (2018) Effect of the carbonization temperature on the properties of biochar produced from the pyrolysis of crop residues. Bioresources 13(2):3429–3446. https://doi.org/10.15376/biores.13.2.3429-3446

Lu R, Gan W, Wu BH, Zhang Z, Guo Y, Wang H-f (2005) C-H stretching vibrations of methyl, methylene and methine groups at the vapor/Alcohol (n = 1-8) interfaces. Journal of Physical Chemistry B 109(29):14118–14129. https://doi.org/10.1021/jp051565q

Macias, R. J., Ibrahim, A., Presley, G., Hafez, I., Simonsen, J., Alam, A. Sessions J, Susaeta A, Sierra-Jimenez V, Garcia-Perez, M. (2026). Transforming biomass forest residues into transport fuels part 1: Fast pyrolysis and catalytic hydrotreatment. Biomass and Bioenergy 215:109579. https://doi.org/10.1016/j.biombioe.2026.109579

Manyà JJ (2012) Pyrolysis for biochar purposes: A review to establish current knowledge gaps and research needs. Environ Sci Technol 46(15):7939–7954. https://doi.org/10.1021/es301029g

Manyà JJ, Azuara M, Manso JA (2018) Biochar production through slow pyrolysis of different biomass materials: Seeking the best operating

conditions. Biomass Bioenergy 117:115–123. https://doi.org/10.1016/j.biombioe.2018.07.019

Mohan D, Sarswat A, Ok YS, Pittman CU (2014) Organic and inorganic contaminants removal from water with biochar, a renewable, low cost and sustainable adsorbent - A critical review. Bioresour Technol 160:191–202. https://doi.org/10.1016/j.biortech.2014.01.120

Novak J, Lima I, Xing B, Gaskin JW, Steiner C, Das KC, Ahmedna M, Rehrah D, Watts DW, Busscher WJ, Schomberg H (2009) Characterization of designer biochar produced at different temperatures and their effects on a loamy sand. Annals of Environmental Science 3. https://openjournals.neu.edu/aes/journal/article/view/v3art5

Restuccia L, Ferro GA, Suarez-Riera D, Sirico A, Bernardi P, Belletti B, Malcevschi A (2020) Mechanical characterization of different biochar-based cement composites. Procedia Structural Integrity 25:226–233. https://doi.org/10.1016/j.prostr.2020.04.027

Shakoor MB, Ali S, Rizwan M, Bibi I, Riaz M, Khalil U, Niazi NK, Rinklebe J (2020) A review of biochar-based sorbents for separation of heavy metals from water. Int. J. Phytoremediation 22(2):111–126. https://doi.org/10.1080/15226514.2019.1647405

Sharma A, Pareek V, Zhang D (2015) Biomass pyrolysis - A review of modelling, process parameters and catalytic studies. Renewable and Sustainable Energy Reviews 50:1081–1096. https://doi.org/10.1016/j.rser.2015.04.193

Silber A, Levkovitch I, Graber ER (2010) PH-dependent mineral release and surface properties of cornstraw biochar: Agronomic implications. Environ Sci Technol 44(24):9318–9323. https://doi.org/10.1021/es101283d

Singh B, Dolk MM, Shen Q, Camps-Arbestain M (2017) Biochar : pH, electrical conductivity and liming potential. In: Singh B, Camps-Arbestain M, Lehmann J (eds), Biochar: A Guide to Analytical Methods, CSIRO Publishing, pp 23–38.

Sluiter A, Hames B, Ruiz R, Scarlata C, Sluiter J, Templeton D, Crocker D (2012) Determination of structural carbohydrates and lignin in biomass: Laboratory analytical procedure (LAP). National Renewable Energy Laboratory, Technical Report NREL/TP-510-42618; revised August 2012. https://docs.nlr.gov/docs/gen/fy13/42618.pdf

Sopeña F, Semple K, Sohi S, Bending G (2012) Assessing the chemical and biological accessibility of the herbicide isoproturon in soil amended with biochar. Chemosphere 88:77–83. https://doi.org/10.1016/j.chemosphere.2012.02.066

Stewart D (2008) Lignin as a base material for materials applications: Chemistry, application and economics. Ind Crops Prod 27(2):202–207. https://doi.org/10.1016/j.indcrop.2007.07.008

Suliman W, Harsh JB, Abu-Lail NI, Fortuna A-M, Dallmeyer I, Garcia-Perez M, (2016) Influence of feedstock source and pyrolysis temperature on biochar bulk and surface properties. Biomass Bioenergy 84:37–48. https://doi.org/10.1016/j.biombioe.2015.11.010

Sun J, He F, Pan Y, Zhang Z (2017) Effects of pyrolysis temperature and residence time on physicochemical properties of different biochar types. Acta Agric Scand B Soil Plant Sci 67(1):12–22. https://doi.org/10.1080/09064710.2016.1214745

Sun K, Gao B, Ro KS, Novak JM, Wang Z, Herbert S, Xing B (2012) Assessment of herbicide sorption by biochars and organic matter associated with soil and sediment. Environmental Pollution 163:167–173. https://doi.org/10.1016/j.envpol.2011.12.015

Sun Y, Gao B, Yao Y, Fang J, Zhang M, Zhou Y, Chen H, Yang L, (2014) Effects of feedstock type, production method, and pyrolysis temperature on biochar and hydrochar properties. Chemical Engineering Journal 240:574–578. https://doi.org/10.1016/j.cej.2013.10.081

Tagliaferro A, Rovere M, Padovano E, Bartoli M, Giorcelli M (2020) Introducing the novel mixed Gaussian-Lorentzian lineshape in the analysis of the Raman signal of biochar. Nanomaterials 10:1–19. https://doi.org/10.3390/nano10091748

Tang Q, Chen Y, Yang H, Liu M, Xiao H, Wu Z, Chen H, Naqvi SR (2020) Prediction of Bio-oil Yield and Hydrogen Contents Based on Machine Learning Method: Effect of Biomass Compositions and Pyrolysis Conditions. Energy and Fuels 34(9):11050–11060. https://doi.org/10.1021/acs.energyfuels.0c01893

Titiladunayo IF, McDonald AG, Fapetu OP (2012) Effect of temperature on biochar product yield from selected lignocellulosic biomass in a pyrolysis process. Waste Biomass Valorization 3:311–318. https://doi.org/10.1007/s12649-012-9118-6

Tomczyk A, Sokołowska Z, Boguta P (2020) Biochar physicochemical properties: pyrolysis temperature and feedstock kind effects. Rev Environ Sci Biotechnol 19:191–215. https://doi.org/10.1007/s11157-020-09523-3

Tripathi M, Sahu JN, Ganesan P (2016) Effect of process parameters on production of biochar from biomass waste through pyrolysis: A review. Renewable and Sustainable Energy Reviews 55:467–481. https://doi.org/10.1016/j.rser.2015.10.122

Vaughn SF, Kenar JA, Thompson AR, Peterson SC (2013) Comparison of biochars derived from wood pellets and pelletized wheat straw as replacements for peat in potting substrates. Ind Crops Prod 51:437–443. https://doi.org/10.1016/j.indcrop.2013.10.010

Wang Y, Gu X, Huang Y, Ding Z, Chen Y, Hu X (2022) Insight into biomass feedstock on formation of biochar-bound environmentally persistent free radicals under different pyrolysis temperatures. RSC Adv 12(30):19318–19326. https://doi.org/10.1039/d2ra03052g

Woźniak M, Gromadzka K, Kwaśniewska-Sip P, Cofta G, Ratajczak I (2022) Chitosan–caffeine formulation as an ecological preservative in wood protection. Wood Sci Technol 56:1851–1867. https://doi.org/10.1007/s00226-022-01426-6

Xu R-k, Zhao A-z, Yuan J-h, Jiang J (2012) pH buffering capacity of acid soils from tropical and subtropical regions of China as influenced by incorporation of crop straw biochars. J Soils Sediments 12:494–502. https://doi.org/10.1007/s11368-012-0483-3

Yaashikaa PR, Kumar PS, Varjani S, Saravanan A (2020) A critical review on the biochar production techniques, characterization, stability and applications for circular bioeconomy. Biotechnology Reports 28:e00570. https://doi.org/10.1016/j.btre.2020.e00570

Yang H, Yan R, Chen H, Lee DH, Zheng C (2007) Characteristics of hemicellulose, cellulose and lignin pyrolysis. Fuel 86:1781–1788. https://doi.org/10.1016/j.fuel.2006.12.013

Yuan JH, Xu RK, Zhang H (2011) The forms of alkalis in the biochar produced from crop residues at different temperatures. Bioresour Technol 102:. https://doi.org/10.1016/j.biortech.2010.11.018

Zhang S, Jia X, Wang X, Chen J, Cheng C, Jia X, Hu H (2024) Using the conditional process analysis model to characterize the evolution of carbon structure in *Taxodium ascendens* biochar with varied pyrolysis temperature and holding time. Plants 13(30):460. https://doi.org/10.3390/plants13030460

Zhang Y, He M, Wang L, Yan J, Ma B, Zhu X, Ok YS, Mechtcherine V, Tsang DCW (2022) Biochar as construction materials for achieving carbon neutrality. Biochar 4(59). https://doi.org/10.1007/s42773-022-00182-x

Zhao L, Cao X, Mašek O, Zimmerman A (2013) Heterogeneity of biochar properties as a function of feedstock sources and production temperatures. J Hazard Mater 256–257:1–9. https://doi.org/10.1016/j.jhazmat.2013.04.015

An investigation of the impact response of European ash and sycamore maple

Mojtaba Hassan Vand *
Department of Wood Science and Wood Technology, Mendel University, Zemědělská 1665, Brno, Czech Republic. Email: mojtaba.vand@mendelu.cz

Jan Tippner †
Department of Wood Science and Wood Technology, Mendel University, Zemědělská 1665, Brno, Czech Republic. Email: jan.tippner@mendelu.cz

(Received 7 May 2026)

Abstract: European ash (*Fraxinus excelsior* L.) and sycamore maple (*Acer pseudoplatanus* L.) have long historical applications in structural components requiring high impact resistance, yet a detailed characterization of their full-field dynamic strain behavior remains limited. This study investigates the impact bending responses of both species using three-point drop-weight impact tests integrated with high-speed recording (10,000 frames per second) and the digital image correlation (DIC) method. The distinct and interactive effects of moisture content (MC) and growth-ring orientation (GO) were evaluated across key mechanical metrics: maximum deflection of the beam up to crack initiation, maximum normal strain, maximum reaction force (F_{max}), total absorbed energy, and impact bending strength (IBS). The IBS of ash and maple were 6.3 and 4.5 J/cm², respectively, while their maximum deflection was 8.5 and 8.6 mm, respectively. Two-way ANOVA revealed highly species-specific sensitivities to environmental and structural factors. For European ash, unlike F_{max}, other results such as maximum deflection, maximum strain, total absorbed energy, and IBS were not significantly altered by MC or GO. Conversely, sycamore maple exhibited highly isotropic behavior regarding GO, but it showed to be dependent on the MC. MC significantly enhanced the maximum deflection and maximum normal strain of maple, while triggering a severe 64% reduction in F_{max}. The force-time charts of the tests showed a distinct structural transition from a rigid, brittle fracture mode at low moisture levels to a highly dampening, ductile deformation mode once exceeding the fiber saturation point (FSP). These findings highlight the strong effect of species type on the impact mechanics, providing a robust experimental dataset essential for developing and validating analytical and finite element models.

Keywords: Ash; Maple; Impact test; Digital image correlation method; Three-point bending; High-speed camera; Moisture content; Growth-ring orientation.

Introduction

European ash, or common ash (*Fraxinus excelsior* L.), is a vital species for the functioning and conservation of forests throughout Europe, typically growing as an admixed tree species and rarely achieving dominance (Pautasso et al. 2013). This species thrives on fertile, well-drained soils with a neutral pH and is scattered across various forest communities (Dobrowolska et al. 2011). It can grow from lowland fields and meadows to medium-height mountains, as long as its water requirements are met, and it can reach heights of up to 40 m and a diameter of 1 m (Tudor et al. 2011). Ash is highly sensitive to fire and freezing temperatures; furthermore, it exhibits one of the highest sensitivities to drought (Thomas 2016).

Ash wood's remarkable strength, flexibility, impact resistance, and springiness make it an exceptional material for sports equipment items like baseball bats, tennis rackets, polo shafts, and hockey sticks (Clauß et al. 2014; Boshier et al. 2005). In fact, ash has a significant place in baseball history, largely due to its superior impact strength for bat production (Fortin-Smith et al. 2016a). Compared to many other common wood species, ash boasts relatively high mechanical properties, including excellent strength and fracture toughness (Niemz et al. 2014). Its impact bending strength (IBS) is one of the highest among common species (Borůvka et al. 2020). The exceptional performance of ash under impact loadings has naturally drawn researchers and designers to explore its use in various impact-related applications. Studies have also utilized techniques such as finite element method modeling to predict and optimize the response of ash and other types of wood to impact (Fortin-Smith et al. 2016b, 2018).

* Corresponding author
† Society of Wood Science & Technology member

The sycamore maple (*Acer pseudoplatanus* L.) is a large hardwood tree characterized by a broad, domed crown and a strong root system which can reach heights of 30–35 m (Pasta et al. 2016). This fast-growing species is common in many European forests, though it rarely forms pure stands, typically growing in mixture with other species (Vacek et al. 2018). Sycamore maple can thrive in full sun or partial shade and shows no sensitivity to soil pH, adapting well to a wide range of soil types (Gilman and Watson 1993). It grows successfully in mixed deciduous forests, showing resilience to diverse ecological conditions, saline or eroded soils, and climate shifts (Iliev et al. 2022). Furthermore, it has no difficulty colonizing coarse scree or colluvium on slopes (Bodziarczyk and Lesiński 2011).

Due to its hardness and ease of processing, maple wood is suitable for a range of applications, including furniture, carpentry, flooring, and molding (Sedlar et al. 2021). Alongside ash, maple is also valued for its high IBS (Campshure et al. 2020). Maple wood can have wavy fibers, which makes it particularly favored for the backs of violins and other stringed musical instruments, a practice that luthiers have employed for centuries (Dinulica et al. 2023). The application of maple wood, according to some researchers, could be further expanded and optimized through progressive improvements in data concerning its mechanical properties (Sonderegger et al. 2013).

Given their widespread use, wood and wooden products are frequently subjected to various types of loading, including impacts (Polocoșer et al. 2017). Wooden structures can constantly experience impacts due to common scenarios of different types of tasks, such as automobile crashes affecting wooden guardrails (Gutkowski et al. 2007), natural hazards damaging wooden buildings (Yamada et al. 2018; Turnbull-Grimes et al. 2010), packaging applications (Liu and Chen 2010), or even simple domestic incidents (Acuña et al. 2020). The viscoelastic nature of wood means its response varies significantly with different loading types, from creep to impact. Consequently, various testing methods have been developed to account for these differences in mechanical behavior under varying loading rates (Polocoșer et al. 2018). By studying and understanding wood's mechanical behavior under impact, we can use it more efficiently, broaden its applications, and reduce the risk of potential damage (Baumann et al. 2021).

One of the most common impact tests for wood is the three-point impact bending test. While relatively simple to set up and execute, its analysis is complex due to the simultaneous occurrence of tension, compression, and shear forces (Sahraoui and Lataillade, 1998). This test determines the IBS, which represents the work required to break a specimen, independent of its dimensions (Borůvka et al. 2020). IBS can be measured by dividing the absorbed energy of the impact by the beam's cross-sectional area at its center (Moreira et al. 2017). By altering various parameters and characteristics of the wood samples, this test can identify factors influencing wood's impact behavior (Hassan Vand and Tippner 2023). Both the structural and mechanical properties of wood, along with environmental conditions, can significantly influence its mechanical response (Glass and Zelinka 2021), including its impact response (Kretschmann 2010). Key environmental factors include moisture content (MC), temperature, and any modification applied to the wood.

Due to the chaotic nature of impact loadings, it is preferable to assess desired parameters using non-contact methods (Bragov et al. 2020). One of the most effective techniques for measuring the deformation and motion of objects during tests is digital image correlation (DIC). This method provides comprehensive information about all points of a specimen under examination (Sutton et al. 2009). Although DIC is relatively new to wood testing (Choi et al. 1991), its adoption has been rapid, making it now a common tool for assessing various types of static wood tests and for validating wood modeling methods (Keunecke et al. 2012). To efficiently measure deformations during dynamic tests, DIC requires integrating high-speed camera equipment, enabling the capture of deformations over extremely brief time intervals between successive images (Olmedo et al. 2015; Polocoșer et al. 2016; Hassan Vand et al. 2024). Prior to the advent of DIC, high-speed cameras were primarily used to determine the hammer's speed before and after impact and, consequently, to measure the energy imparted (Gerhards 1977).

Despite the fact that the ash and maple are commonly used woods with a long history of application in higher impact uses, a clear impact-related study with high-speed equipment was needed to see how internal deformation can lead to failure. Wood as a building material or as a part of the living trees can be affected by impacts, which should be controlled to prevent financial losses and casualties. For controlling the impact response and improving safety, a comprehensive study of the impact response of these species is required. This article comprehensively details the mechanical behavior of European ash and sycamore maple under impact loading, utilizing robust and suitable equipment to determine the effect of MC and growth-ring orientation (GO). This research provides information on these species' mechanical responses to impacts, including deflection, internal normal strain of specimens,

reaction loads, the work required for specimen failure, IBS, and shear strains at the neutral axis. The detailed deflection and strain distribution data presented in this paper can serve as a valuable criterion for validating various modeling methods for these wood species. To assess the influence of wood's MC on its impact behavior, these tests were conducted on specimens at two distinct MC levels.

Materials and methods

Samples with dimensions of 20 × 20 × 300 mm (radial × tangential × longitudinal) were cut from wood planks of European ash and sycamore maple from the South Moravian region in the Czech Republic. After preparation, every specimen was inspected visually for knots and defects, and those that did not meet the criteria were discarded. A total of 76 specimens were retained for testing, with 46 samples of ash wood and 30 samples of maple (see Table 1). The specimens of each species were divided into two groups: the lower moisture content (LMC) and the high moisture content (HMC) groups. The LMC samples were stored in a condition of 20°C and 65% relative humidity until their MC stabilized at approximately 11%. The HMC specimens were left under water for 2 d, then stored in sealed chambers with high level of MC above the water level for around 3 d, so that their MC steadily surpassed the fiber saturation point (FSP). The specimens were removed from their compartments only briefly before the tests to prevent moisture loss. Half of each group was tested in a way that the GO of the specimens was parallel to the direction of the hammer's movement. For the remaining specimens, the GO was positioned perpendicular to the direction of the hammer's movement. However, some studies showed that the GO has a negligible effect on certain aspects of the impact response of wood (Hassan Vand et al. 2024a, 2024b; Hassan Vand and Tippner 2023). Following testing, the specimens were placed in a drying oven at 103°C for 48 h to remove all moisture, enabling the determination of their oven-dry weight and exact MC.

To prepare the specimens, they were painted with a black-and-white random speckled pattern to improve the accuracy of the video extensometer and DIC (Pan et al. 2009). Just before the tests, the dimensions and weights of the specimens were measured. The tests were conducted at room temperature (≈20°C) in accordance with standards ČSN 490115 (Czech Technical Standard 1979), Wood: Determination of ultimate strength in flexure tests, and ČSN 490117 (Czech Technical Standard 1979), Wood: Impact strength in flexure. The tests were performed using a DPFest 400 drop-weight impact testing machine (Labortech s.r.o., CZ) with a displacement resolution of 10^{-5} m and a sampling frequency of 1 MHz. The reaction force was measured by an HBM force sensor from the CFTplus series (Hottinger Brüel & Kjaer, Austria). The weight of the hammer and its release height were 9.05 kg and 815.7 mm. This condition made the impact velocity 4 m/s, with 72.4 J of energy. Figure 1 shows a schematic of the specimens and clamps.

The samples were symmetrically positioned on two lower cylindrical support grips spaced 240 mm apart between their centerlines. Both the lower support grips and the upper impact hammer share identical geometric profiles, of a semi-cylindrical contact surface with a 15 mm radius and a lateral depth of 20 mm to match the specimen width. The upper impact hammer is aligned precisely at the mid-span (120 mm from each

Table 1. The physical and mechanical properties of the specimens and their test results. The median and CV% are in parentheses.

	Ash LMC	Ash HMC	Maple LMC	Maple HMC
MC (%)	11.0 (0.6)	55.5 (8.5)	10.55 (1.6)	62.2 (13.3)
Number of samples	35	11	15	15
Radial (mm)	20.1 (0.6)	20.9 (1.0)	20.1 (1.0)	20.6 (0.5)
Tangential (mm)	20.2 (0.7)	22.2 (0.8)	20.1 (0.7)	21.2 (0.8)
Length (mm)	300	300	300	300
Weight (g)	86.2 (3.1)	121.5 (5.3)	77.0 (2.1)	114.8 (5.1)
0% MC Weight (g)	77.5 (3.0)	77.2 (3.9)	70.1 (3.2)	69.9 (1.8)
Density (kg/m^3)	708.8 (3.2)	870.7 (6.1)	642.3 (2.0)	869.3 (5.0)
Max Deflection (mm)	8.5 (8.4)	8.2 (18)	8.6 (15.4)	9.1 (26.6)
Max Strain (–)	0.01266 (8.8)	0.01253 (16)	0.01465 (19.5)	0.01944 (23.4)
Max Force (N)	6899.5 (7.8)	5775.8 (13.7)	8967.8 (12.8)	3200.0 (12.2)
Absorbed Energy (J)	25.7 (16.4)	27.4 (18.0)	18.1 (19.2)	22.6 (37.8)
IBS (J/cm^2)	6.3 (17.0)	5.8 (18.0)	4.5 (19.5)	5.1 (37.9)

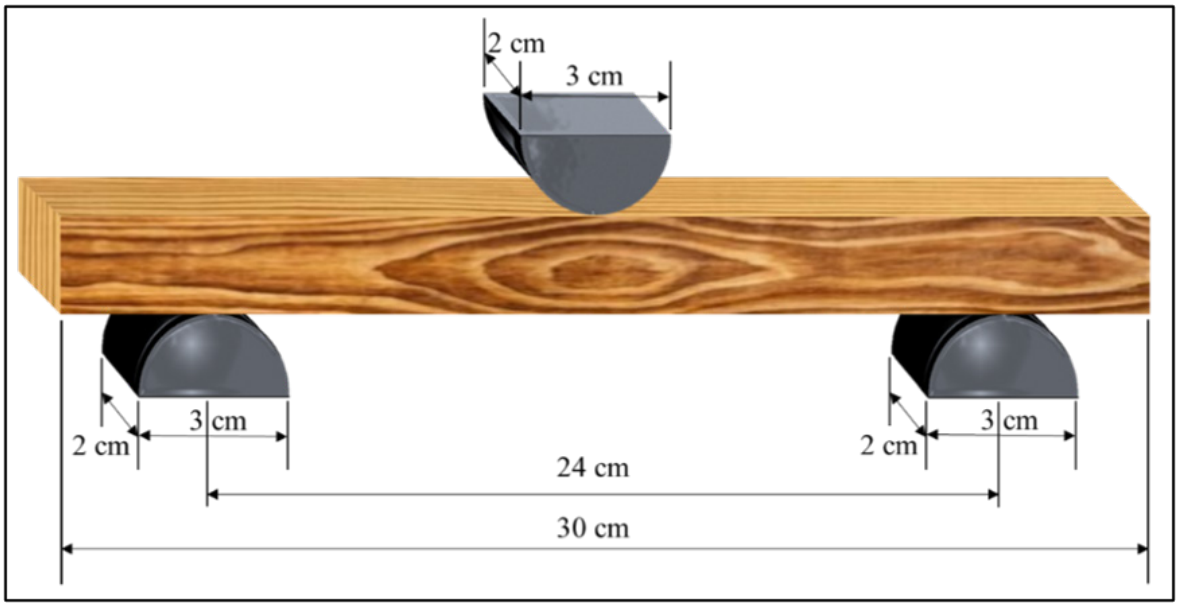


Figure 1. Schematic illustration of the three-point drop-weight impact bending test, the specimen dimensions, support span, impact hammer position, and loading configuration.

support centerline). The primary direction of impact is vertically downward, perpendicular to the longitudinal axis of the specimen. This induces a bending-dominated stress state at the mid-span, resulting in tensile stresses along the bottom surface and compressive stresses along the top surface of the beam profile.

The testing machine provides force vs. time charts and the total absorbed energy for breaking the specimens by integrating the force vs. displacement curves. All data curves were filtered directly by the built-in system of the impact testing machine. The output of charts had similar pattern but with different location for peaks and troughs. Thus, in order to calculate the median force-time curve accurately, minor misalignments required a slight extension or compression of the time scale (around 10% of total length). The value and timing of the maximum peak force were identified for each test, and the curves were adjusted so that all force peaks aligned at a single point. This synchronization ensures that the peaks and troughs of all curves line up correctly without distorting the data shape. Once the curves were synchronized, the median response was calculated for each time step.

A high-speed recording camera, FASTCAM SA-X2 type 1000K-M2 (Photron Cameras, Japan) alongside a mounted Nikon Micro-Nikkor G lens with a focal length of 105 mm (Nikon Corporation, Japan), was placed 1 m away at a perpendicular angle from the thickness-by-width specimens' surface. The camera recorded the impacts at 10,000 frames per second as black-and-white images of the central regions of the specimens, with a resolution of 768 × 328 pixels.

The recorded images were processed using Vic-2D v. 2010 (Correlated Solutions Inc., USA) DIC software. A simple 1D scale calibration with reference target of the thickness of the specimen was performed to determine the conversion factor, and a Lagrangian strain formulation was used to calculate strain tensors. The displacement field was considered 3×3 and the filter size was 5×5 points. The software could determine all point deformations, providing normal and shear strain distributions, as well as deflections, from the onset of impact to crack initiation in the specimens. Specimen deflection was measured by tracking the y-axis displacement of the beam's lowest point along its horizontal symmetry line. The maximum normal strain was also measured at the points where cracks initiated, which happened in the maximum deflection of each individual specimen. However, to mitigate noise, a small region around each point was used for strain determination rather than a single point.

For presenting a strain distribution pattern, the strains were captured at times corresponding to a chosen deflection of 4 mm. The strain distributions with values closest to the median and exhibiting more symmetrical form were selected as the typical strain distribution patterns. Additionally, the shear strain of the points along a multilinear probe located on the neutral axis of the samples was measured. DIC identified the neutral axis itself as the set of points with zero normal strain

for the images before crack initiation. The error of the DIC for measuring deflection and normal strain were 0.0073 mm and 0.00044, respectively. DIC error was estimated as the standard deviation of deflection and normal strain measurements obtained from stationary pre-impact images.

A 2-by-2 full factorial completely randomized design was used to analyze the effects of MC (LMC vs. HMC) and GO (radial vs. tangential) on the mechanical properties of both species by MATLAB R2025 (MathWorks, USA) using the official Statistics and Machine Learning Toolbox. To stabilize proportional variances inherent to timber testing under varying moisture loads, raw engineering data were transformed using the natural logarithm. Prior to analysis, residual normality and variance homogeneity were verified. A two-way ANOVA test was conducted (P-value = 0.05) to evaluate the main effects and the interaction effects. Significant localized variances were subsequently isolated using Tukey's post-hoc pairwise comparisons.

Results and discussion

Table 1 summarizes the specimens' basic parameters and test results based on the MC level and species type. The presented values are the median, and in parentheses, the coefficient of variation (CV%) of the physical properties as a percentage.

Alongside the median values of different parameters, the statistical analysis is needed to specify the effect of each setting on the results. The differences in medians do not necessarily indicate statistically significant group differences, and the difference between the groups can, in fact, be negligible. Based on the group density means and variances, the observed effect size was exceptionally large (Cohen's d for ash groups and maple groups was 3.12 and 6.56, respectively). This indicates a massive physical disparity between the two wood groups that far exceeds the standard deviation of the data, thus showing that the size of the groups was big enough.

To contextualize the experimental findings, the results of the density and IBS were compared against former studies about both ash and maple wood. Table 2 presents the IBS and density of the former studies; and the difference between their results and this study for each article is shown in the parentheses. Across the cited studies, both ash and maple wood exhibited a more consistent density profile, yet their IBS values varied drastically, with the highest reported values nearly double the lowest. This suggests that for ash, density alone is a poor predictor of dynamic toughness, and the wide fluctuations in the coefficients of variation point to significant discrepancies in wood quality, grain orientation, or testing conditions among research studies.

Prior to analyzing the mechanical results, we verified the data rules for ANOVA using Table 3. For an ANOVA to be accurate, the data should follow a normal distribution shape and have suitable group spreads, with consideration of the MC and GO separations. The natural log transformation worked exceptionally well, successfully validating both rules ($p > 0.05$) for 80% of the experimental runs. There were only two minor exceptions. First, European ash deflection did not have perfectly equal spreads ($p = 0.0053$) due to natural variations in wood. However, because its data shape was highly normal ($p = 0.9442$), the ANOVA test was retained because residual distributions showed acceptable behavior. Second, sycamore maple F_{max} was slightly outside the ideal normal shape ($p = 0.0472$), but its group spreads are acceptable ($p = 0.5514$). Because the residual distributions exhibited high normality, the ANOVA framework remains robust despite the unequal sample sizes between the ash moisture groups.

The effects of MC, GO, and their interaction (MC × GO) on the impact bending characteristics of ash and maple wood are presented in Table 4. The two-way ANOVA results revealed

Table 2. Comparison of density and IBS obtained in the present study with values reported in previous studies. Values in parentheses indicate the percentage difference relative to the present study.

Study	Species	Density	IBS (J/cm²)
Kielmann et al. 2013	Ash	645 (9%)	2.6 (58%)
Brischke 2017	Ash	-	7.4 (17%)
Borůvka et al. 2020	Ash	655 (7%)	7.3 (16%)
Fortin-Smith et al. 2016a	Ash	-	5.0 (8%)
Fortin-Smith et al. 2016a	Maple	-	5.3 (16%)
Kollmann and Côté 1968	Maple	630 (2%)	6.4 (42%)
Kielmann et al. 2013	Maple	670 (4%)	3.6 (20%)
Von Wedel 1964	Maple	600 (7%)	5.2 (16%)
Sell 1968	Maple	635 (1%)	6.4 (42%)
Wagenführ 2007	Maple	630 (2%)	6.5 (44%)

Table 3. Validation of ANOVA assumptions using Levene's test for homogeneity of variance and normality tests for the log-transformed data.

Column1	Ash		Maple	
	Levene	Normality	Levene	Normality
Max Def	0.0053	0.9442	0.1684	0.8061
Max strain	0.2368	0.7907	0.7074	0.9781
F_{max}	0.1662	0.3892	0.5514	0.0472
Absorbed energy	0.2389	0.9040	0.3752	0.7284
IBS	0.1828	0.7565	0.7046	0.6045

Table 4. Results of the two-way ANOVA evaluating the effects of MC, GO, and their interaction (MC × GO) on the mechanical properties.

Material and metric	Source of variation	df	Mean square (MS)	F-value	p-value	Significance
Ash deflection	MC	1	0.0040	0.2865	0.5955	ns
	GO	1	0.0007	0.0502	0.8239	ns
	MC*GO	1	0.0173	1.2472	0.2709	ns
Maple deflection	MC	1	0.3302	6.9155	0.0142	*
	GO	1	0.0004	0.0078	0.9301	ns
	MC*GO	1	0.0111	0.232	0.6341	ns
Ash max strain	MC	1	0.0043	0.3805	0.5408	ns
	GO	1	0.0174	1.5508	0.2203	ns
	MC*GO	1	0.0020	0.1752	0.6778	ns
Maple max strain	MC	1	0.3290	4.9986	0.0342	*
	GO	1	0.0019	0.0285	0.8672	ns
	MC*GO	1	0.0014	0.0211	0.8856	ns
Ash F_{max}	MC	1	0.1967	33.1742	< 0.0001	***
	GO	1	0.1426	24.0591	< 0.0001	***
	MC*GO	1	0.0417	7.0272	0.0114	*
Maple F_{max}	MC	1	7.9241	387.071	< 0.0001	***
	GO	1	0.0077	0.3753	0.5454	ns
	MC*GO	1	0.0026	0.1289	0.7224	ns
Ash absorbed energy	MC	1	0.0070	0.2604	0.6125	ns
	GO	1	0.0928	3.434	0.0709	ns
	MC*GO	1	0.0514	1.9023	0.1751	ns
Maple absorbed energy	MC	1	0.4047	4.1808	0.0511	ns
	GO	1	0.0116	0.1202	0.7316	ns
	MC*GO	1	0.0184	0.1902	0.6663	ns
Ash IBS	MC	1	0.0888	3.1771	0.0819	ns
	GO	1	0.0896	3.2039	0.0807	ns
	MC*GO	1	0.0539	1.9259	0.1725	ns
Maple IBS	MC	1	0.0479	0.6689	0.4212	ns
	GO	1	0.0035	0.0494	0.8259	ns
	MC*GO	1	0.0937	1.3082	0.2635	ns

Significance indicators are as ns = $p \geq 0.05$, * = $p < 0.05$, ** = $p < 0.01$, and *** = $p < 0.001$.

that most of the investigated parameters were not significantly affected by MC, GO, or their interaction. For ash wood, maximum deflection and maximum strain showed no significant influence of any investigated factor ($p > 0.05$). In contrast, F_{max} was significantly affected by both MC and GO, with highly significant effects observed for MC ($F = 33.174$, $p < 0.0001$) and GO ($F = 24.059$, $p < 0.0001$). Additionally, a significant interaction between MC and GO was observed for F_{max} ($F = 7.027$, $p = 0.0114$), indicating that the influence of MC on the maximum force depended on the GO. Absorbed energy and IBS of ash wood were not significantly affected by the studied factors, although GO showed a tendency toward influencing these properties ($p = 0.0709$ and $p = 0.0807$, respectively).

For maple wood, MC significantly influenced maximum deflection ($F = 6.916$, $p = 0.0142$) and maximum strain ($F = 4.999$, $p = 0.0342$), while GO and the MC × GO interaction had no significant effects on these parameters. Similar to ash wood, F_{max} was strongly affected by MC ($F = 387.071$, $p < 0.0001$), whereas GO and the interaction effect were not significant. The effects of MC, GO, and their interaction on absorbed energy and IBS were statistically insignificant for maple wood ($p > 0.05$), although MC showed a marginal effect on absorbed energy ($F = 4.181$, $p = 0.0511$). Overall, MC was identified as the dominant factor affecting the maximum force response of both wood species, whereas its influence on energy absorption and impact bending strength was statistically insignificant. GO contributed mainly to the maximum force response of ash wood.

The contrasting impact behaviors of European ash and sycamore maple are not only due to density alone, but are also rooted in their distinct microstructural structures. European

ash features a ring-porous anatomical structure characterized by heavily densified latewood bands with a high fiber-to-parenchyma ratio. Under rapid impact stress, these dense fiber matrices can act as critical crack-arresting barriers. Conversely, sycamore maple possesses a diffuse-porous structure with smaller, uniformly distributed vessels, a lower fiber ratio, and prominent wood rays. These fundamental differences between the structures, can have a great effect on the impact response of wood. This requires a more comprehensive further study that includes the micro assessment of the structures of each specimen, alongside its impact response.

The mechanical response of both species is heavily influenced by the transition through the FSP. In the LMC groups, the presence of bound water within the cell walls acts as bonding water between wood polymers. On the other hand, the MC in both HMC groups significantly exceeded the FSP. At this stage, the cell walls are fully saturated and plasticized, and any additional moisture exists as free water in the cell lumens, which does not further reduce the strength of the cell wall matrix. The pattern of increasing MC more than FSP can be seen in former studies (Hassan Vand et al. 2024; Hassan Vand and Tippner 2024a, 2024b) where IBS, maximum deflection, and maximum strain increased with elevated MC, while maximum force drastically decreased.

The values of the maximum normal strain and deflection measured by DIC are shown in Figures 2 and 3 as boxplots. The center horizontal line within each box denotes the median value, while the (×) marker represents the sample mean. The box boundaries define the interquartile range (IQR) from the 25th to the 75th percentile. The whiskers extend to the maximum

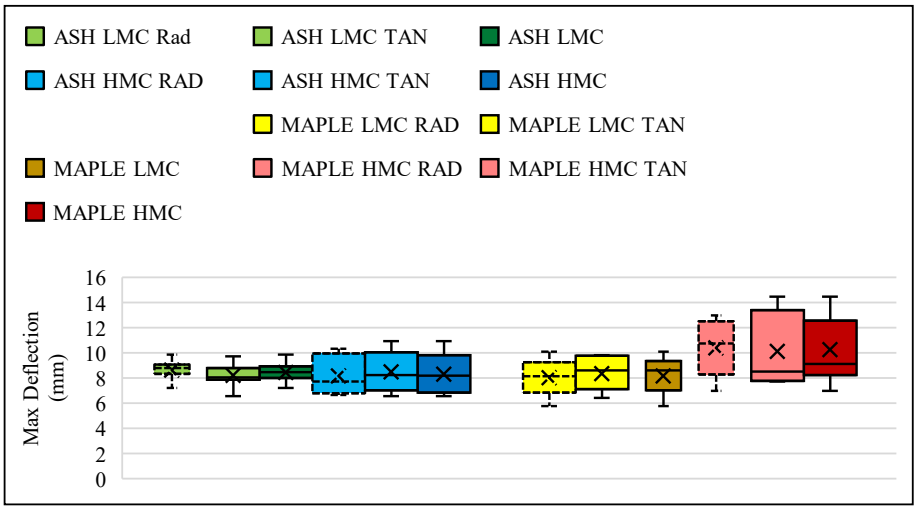


Figure 2. Maximum mid-span deflection measured by DIC up to crack initiation for both species under different MC and GO.

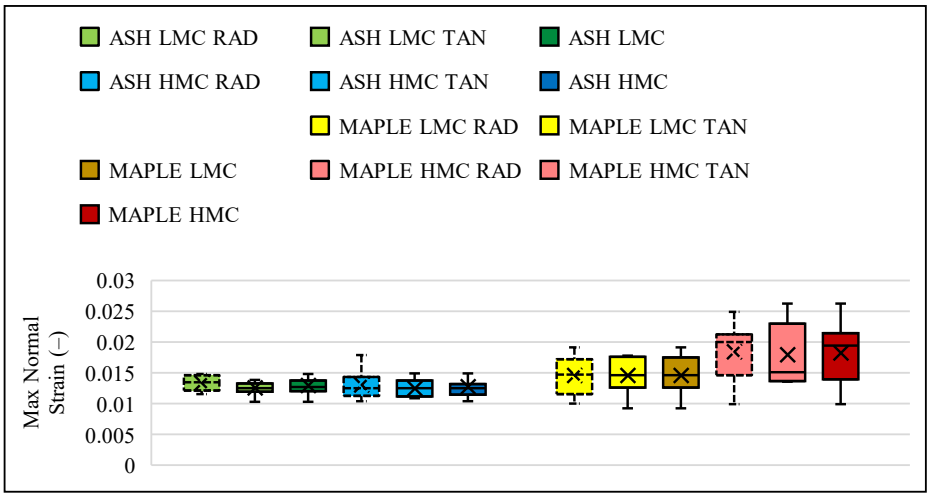


Figure 3. Maximum normal strain measured by DIC up to crack initiation for both species under different MC and GO.

and minimum data points within 1.5 IQR from the box edge; individual data points falling beyond this range are plotted as distinct outlier dots. From Figure 2, it can be seen that the ash deflection is unaffected by increasing MC. In contrast, for the maple, the increase in the MC significantly increases the flexibility. The GO also showed no influence over the flexibility of both species for both MC levels. The maximum normal strain has almost the same pattern as the maximum deflection. The maximum deflection for LMC of both species was similar, while for HMC, the ash showed no difference, whereas the maple showed improvement in deflection.

Figure 4 displays the maximum reaction force of the specimens. Boxplot parameters such as the median, mean, IQR, and whiskers follow the definitions established in Figure 2. It is clear that an increase in MC consistently decreases the maximum force for all specimens, while GO generally had no influence on the maximum force for either species at both MC levels, except for ash HMC. Notably, the effect of MC on ash, with 16% decrease, was far less pronounced compared to its effect on maple wood, with 64% decrease of the F_{max}.

Figures 5 and 6 display the median of all charts for reaction forces vs. time of all groups. To highlight their similarities and differences, the median values for the LMC and HMC groups of both species are plotted side by side.

The dynamic impact response of both ash and maple wood specimens can be distinctly categorized into three sequential chronological stages. During Stage I (0 to 0.001 s), initial contact with the impact hammer induced a rapid, highly oscillatory force peak dominated by inertial shock waves passing through the specimen and test fixtures, which subsequently stabilized into a linear elastic trend. As loading transitioned into Stage II (0.001 to 0.0025 s), the curves diverged sharply based on MC, capturing progressive micro-cracking and fiber fracture. LMC specimens climbed to a drastically high, sharp peak indicative of a rigid, brittle matrix, before experiencing sudden force drops from unstable macro-crack propagation; whereas

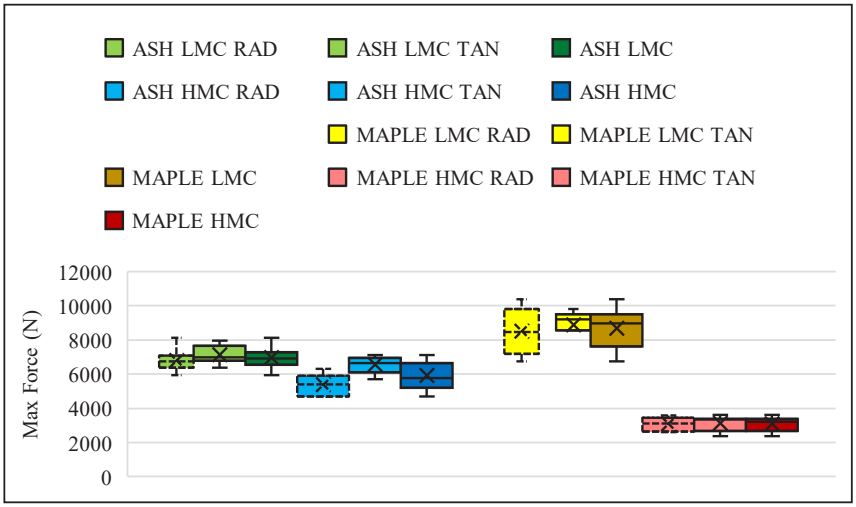


Figure 4. The maximum reaction force of the species as measured by the testing machine.

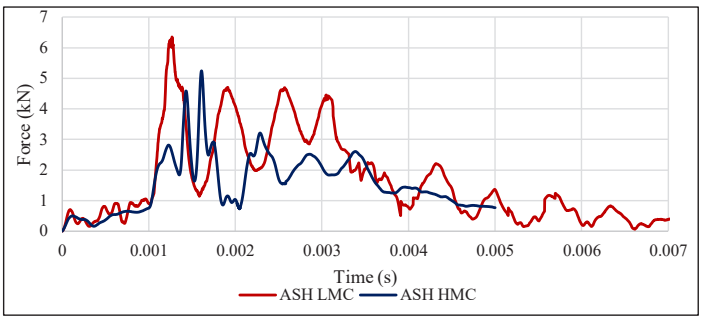


Figure 5. Median reaction force-time curves for ash specimens under low and high moisture contents. Curves represent the synchronized median responses obtained from all impact tests.

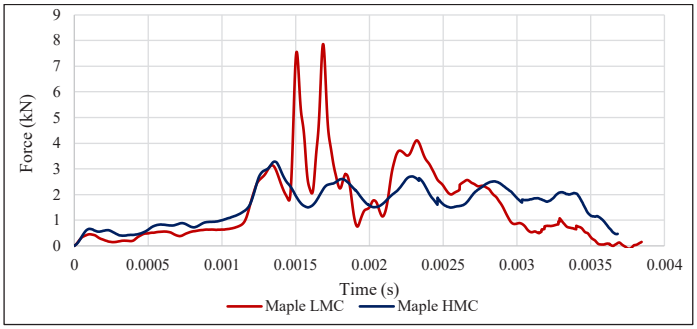


Figure 6. Median reaction force-time curves for maple specimens under low and high moisture contents. Curves represent the synchronized median responses obtained from all impact tests.

HMC specimens displayed significantly attenuated, smoother, and temporally delayed peaks representing a compliant, ductile failure mode. Finally, Stage III (0.0025 to the end) represents the post-peak degradation phase where load-bearing capacity decayed as macro-cracks fully cleaved the cross-section; here, LMC curves continued to show high-frequency force oscillations from splintering and friction, while the HMC curves decayed much more smoothly due to the structural damping qualities of the moisture-saturated cellular matrix.

The sharp contrast between the brittle failure of LMC specimens and the ductile response of HMC specimens highlights a vital safety trade-off. While LMC timber achieved significantly higher peak load capacities, its failure was instantaneous and catastrophic, offering no visual or structural warning signs. Conversely, while HMC timber had smaller peak strength, its prolonged deformation and smoother post-peak degradation provided a more compliant, progressive failure mode. In structural applications exposed to sudden impact risks (such as protective barriers, seismic-resistant designs, or rockfall shelters), a predictable, ductile deformation mode is often preferred over sudden, brittle snapping.

The primary strength-related parameter in impact loading is the amount of absorbed energy, or its dimensionless counterpart, IBS. Figures 7 and 8 illustrate the absorbed energy and IBS for all groups. Boxplot parameters such as the median, mean, IQR, and whiskers follow the definitions established in Figure 2.

Figure 7 reveals that ash generally exhibited a higher total absorbed energy than maple, and interestingly, MC had no significant effect on the ability of ash to absorb inflicted energy. Conversely, maple demonstrated a lower capacity to absorb energy, though increasing its MC marginally improved this capacity.

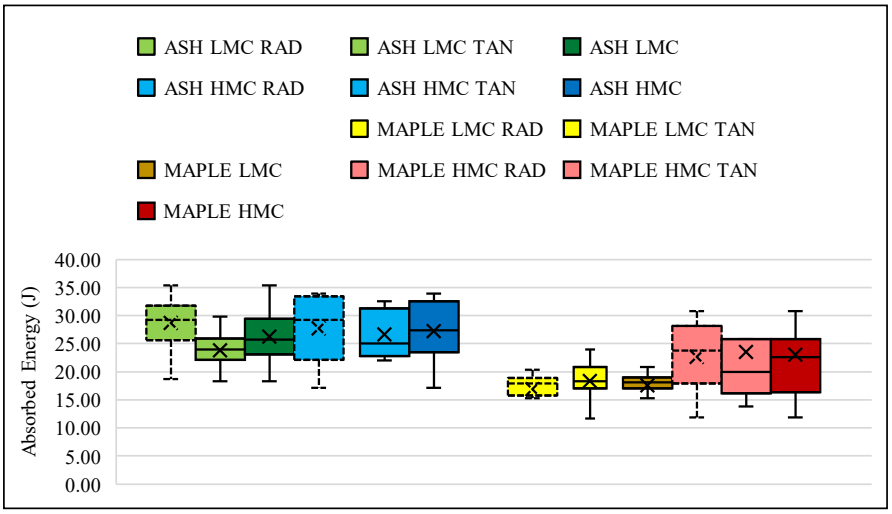


Figure 7. The absorbed energy of the species.

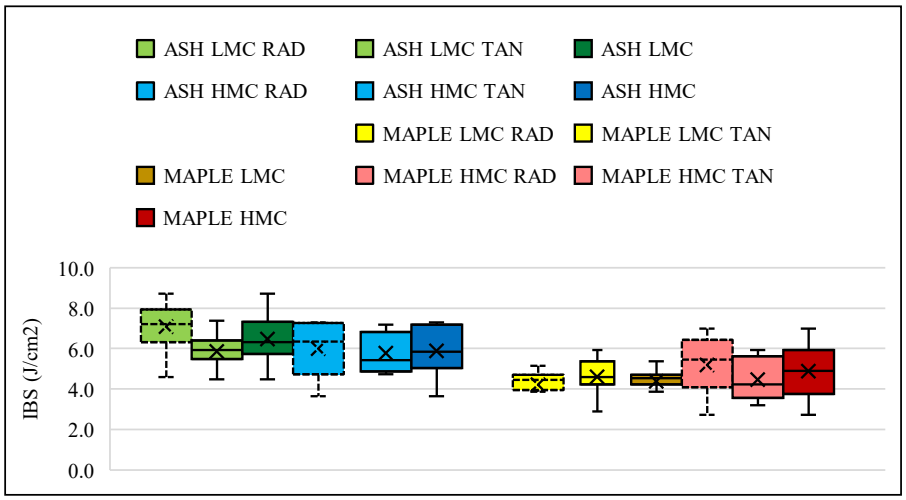


Figure 8. The IBS of the species.

Figure 8 presents the IBS values for the groups. It is important to note that the difference between IBS and absorbed energy arises from the cross-section of the specimens. Specifically, the cross-section of ash and maple specimens increased by 14% and 8%, respectively, with increased MC. This means the specimens' MC can considerably alter IBS values without affecting the absorbed energy. For example, the IBS of ash-HMC was lower than that of ash-LMC, even though the total absorbed energy of ash-HMC was higher than that of ash-LMC.

The strain distribution of each group was measured, and the strain distributions are presented in Figures 9 to 12. These strain distribution patterns can be used for validating the respective models. Both the normal and shear strain distributions were determined at 4 mm deflection. The figures reveal a symmetrical normal strain distribution. For the normal strain, the map displays the normal strain distribution illustrating compressive behavior at the top edge (purple/blue) and tensile behavior at the bottom edge (red). The highest compressive strain was observed under the impact region, close to the hammer. Conversely, the highest tensional strain, where cracks invariably initiate, was located in the central region, at the bottom of the sample. For shear strain, peaks were near the neutral axis and concentrated in the regions between the central impact hammer and the outer support grips. The distribution

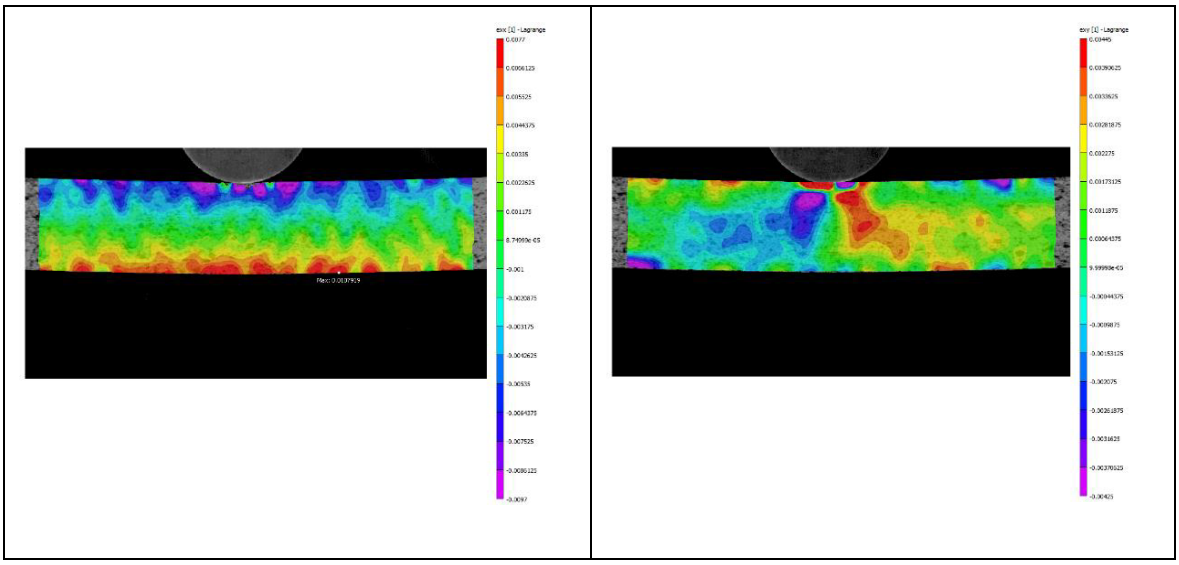


Figure 9. Representative strain distributions (DIC maps) for ash LMC specimens at a 4 mm mid-span deflection.

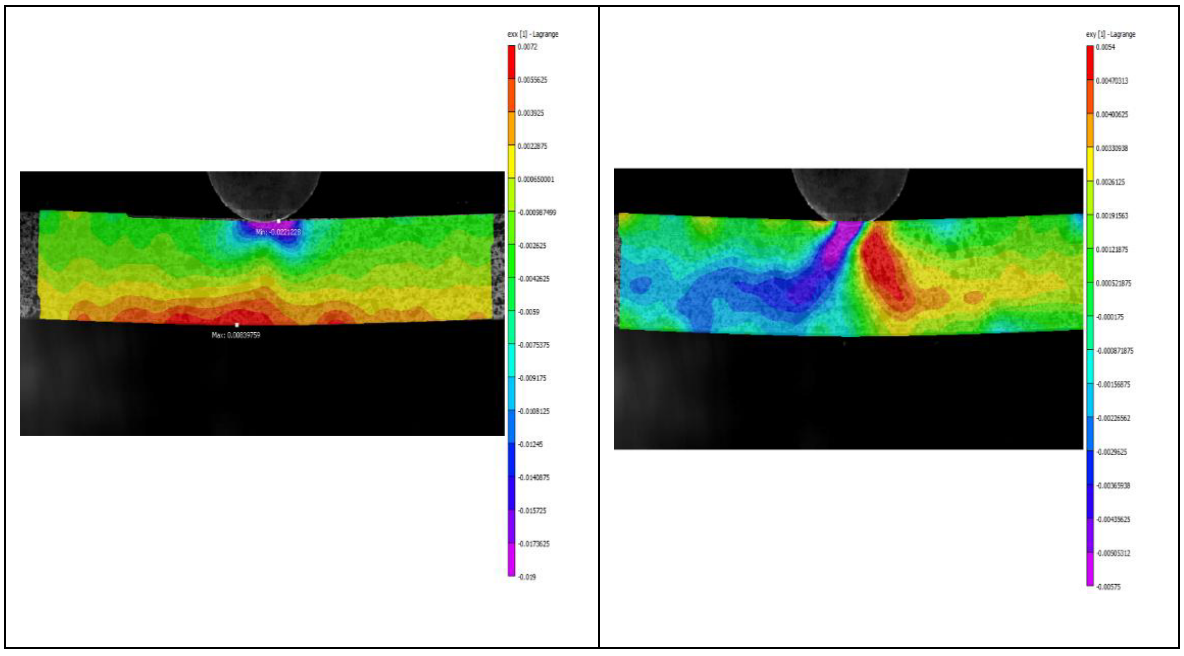


Figure 10: Representative strain distributions (DIC maps) for ash HMC specimens at a 4 mm mid-span deflection.

typically shows a clear anti-symmetric pattern, with positive and negative shear gradients splitting down the center line of the impact point. The displayed maps are taken from a single representative specimen chosen because its maximum peak force and symmetrical pattern matched the calculated median values of that group.

The shear strain distribution along the neutral axis was also determined using DIC, as shown in Figure 13. Figure 14 further illustrates the "maximum absolute shear strain" on the neutral axis of the beams. Boxplot parameters such as the median, mean, IQR, and whiskers follow the definitions established in Figure 2.

Along the neutral axis of the specimen, the shear strain distribution exhibited a highly distinct, anti-symmetric profile across the span as the material approached crack initiation. The shear strain peaks in the positive direction at between the outer support grips and the central loading point, rapidly dropped through zero directly beneath the central impact hammer, and reached a corresponding negative peak on the opposite symmetrical point. This sharp inversion from positive to negative shear gradients highlights the intense localized shear concentrations driving material deformation right before failure. Furthermore, the higher MC in the HMC specimen yielded visibly higher peak shear strain values compared to the LMC specimen, indicating

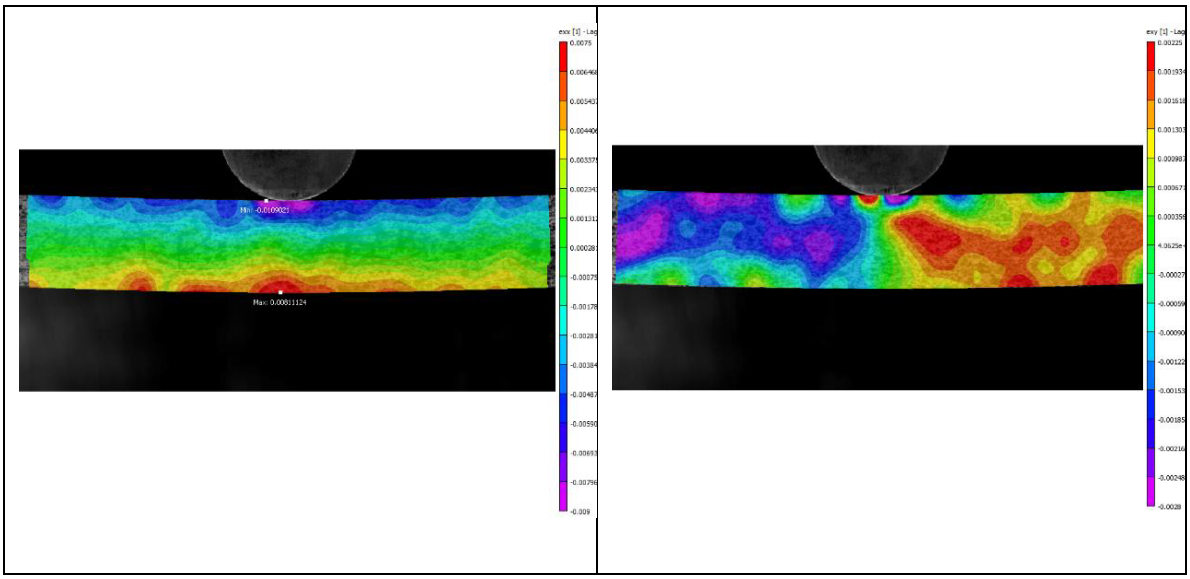


Figure 11. Representative strain distributions (DIC maps) for maple LMC specimens at a 4 mm mid-span deflection.

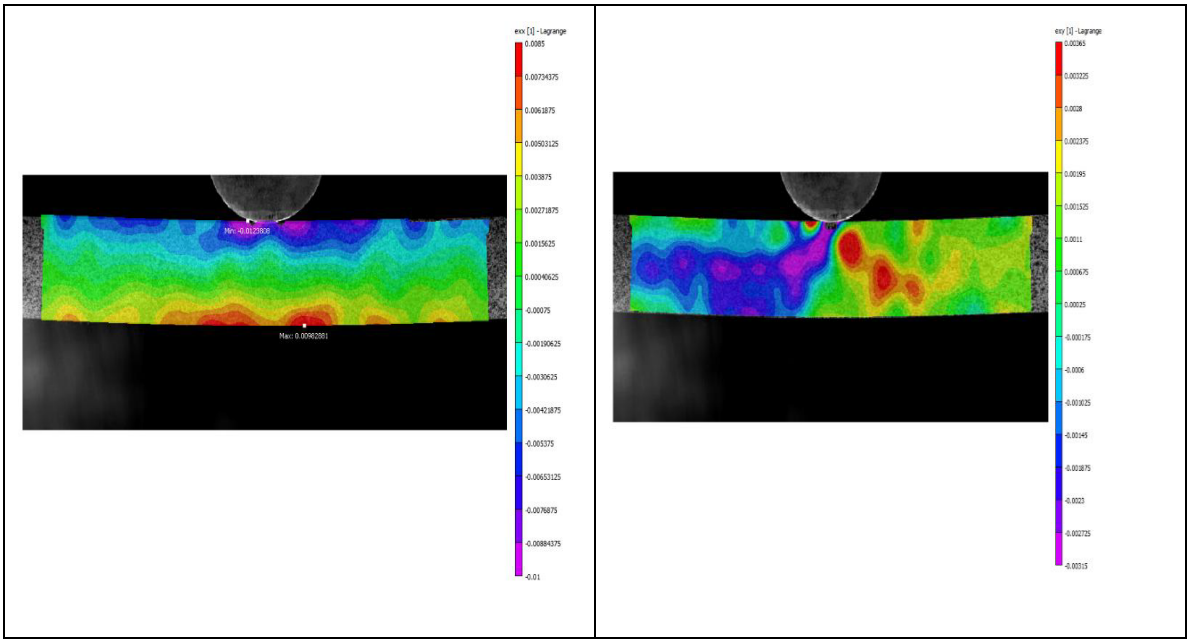


Figure 12. Representative strain distributions (DIC maps) for maple HMC specimens at a 4 mm mid-span deflection.

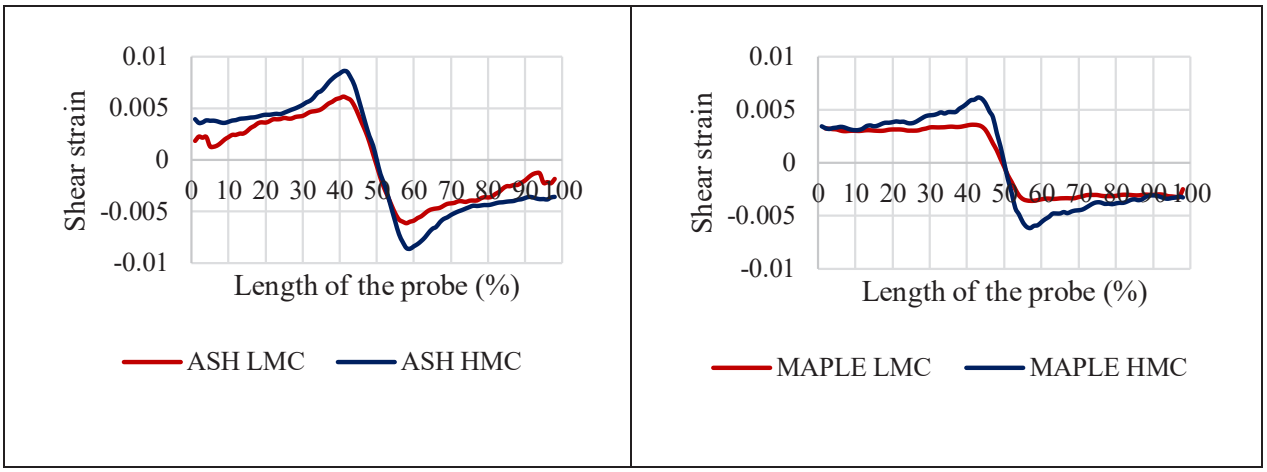


Figure 13. Shear strain distribution along the neutral axis of ash and maple beams across varying moisture levels.

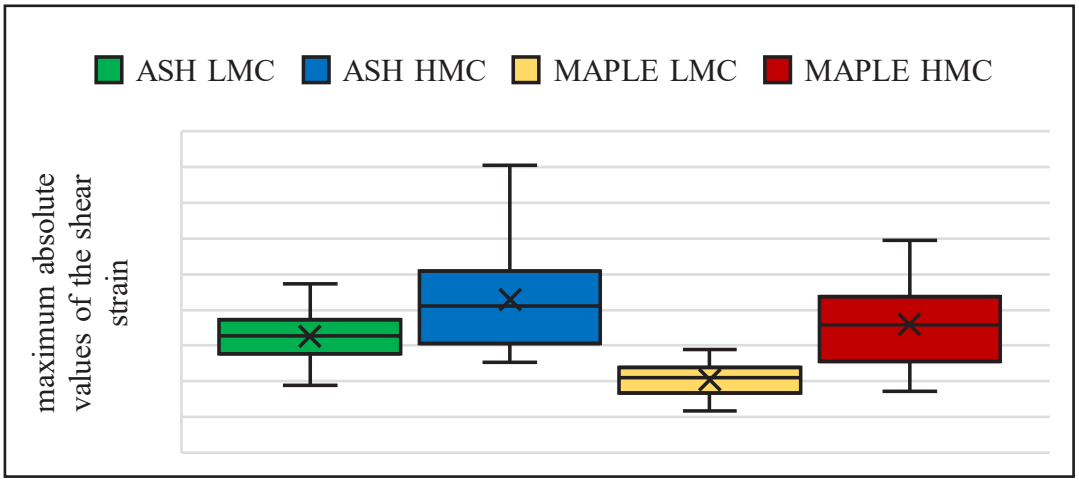


Figure 14. The maximum absolute values of the shear strain distribution over the neutral axis of the specimens.

increased material compliance and greater shear deformation prior to structural cracking.

While this study provides high-resolution insights into the dynamic behavior of European ash and sycamore maple using advanced DIC, certain limitations of this study must be acknowledged. First, the experimental design focused on two distinct moisture extremes—low moisture content, around 12% MC, and high moisture content far exceeding the FSP. Lack of assessment for other MC levels made it unable to determine the non-linear transition profiles of mechanical properties directly before, around, and after FSP. Second, while the macro-scale impact metrics and surface strain fields were successfully captured, localized internal microstructural failure mechanisms, including the influence of structural characteristics of each specimen of both species, were not investigated.

Conclusion

This research provides critical insights into the impact performance of European ash and sycamore maple, emphasizing their distinct sensitivities to moisture and GO. Consequently, a better, optimized design ultimately leads to more efficient and reliable wooden structures and products. The research confirmed ash wood's superior general impact strength and energy absorption, consistent with its widespread use in demanding applications. Notably, absorbed energy of ash remained largely unaffected by increased MC, although mechanical properties of maple, including deflection, maximum strain, and maximum force, were significantly influenced by changes in MC. The effects of GO diminished significantly in higher MC conditions for ash, while sycamore maple exhibited a more isotropic behavior regarding GO across all MC levels. The distinction between

absorbed energy and IBS was also highlighted, demonstrating that changes in specimen cross-section due to MC can independently affect IBS values, independent of total absorbed energy. The IBS of ash for lower MC levels was from 6.3 J/cm^2, whereas it reached 5.8 J/cm^2 for higher MC levels, showing an 8% decrease. For maple wood, IBS from 4.5 J/cm^2 for LMC group increased to 5.1 J/cm^2 for the HMC group, showing a 13% increase.

Another output of the study was a detailed strain distribution pattern obtained via DIC, including normal and shear strains at a certain level of deflection. Also, the shear strain of the points on the neutral axis was presented. These results offered invaluable data for validating and refining numerical models of wood behavior under dynamic loading.

The structural design of timber elements must dynamically adjust safety factors to account for moisture-induced plasticization, as high moisture content drastically degrades peak load capacity, while shifting failure from brittle to a more progressive, ductile mode. Furthermore, because GO showed negligible statistical influence on deflection, quality control in impact-critical structures should prioritize managing moisture and species thresholds over GO alignment during material selection.

Future work should further elucidate the underlying microstructural mechanisms driving these observed macroscopic responses and explore the influence of other environmental factors via tools such as X-ray computed tomography to correlate anatomical structure with impact response in areas of high deformation.

Acknowledgements

This work was supported by the Ministry of Education Youth and Sports in the Czech Republic [Grant Number #LL1909, ERC CZ].

References

Acuña L, Sepliarsky F, Spavento E, Martínez RD, Balmori JA (2020) Modelling of impact falling ball test response on solid and engineered wood flooring of two *Eucalyptus* species. Forests 11(9):933. https://www.mdpi.com/808558

Baumann G, Brandner R, Müller U, Stadlmann A, Feist F (2021) A comparative study on the temperature effect of solid birch wood and solid beech wood under impact loading. Materials 14(24):7616. https://doi.org/10.3390/ma14247616

Bodziarczyk J, Lesiński J (2011) Sycamore maple forests in Poland-a review. https://www.cabidigitallibrary.org/doi/full/10.5555/20123105506

Borůvka V, Novák D, Šedivka P (2020) Comparison and analysis of radial and tangential bending of softwood and hardwood at static and dynamic loading. Forests 11(8):896. https://www.mdpi.com/801256

Boshier D, Cordero J, Harris S, Pannell J, Rendell S, Savill P, Stewart J, Cundall N, Hubert J, Samuel S et al. (2005) Ash species in Europe: biological characteristics and practical guidelines for sustainable use. Oxford: Department of Plant Sciences, Oxford Forestry Institute, University of Oxford.

Bragov A, Igumnov L, dell'Isola F, Konstantinov A, Lomunov A, Iuzhina T (2020) Dynamic testing of lime-tree (*Tilia Europoea*) and pine (*Pinaceae*) for wood model identification. Materials 13(22):5261. https://www.mdpi.com/897314

Brischke C (2017) Interrelationship between static a Nd dynamic strength properties of wood and its structural integrity. Drvna industrija 68(1):53–60. https://hrcak.srce.hr/clanak/263383

Campshure B, Drane P, Sherwood J (2020) June. An Investigation of Maple Wood Baseball Bat Durability as a Function of Bat Profile Using LS-DYNA. In Proceedings of the 16th International LS-DYNA Users Conference (pp. 10–11). https://lsdyna.ansys.com/16th-international-ls-dyna-conference/

Choi D, Thorpe JL, Hanna RB (1991) Image analysis to measure strain in wood and paper. Wood Science And Technology 25(4):251–262. https://link.springer.com/article/10.1007/BF00225465

Czech Technical Standard (1979) ČSN 490115. Wood: Determination of ultimate strength in flexure tests. https://eshop.agentura-cas.cz/Detailnormy.aspx?k=4257

Czech Technical Standard (1979) ČSN 490117. Wood: Impact strength in flexure. https://eshop.agentura-cas.cz/Detailnormy.aspx?k=4259

Clauß S, Pescatore C, Niemz P (2014) Anisotropic elastic properties of common ash (*Fraxinus excelsior* L.). Holzforschung 68(8):941–949. https://www.degruyterbrill.com/document/doi/10.1515/hf-2013-0189/html

Dinulica F, Savin A, Stanciu MD (2023) Physical and acoustical properties of wavy grain sycamore maple (*Acer pseudoplatanus* L.) used for musical instruments. Forests 14(2):197. https://www.mdpi.com/2084164

Dobrowolska D, Hein S, Oosterbaan A, Wagner S, Clark J, Skovsgaard JP (2011) A review of European ash (*Fraxinus excelsior* L.): implications for silviculture. Forestry 84(2):133–148. https://doi.org/10.1093/forestry/cpr001

Fortin-Smith J, Sherwood J, Drane P, Kretschmann D (2016a) A Complementary Experimental and Modeling Approach for the Characterisation of Maple and Ash Wood Material Properties for the Bat/Ball Impact Modeling in LS-DYNA. In 14th International LS-DYNA Users Conference. https://lsdyna.ansys.com/14th-international-ls-dyna-conference/

Fortin-Smith J, Sherwood J, Drane P, Kretschmann D (2016b) Characterisation of maple and ash material properties as a function of wood density for bat/ball impact modeling in LS-DYNA. Procedia engineering 147:413–418. www.sciencedirect.com/science/article/pii/S1877705816307780

Fortin-Smith J, Sherwood J, Drane P, Kretschmann D (2018) Characterisation of maple and ash material properties for the finite element modeling of wood baseball bats. Appl Sci 8(11):2256. https://www.mdpi.com/366146

Gerhards CC (1977) Effect of duration and rate of loading on strength of wood and wood-based materials. USDA for serv research paper FPL 283, USDA For Serv Forest Products Laboratory, Madison, WI, United States.

Gilman FE, Watson GD (1993) *Acer pseudoplatanus* L. Sycamore Maple, Fact Sheet ST-40, USA. https://doi.org/10.32473/EDIS-ST040-1993

Glass S, Zelinka S (2021) Moisture relations and physical properties of wood. Chapter 4 in FPL-GTR-282, pp.4–1.

Gutkowski RM, Shigidi AM, Peterson ML (2007) Dynamic impact load tests of a bridge guardrail system (No. MPC Report No. 07-188). Fargo: Mountain-Plains Consortium.

Hassan Vand M, Tippner J (2023) Impact bending strength of thermally-modified timber. Holzforschung 77(11–12):828–837. https://www.degruyterbrill.com/document/doi/10.1515/hf-2023-0046/html

Hassan Vand M, Tippner J (2024a) The effect of moisture content over the fibre saturation points on the impact strength of wood. R Soc Open Sci 11(2). https://royalsocietypublishing.org/rsos/article/11/2/231685/92484

Hassan Vand M, Tippner J (2024b) Effects of moisture content on the behaviour of Scots pine heartwood and sapwood under impact. J Wood Sci 70(1):39. https://doi.org/10.1186/s10086-024-02152-2

Hassan Vand M, Tippner J, Brabec M (2024) Effects of species and moisture content on the behaviour of solid wood under impact. Eur J Wood Wood Prod 82(1):23–34. https://link.springer.com/article/10.1007/s00107-023-01986-9

Iliev N, Varbeva L, Alexandrov N (2022) Silvicultural aspects of the sycamore (*Acer pseudoplatanus* L.) propagation–Overview. Silva Balc 23(1):37–55. https://silvabalcanica.pensoft.net/article/82756/download/pdf/

Kielmann BC, Militz H, Mai C, Adamopoulos S (2013) Strength changes in ash, beech and maple wood modified with a N-methylol melamine compound and a metal-complex dye. Wood Res 58(3):343–350. www.woodresearch.sk/wr/201303/02.pdf

Keunecke D, Novosseletz K, Lanvermann C, Mannes D, Niemz P (2012) Combination of X-ray and digital image correlation for the analysis of moisture-induced strain in wood: opportunities and challenges. Eur J Wood Wood Prod 70(4):407–413. https://link.springer.com/article/10.1007/s00107-011-0573-8

Kollmann FFP, Côté WA (1968) Principles of Wood Science and Technology: I Solid Wood. Berlin, Heidelberg: Springer. Available at: https://doi.org/10.1007/978-3-642-87928-9

Kretschmann D (2010) Mechanical properties of wood. Wood handbook: wood as an engineering material: chapter 5. Centennial ed. General technical report FPL; GTR-190. Madison, WI: US Dept. of Agriculture, Forest Service, Forest Products Laboratory: p. 5.1–5.46., 190, pp.5–1. https://research.fs.usda.gov/treesearch/62243

Liu D, Chen Y (2010) The impact behavior of ecofriendly cellulosic fiber-based packaging composites. Wood Fiber Sci 42(4):460–466. https://wfs.swst.org/index.php/wfs/article/view/499

Moreira AP, Silveira ED, Almeida DHD, Almeida THD, Panzera TH, Christoforo AL, Rocco FA (2017) Toughness and impact strength in dynamic bending of wood as a function of the modulus of elasticity and the strength in compression to the grain. Int J Mater Eng 7(4):61–67. https://doi.org/10.5923/j.ijme.20170704.01

Niemz P, Clauss S, Michel F, Hansch D, Hansel A (2014) Physical and mechanical properties of common ash (*Fraxinus excelsior* L.). Wood Res 59(4):671–682. https://hdl.handle.net/20.500.11850/90545

Olmedo I, Bourrier F, Bertrand D, Toe D, Berger F, Limam A (2015) Experimental analysis of the response of fresh wood stems subjected to localized impact loading. Wood Sci Technol 49:623–646. https://doi.org/10.1007/s00226-015-0713-0

Pan B, Qian K, Xie H, Asundi A (2009) Two-dimensional digital image correlation for in-plane displacement and strain measurement: a review. Meas Sci Technol 20(6):062001. https://doi.org/10.1088/0957-0233/20/6/062001

Pasta S, de Rigo D, Caudullo G (2016) *Acer pseudoplatanus* in Europe: distribution, habitat, usage and threats. In: San-Miguel-Ayanz J, de Rigo D, Caudullo G, Houston Durrant T, Mauri A (Eds), European Atlas of Forest Tree Species. Luxembourg: Publ. Off. EU, p.e01665a. https://forest.jrc.ec.europa.eu/en/european-atlas/

Pautasso M, Aas G, Queloz V, Holdenrieder O (2013) European ash (*Fraxinus excelsior*) dieback–A conservation biology challenge. Biol Conserv 158:37–49. https://doi.org/10.1016/j.biocon.2012.08.026.

Polocoşer T, Kasal B, Stöckel F (2017) State-of-the-art: intermediate and high strain rate testing of solid wood. Wood Sci Technol 51:1479–1534. https://doi.org/10.1007/s00226-017-0925-6

Polocoşer T, Kasal B, Stöckel F, Li X (2018) Dynamic material properties of wood subjected to low-velocity impact. Mater Struct 51:1–16. https://doi.org/10.1617/s11527-018-1186-z

Polocoşer T, Stöckel F, Kasal B (2016) Low-velocity transverse impact of small, clear spruce and pine specimens with additional energy absorbing treatments. J Mater Civ Eng 28(8):04016048. https://ascelibrary.org/doi/abs/10.1061/(ASCE)MT.1943-5533.0001545

Sahraoui S, Lataillade JL (1998) Analysis of load oscillations in instrumented impact testing. Eng Fract Mech 60(4):437–446. https://www.sciencedirect.com/science/article/pii/S0013794498000241

Sedlar T, Šefc B, Stojnić S, Sinković T (2021) Wood quality characterisation of sycamore maple (*Acer pseudoplatanus* L.) and its utilisation in wood products industries. Croat J For Eng: Journal for Theory and Application of Forestry Engineering 42(3):543–560. https://hrcak.srce.hr/clanak/381464

Sell J (1968) *Eigenschaften und Kenngrössen von Holzarten*. Switzerland: Lignum, Schweizerische Arbeitsgemeinschaft für das Holz.

Sonderegger W, Martienssen A, Nitsche C, Ozyhar T, Kaliske M, Niemz P (2013) Investigations on the physical and mechanical behaviour of sycamore maple (*Acer pseudoplatanus* L.). Eur J Wood Wood Prod 71(1):91–99. https://link.springer.com/article/10.1007/s00107-012-0641-8

Sutton MA, Orteu JJ, Schreier H (2009) Image correlation for shape, motion and deformation measurements: basic concepts, theory and applications. Springer Science & Business Media.

Thomas PA (2016) Biological flora of the British Isles: Fraxinus excelsior. J Ecol 104(4):1158–1209. https://besjournals.onlinelibrary.wiley.com/doi/full/10.1111/1365-2745.12566

Tudor MP, Agnes MI, Szilard B (2011) Study of physical characteristics, mechanical and technological properties of wood species from the *Fraxinus* genus encountered in Romania compared to other main forestry species. Natural Resources and Sustainable Development, pp. 217–222. https://doi.org/10.31924/nrsd

Turnbull-Grimes C, Charlie WA, Gutkowski RM, Balogh J (2010) Bus-stop shelters: improved safety (phases 1 and 2). https://rosap.ntl.bts.gov/view/dot/18150

Von Wedel K (1964) *Untersuchungen über Eigenschaften, Verwertung und Verwendung des Ahornholzes*. Dissertation, Universität zu Göttingen.

Vacek S, Vacek Z, Kalousková I, Cukor J, Bílek L, Moser WK, Bulušek D, Podrázský V, Řeháček D (2018) Sycamore maple (*Acer pseudoplatanus* L.) stands on former agricultural land in the Sudetes–evaluation of ecological value and production potential. Dendrobiology (79):61–76. https://www.idpan.poznan.pl/pl/vol-79/79-61-76

Wagenführ R (2007) Holzatlas, 6th edn. Fachbuchverlag, Leipzig.

Yamada H, Tateyama K, Sasaki H, Naruke S, Kishimoto H, Yoshimoto M (2018) Impact resistance to ballistic ejecta of wooden buildings and a simple reinforcement method using aramid fabric. J Volcanol Geotherm Res 359:37–46. https://doi.org/10.1016/j.jvolgeores.2018.06.014

Defining perpendicular to grain compression stress: A comparison of methods and recommendations for ASTM D143

Zoe A. E. Sperduto [1]
Undergraduate Research Assistant, Department of Engineering, Swarthmore College
Swarthmore, PA 19081; Email: zoes@mit.edu

Fiona A. O'Donnell *†
Assistant Professor, Department of Engineering, Swarthmore College
Swarthmore, PA 19081; Email: fodonne1@swarthmore.edu

(Received 12 August 2026)

Abstract: The reliable characterization of structural properties is essential for safe and efficient structural design. This paper focuses on the behavior of lumber under compression load perpendicular to the grain. Emphasis is made on defining a standardized method for determining yield stress for tests performed in accordance with ASTM D143, primarily motivated by the need for well-defined material properties for finite element constitutive models. This research compared the existing standard test methods published by the European Committee for Standardization (CEN), International Standards Organization (ISO), and ASTM International by analyzing a series of tests performed in accordance with ASTM D143. A literature review showed that there is no dominant method for calculating strength of wood in compression perpendicular to the grain and that analysis methods are not always clearly described or aligned with the standard used for testing. Experimental results indicated that the various calculation methodologies produce significantly different strength properties; as such, a standardized calculation methodology should be implemented for use with ASTM D143 testing procedures. It is recommended that the methods for determining yield stress specified in EN 12512 should be applied to experimental data resulting from specimens tested in accordance with ASTM D143.

Keywords: Clear wood compression strength; Perpendicular to grain; Yield stress; ASTM D143

Introduction

Compression perpendicular to grain stress describes a fundamental mechanical behavior that is important for the analysis and design of bearings and connections for timber buildings. There are several international standards for characterizing perpendicular to grain compressive stress. However, these standards vary in specimen dimensions, load configuration, and definition of compressive stress. This is because some standards aim to characterize basic material properties, while others reflect typical uses (Leijten et al. 2010). The lack of unified approach to determining the standard compression perpendicular to grain strength makes it difficult to determine consistent strength values.

Computational modeling is rapidly advancing in the field of wood mechanics. There are currently several finite element software programs which offer different material models to simulate the elastoplastic and orthotropic behavior of wood (Crespo et al. 2020). However, the predictive capability of such models is fundamentally constrained by the accuracy of the input material properties. Reliable characterization of wood under fundamental loading scenarios is therefore critical for deriving the parameters required in finite element modeling (FEM).

There are several material models for wood that can be applied in FEM; however, most nonlinear constitutive models require, at a minimum, the specification of an elastic modulus and yield stress. For compression perpendicular to grain, the yield stress is different from the design value published in the National Design Specification for Wood Construction (NDS) which is a deflection serviceability limit (American Wood Council 2024). As such, determining the most appropriate stress value for use in FEM analyses is required.

The stress that distinguishes between elastic and plastic behavior of a material is sometimes called the yield point, proportional limit, elastic limit, or yield stress. Although each of these terms are used to describe that point at which the material transitions from elastic to plastic behavior, they often are understood with somewhat different interpretations (Christensen 2008). The proportional limit is the stress at which the stress-strain relationship becomes nonlinear. Defining the proportional limit can be challenging since the transition from linear to nonlinear deformation is gradual. The yield stress is typically

[1] Present Address: Graduate Research Assistant, Department of Civil and Environmental Engineering, Massachusetts Institute of Technology, Cambridge, MA 02139
* Corresponding author
† Society of Wood Science & Technology member

an engineering definition specified by a standard approach. In steel products, for example, the yield stress is defined by an offset method, where the yield stress is defined by drawing a line, offset by 0.2% strain, parallel to the elastic portion of the stress-strain curve (Instron 2023). The point where the line intersects the stress-strain curve is defined as the yield stress (ASTM International 2024). No existing ASTM standards specify a calculation method for defining the yield stress of wood in compression perpendicular to the grain.

The objective of this work is to provide a recommendation for defining compression perpendicular to grain yield stress for tests performed in accordance with ASTM D143, Test Methods for Small Clear Specimens of Timber (ASTM International 2022a), based primarily on a literature review and experimental program.

To this end, a literature review of North American and European standards for characterizing compression perpendicular to grain properties was performed to identify the existing methods for defining compression perpendicular to grain stress. A review of the academic research literature was also performed to evaluate current practices and how the standards are applied in practice.

Spruce-pine-fir (SPF) specimens were then tested in accordance with ASTM D143 (ASTM International 2022a). Several standard methods for defining compression perpendicular to grain stress were then applied to compare the analytical methods. Statistical results were computed and the parameters required for computational modeling of compression perpendicular to grain behavior are presented. Recommendations for automating the calculation of compression yield stress with tests performed in accordance with ASTM D143 are provided.

Background

Organizations such as the American Society of Testing and Materials (ASTM), the International Organization for Standardization (ISO), and the European Committee for Standardization (CEN) maintain standard procedures for defining wood properties. There are currently two general philosophies for mechanical property testing: tests can be performed with small, clear, wood samples or structural scale specimens. Clear wood properties are valuable for determining material properties without the effects of defects, whereas structural scale specimens are commonly used for defining structural design values (Arriaga et al. 2023).

ASTM D143

In North America, ASTM International Committee D07 on Wood has jurisdiction over several standards which provide fundamental test methods for characterizing wood properties and establishing structural grades and design values. The scope of each standard is summarized in Table 1. Historically, reference design values for visually graded dimension lumber were developed from small clear specimens of timber. Experimental testing was performed in accordance with ASTM D143 (ASTM International 2022a), and allowable stress and modulus of elasticity values were determined using the procedures of ASTM D245, Practice for Establishing Structural Grades and Related Allowable Properties for Visually Graded Lumber (ASTM International 2022b), and ASTM D2555, Standard Practice for Establishing Clear Wood Strength Values (ASTM International 2006). With the introduction of mechanical testing equipment capable of rapidly testing full-size structural members, it is now standard practice for allowable stress and modulus of elasticity values to be derived from tests of full-size structural members conducted in accordance with ASTM D198, Test Methods of Static Tests of Lumber in Structural Sizes (ASTM International 2022c). The transition from clear wood to structural scale specimens was implemented in the North American In-Grade Test Program.

While many of the reference design values are obtained through structural scale specimens in accordance with the methods of ASTM D198 (ASTM International 2022c) and ASTM D1990, Practice for Establishing Allowable Properties for Visually-Graded Dimension Lumber from In-Grade Tests of Full-Size Specimens (ASTM International 2025a), allowable stress values for compression perpendicular to grain continue to be calculated from small, clear wood, specimens using the procedures of ASTM D143 (ASTM International 2022a), ASTM D245 (ASTM International 2022b), and ASTM D2555 (ASTM International 2006).

ASTM D143 specifies that a 50 mm by 50 mm by 150 mm (2 in. by 2 in. by 6 in.) specimen be loaded through a 50 mm (2 in.) wide metal bearing plate placed over the central third of the specimen surface. The metal bearing plate is loaded in compression through a spherical bearing, with the specimen placed so that load is applied through the bearing plate to a radial surface, at a rate of deflection of 0.305 mm (0.012 in.) per minute until a 2.5 mm (0.1 in.) compression deformation is achieved. Compression deformation is measured between the loading surfaces (ASTM International 2022a). This testing procedure was originally developed to represent a 50 mm (2 in.) wide wood joist resting on a wall or foundation (Pellicane et al. 1994).

ASTM D245 states that the stress at the proportional limit in compression perpendicular to grain and stress in compression

Table 1. Summary of ASTM standards for wood property characterization.

ASTM Standard	Summary of standard scope
ASTM D143 – Standard Test Methods for Small Clear Specimens of Timber (ASTM International 2022a)	Provides standard test methodology for clear wood, small-scale mechanical tests.
ASTM D198 – Standard Test Methods of Static Tests of Lumber in Structural Sizes (ASTM International 2022c)	Provides standard test methodology for structural-scale mechanical tests.
ASTM D245 – Standard Practice for Establishing Structural Grades and Related Allowable Properties for Visually Graded Lumber (ASTM International 2022b)	Provides provisions for assigning reference design values for some species and grades of visually graded dimension lumber.
ASTM D1990 – Standard Practice for Establishing Allowable Properties for Visually-Graded Dimension Lumber from In-Grade Tests of Full-Size Specimens (ASTM International 2025a)	Evolved from ASTM D245; provides provisions for assigning reference design values for most species and grades of visually graded dimension lumber.
ASTM D2555 – Standard Practice for Establishing Clear Wood Strength Values (ASTM International 2006)	Referenced in ASTM D245; used to adjust strength properties of clear wood specimens to obtain reference design values applicable to normal service conditions.

perpendicular to grain at 1 mm (0.04 in.) deformation shall be obtained from ASTM D2555 (ASTM International 2006; ASTM International 2022b). The 1 mm deformation stress represents a serviceability displacement limit state, rather than a strength limit state.

In the 1977 and earlier editions of the NDS, reference design values for compression perpendicular to grain were based on proportional limit and adjusted for load duration (American Wood Council 2024). This approach was revised when ASTM D245 reclassified compression perpendicular to grain as a serviceability limit state, reframing the property as a measure of bearing deformation rather than a stress criterion (ASTM International 2022b). Since 1982, reference design values for compression perpendicular to grain have been established at a uniform deformation limit of 1 mm under a steel plate on wood bearing condition and are no longer subject to load duration adjustment (American Wood Council 2024).

Compression perpendicular to grain behavior of softwood lumber exhibits a linear-elastic initial response before yielding and experiencing an approximately linear response with a reduced modulus with considerable plastic deformation. Compressive loading perpendicular to the grain can lead to a high degree of densification, particularly in the radial direction (Arriaga et al. 2023). Identifying the proportional limit of the linear-elastic region can be difficult because the transition from linear to nonlinear is gradual. ASTM D2555 does not specify a method for identifying the proportional limit (ASTM International 2006).

Neither ASTM D245 nor ASTM D2555 provide provisions for determining compression yield stress (ASTM International 2006; ASTM International 2022b). As such, it is assumed that yield stress should be defined visually on the stress-strain curve as the end of the linear-elastic regime.

ISO 13061-5

The International Organization for Standardization (ISO) is an international federation of national standards bodies. ISO Technical Committee 218 *Timber* has jurisdiction over ISO 13061-5, *Physical and mechanical properties of wood—Test methods for small clear wood specimens Part 5: Determination of strength in compression perpendicular to grain* (International Organization for Standardization 2020). This standard has been utilized in many countries around the world including Australia, New Zealand, and some Asian countries. It is also assumed in many European countries since the European Committee for Standardization (CEN) does not currently provide guidance for testing small clear wood specimens (Arriaga et al. 2023).

ISO 13061-5 provides both test procedures and analysis methods for compression perpendicular to grain properties. The clear wood specimen height, H, should be 20 to 50 mm (0.8 to 2 in.), length, L, should be 1.5 to 3 times the height, and the width, W, should be greater than or equal to half of the height. Loading should be applied radially, tangentially, or at an angle of 45 to the growth rings, at a constant rate such that yield is reached within 1 to 5 min (60 to 300 s), and specimens are loaded until 5% deformation. With regards to sensing, it states, "When using a testing machine without an accurate recording device, a displacement measuring device shall be used to determine the deformation of the height" (International Organization for Standardization 2020). ISO 13061-5 specifies that the proportional limit in compression perpendicular to the grain should be defined as the ordinate of the point where the tangent of the angle formed by the load axis with the tangent to the load-deformation curve is 50% greater than its value in the linear portion of the diagram. The proportional limit stress is then the load at the proportional limit divided by the bearing area (International Organization for Standardization 2020).

EN 408

The European standard, EN 408, *Timber structures—Structural timber and glued laminated timber—Determination of some physical and mechanical properties*, does not limit samples to clear wood; instead, it applies broadly to solid wood, glued laminated timber, and other wood-based products (British Standards Institution 2012). For compression perpendicular to grain, EN 408 provides both testing and calculation guidelines for the compression stress and modulus of elasticity. For testing structural timber, EN 408 calls for a 45 mm by 90 mm by 70 mm (1.8 in. by 3.5 in. by 2.8 in.) specimen to be loaded over the entire length of the sample through spherically seated loading heads; the load rate should be determined so the maximum load is reached within 5 ± 2 min (300 ± 120 s). EN 408 also specifies that displacement should be measured by two extensometers centered on the specimen on opposite sides with a gauge length approximately equaling 60% of the height of the sample (British Standards Institution 2012).

The compression stress is calculated using an iterative method in which the maximum compressive force, $F_{C,90,max,est}$, is estimated visually, and the modulus of elasticity, *E,* is calculated by

$$E = \frac{(F_{40} - F_{10})h_0}{(w_{40} - w_{10})bl} \quad [1]$$

where F_{40} and F_{10} correspond to the 40% and 10% of the estimated maximum compressive force, $F_{C,90,max,est}$, and w_{40} and w_{10} are the deformations corresponding to F_{40} and F_{10}.The gauge length, specimen width, and specimen length are h_0, b, and l, respectively. A line is then drawn with a slope of E and originating at a force of 0 and deformation equal to 1% of h_0. If the point of intersection of this line and the experimental data is within 5% of $F_{C,90,max,est}$, then that load may be used to determine the compressive stress by:

$$f = \frac{F_{c,90,max}}{bl}. \quad [2]$$

Otherwise, the procedure is repeated until a value of $F_{C,90,max}$ within the 5% tolerance limit is obtained. The subscript *max* utilized in $F_{C,90,max}$ and $F_{C,90,max,est}$ is not referring to the maximum load reached during a test but rather the load at the maximum compressive stress, as defined by EN 408. Notably, EN 408 defines *compression* stress in perpendicular to grain and does not define a *yield* stress (British Standards Institution 2012).

EN 12512

The European standard, EN 12512, *Timber Structures – Test Methods – Cyclic testing of joints made with mechanical fasteners*, is not intended for defining fundamental material properties of wood; instead, it specifies a test method for determining "the ductility, impairment of strength, and energy dissipation properties of joints made with mechanical fasteners under cyclic loading" (British Standards Institution 2005). Although the specified test methods do not apply to this study, the standard provides a well-defined approach to defining yield load that could be applied to defining the compression perpendicular to grain yield stress. In Method A of EN 12512 (referred to hereafter as "12512a"), which is applied when the load-slip curve presents two well-defined linear sections, the yield load is determined by the intersection between these two lines. This can be modified to be applied to a stress-strain curve. EN 12512 also provides Method B (referred to hereafter as "12512b") for defining the yield load when the yield-slip curve does not have two well-defined linear sections. In this method, the yield values are determined by the intersection of two lines. The first line is drawn through the point on the load-slip curve corresponding to $0.1F_{max}$ and $0.4F_{max}$. The second line is the tangent having an inclination of 1/6 of the first line (British Standards Institution 2005).

Comparison of Test Procedures

The three primary test methodologies considered in this paper for compression perpendicular to grain are ASTM D143 (ASTM International 2022a), EN 408, and ISO 13061-5 (British Standards Institution 2012; International Organization for Standardization 2020). Both ASTM D143 and ISO 13061-5 pertain to small, clear wood specimens, while EN 408 permits larger scale specimens. In ASTM D143, the load is transmitted through a metallic loading block that does not cover the entire area of the specimen, leading to higher compression perpendicular to grain values than in cases in which the load is applied over the full area of the specimen (Kunesh 1968; Bodig 1969; Pellicane et al. 1994, as cited in Basta et al. 2011). In contrast, both EN 408 and ISO 13061-5 transfer compression load through the full area of the cross-section. The ASTM loading procedure is intended to reflect typical loading conditions, such as a beam fully supported on a bearing wall or foundation, and loaded by a square stud (Bodig and Jayne 1982, as cited by Leijten et al. 2012). The EN 408 method aims to define physical material properties, rather than properties related to typical applications. A summary of the test methodologies is provided in Table 2. While EN 12512 is considered in this study as a calculation method, the specific testing procedure

Table 2. Comparison of test methodologies.

Standard	Specimen dimensions (mm)	Bearing plate location	Displacement measurement	Test rate
ASTM D143 (ASTM International 2022a)	50 × 50 × 150	Local center through radial surface	Measured across entire length of specimen	0.305 mm/min up to 2.5 mm displacement
EN 408 (British Standards Institution 2012)	45 × 90 × 70	Full area	Two extensometers on opposite sides of sample; Gauge length of approx. 0.6h and shall be located centrally in the test piece height	Compressive stress reached in 5 min ± 2 min
ISO 13061-5 (International Organization for Standardization 2020)	H = 20 to 50; L = 1.5H to 3H; W 0.5H	Full area	Not specified	Proportional limit is reached in 1–5 min

is not discussed here, as it is not intended for material property characterization (British Standards Institution 2005).

Leijten et al. (2012) provide an assessment and comparison of testing procedures for determining the compressive stress of wood in compression perpendicular to the grain and demonstrate a model for making testing results compatible when using the various procedures (Leijten et al. 2012). However, they consider ASTM D143 to define the compressive stress of wood in compression perpendicular to the grain at 1 mm which represents the serviceability limit specified by ASTM D245 (ASTM International 2022a; ASTM International 2022b). The study presented in this manuscript builds on the work of Leijten et al. (2012) by suggesting standardized analysis methodology for calculating yield stress, rather than a serviceability limit, for tests performed in accordance with ASTM D143.

Methodology

Literature review

A literature review was conducted using the Web of Science search engine to identify publications that performed compression perpendicular to grain tests and defined the compressive stress of wood (Web of Science Master Journal List - WoS MJL by Clarivate). The key terms "compression" AND ("perpendicular-to" OR "perpendicular to") AND ("wood" OR "lumber" OR "clear wood") OR "strength" were applied to titles, abstracts, and keywords for papers. Results were filtered to include only papers published between 2010 and 2025 and limited to Web of Science Categories relevant to this research. This yielded 180 papers; of these, 169 were obtained in English through public or institutional access and then reviewed to determine relevance with respect to this investigation.

Experimental testing

Experimental testing was performed in accordance with ASTM D143: Test Methods for Small Clear Specimens of Timber. ASTM D143 is the standard procedure used in North America for determining wood compression properties but does not provide specific guidance for defining compression perpendicular to grain yield stress (ASTM International 2022a).

Materials

Twenty-one 3048 mm (10 ft.)-long nominal 2×6 SPF boards with a 2100fb 1.8E rating were sourced from Spokane, WA. Samples taken from four different boards were sent to external labs for species identification. The results indicated that the samples were in the yellow pine, or western hard pine, group. Two of the samples were identified as radiata pine (*Pinus radiata*) and two of the samples were identified as likely lodgepole pine (*Pinus contorta*).

ASTM D143 specifies compression perpendicular to grain samples to be rectangular prisms with dimensions of 50 mm by 50 mm by 150 mm (2 in. by 2 in. by 6 in.). Due to constraints in the cross-sectional dimensions of the source lumber, samples were manufactured to 45 mm by 45 mm by 150 mm (1.75 in. by 1.75 in. by 6 in.) (ASTM International 2022a) (Figure 1A). Samples of required dimensions could not be obtained from 3 out of the 21 boards due to the presence of defects in these boards. As such, 18 specimens were manufactured. After manufacturing, samples were moisture conditioned in a steady-state conditioning chamber set to 20C and 65% relative humidity to achieve 12% ± 3% moisture content.

The specimens were weighed immediately prior to testing. After testing, the specimens were placed in an oven at 105°C for 24 h. Specimens were then weighed and placed back into the oven until the change in oven-dry weight was less than 1% over 24 h. The moisture content was determined by ASTM D4442, Test Methods for Direct Moisture Content Measurement of Wood and Wood-Based Materials (ASTM International 2025b): MC (%) = 100 ($W_W - W_{OD}$) / W_{OD}, where W_{OD} is the oven-dry weight and W_W is the pre-test weight.

Testing procedure

Specimen depth, width, and length were measured at three different points on each sample. The average values were used

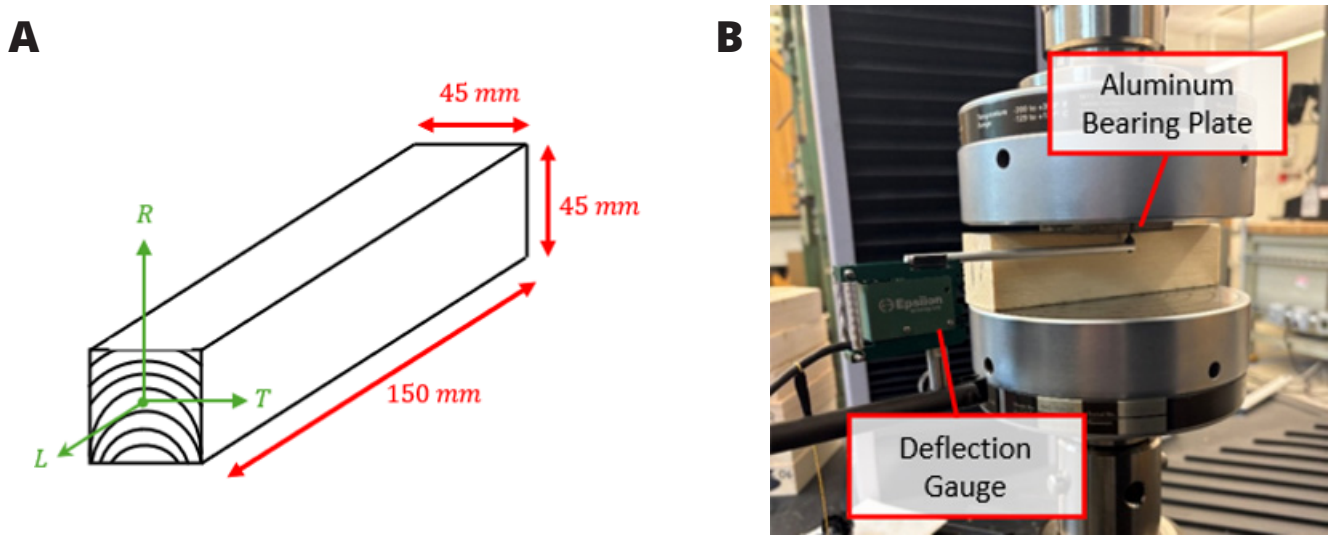


Figure 1. Experimental test assembly for compression perpendicular to grain.(A) Specimen geometry; (B) Test set up.

in stress and strain calculations. Specimens were tested in a 66-kip Electromechanical Universal Testing Machine (MTS Systems, MTS Criterion C45.305). Compression was loaded through rigid platens to the radial surface. A 50 mm (2 in.) wide aluminum bearing plate was placed between the platen and upper surface of the specimen at equal distances from the end of the specimen. In accordance with ASTM D143, deflection was measured between the loading surfaces; a deflection gauge (Epsilon Technology Corp., 3540-025T-ST; measuring range: 6.4 mm (0.25 in.); accuracy: ASTM E2309 Class A, ISO 9513 Class 1) was placed beneath the aluminum plate. Compression load was applied at a constant crosshead rate of 0.305 mm/min (0.012 in./min) until a crosshead displacement of 2.5 mm (0.1 in.) compression (ASTM International 2022a) (Figure 1B).

Data processing and calculation methods

Load, displacement, and deflection gauge data were recorded throughout each test. Stress and strain were determined by $\sigma = F/A$ and $\epsilon = \Delta L/L$, where F is the force measured by the crosshead, A is the measured cross-section of the loaded area of the specimen (i.e., the bearing plate width multiplied by the specimen width), ΔL is the deformation measured by the deflection gauge, and L_i is the initial depth of the specimen.

Yield stress in compression perpendicular to the grain was calculated using four standardized methods for calculating compressive strengths: visual determination, the point on the stress-strain curve where the angle between the stress-strain curve and y-axis increases by 50% (ISO 13061-5), the intersection point of the 1% offset of the linear elastic region (EN 408), and the intersection between the linear elastic region and a line fit to the plastic region (EN 12512) (British Standards Institution 2005; British Standards Institution 2012; International Organization for Standardization 2020). While ISO 13061-5 defines the stress at the proportional limit and EN 408 defines the compressive stress, this study applies the methodology as a yield stress calculation.

Modulus of elasticity calculation

To facilitate a simplified and automated analysis procedure, the slope of the linear elastic region was defined using consistent load intervals across all samples. Visual inspection indicated that the linear region generally occurred at loads between 30% and 50% of the maximum load. As such, the modulus of elasticity was defined as:

$$MOE_{\perp} = \frac{0.5f_u - 0.3_{fu}}{0.5\epsilon - 0.3\epsilon} \quad [3]$$

Yield stress calculation

Visual method

As implied by the name, the visual method requires that the user define the yield stress visually on the stress-strain curve as the upper limit of the linear-elastic regime. After selecting a point, the algorithm selects the closest recorded data point and defines the corresponding stress as the yield stress.

ISO 13061-5

ISO 13061-5 defines the load corresponding to the proportional limit "as the ordinate of the point where the tangent of the angle formed by the load axis with the tangent to the load-deformation curve is 50% greater than its value in the linear portion of the diagram." The linear portion corresponds to the

elastic region; therefore, its slope is taken as the perpendicular modulus of elasticity, $MOE_{\perp}$ The angle of the elastic region relative to the load axis was defined as:

$$\theta_1 = \tan^{-1}\left(\frac{1}{MOE_{\perp}}\right) \quad [4]$$

In accordance with ISO 13061-5, the angle of the tangent line at which the compressive strength is defined was defined as: $\tan(\theta_2) = 1.5\ \tan(\theta_1)$(Figure 2) (International Organization for Standardization 2020).

EN 408

EN 408 defines the compression strength perpendicular to the grain using an iterative process. First, an initial estimate of the yield stress on the stress-strain curve, $F_{C,90,max}$ is selected. The algorithm then determines $0.1F_{C,90,max}$ and $0.4\ F_{C,90,max}$, identifies where these values intersect the stress-strain curve, and calculates the modulus of elasticity as:

$$MOE_{\perp} = \frac{0.1\ \sigma - 0.4\sigma}{0.1\epsilon - 0.4\epsilon} \quad [5]$$

A line with the slope $MOE_{\perp}$ is then drawn offset on the x-axis by the strain corresponding to a deformation of $0.01h$, where h is the original height of the test specimen. The intersection of this offset line and the stress-strain curve is calculated to determine $F_{C,90,max,est}$ (Figure 3). If $F_{C,90,max,est}$ is within 5% of $F_{C,90,max}$, then $F_{C,90,max}$ may be used as the compressive strength. The procedure is repeated until a value within the tolerance is found (British Standards Institution 2012).

EN 12512

EN 12512a defines the yield load for load-displacement curves exhibiting two well-defined linear regions as the intersection point between two lines drawn parallel to these respective regions. To simplify and automate analysis, the slopes of the lines were defined by consistent regions across all samples. Visual inspection indicated that the first linear region was generally observed at loads between 30% and 50% of the maximum load, while the second linear region typically occurred between 90% and 99% of the maximum load. As such, the slopes were defined by:

$$m_1 = \frac{0.5F_u - 0.3_{F_u}}{\delta_{0.5} - \delta_{0.3}} \quad [6]$$

$$m_2 = \frac{0.99F_u - 0.9F_u}{\delta_{0.99} - \delta_{0.9}} \quad [7]$$

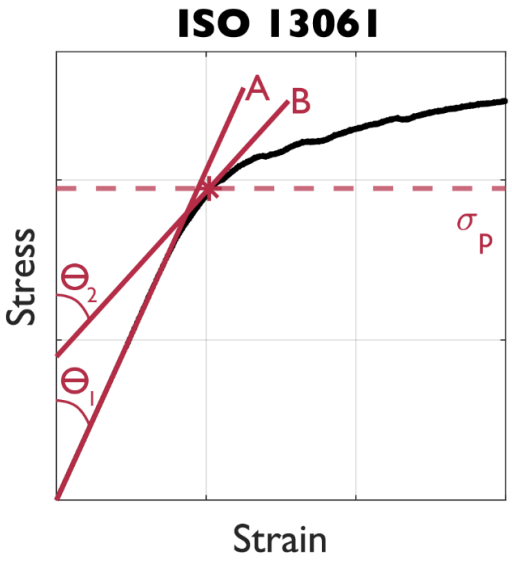


Figure 2. A depiction of the method for calculating the compressive perpendicular to grain strength at the proportional limit outlined in ISO 13061.

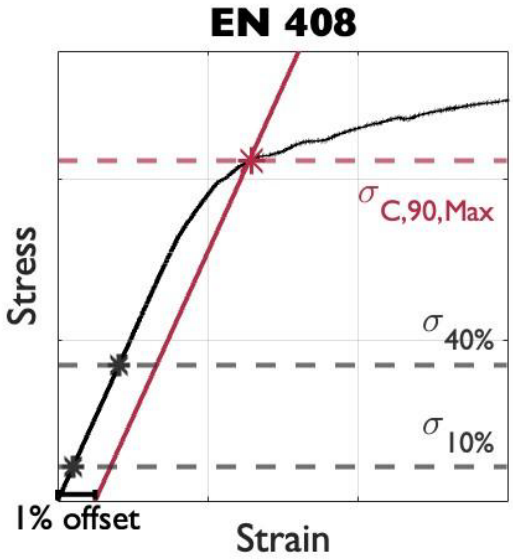


Figure 3. A depiction of the method for calculating compression stress perpendicular to the grain outlined in EN 408.

where F_u is the maximum load for each sample and δ represents the corresponding displacement (British Standards Institution 2005).

EN 12512b provides a method for defining the yield load for load-displacement curves that do not exhibit two well-defined linear parts. The yield load is determined by the intersection of two lines. The first line is drawn through the points of the load-displacement curve corresponding to $0.1F_u$ and $0.4F_u$ The second line has a slope equal to 1/6 of the slope of the first line and is tangent to the load-displacement curve (British

Standards Institution 2005). Refer to Figure 4 for visualizations of both EN 12512a and EN 12512b.

Statistical Analysis

The average, standard deviation, and coefficient of variation of the yield stresses were calculated for each of the four methods. The processed data was used for all calculation methods. A one-way analysis of variance (ANOVA) test was performed ($\alpha = 0.05$ significance level) to determine whether there were significant differences between the calculated yield stress values from each of the four methods utilized. Resulting yield stresses were plotted on a histogram, and a Weibull probability-density function was fitted to the data to assess spread.

Results

Literature review

Fifty-four papers were deemed relevant to the literature review, meaning they tested small wood specimens in compression perpendicular to the grain and calculated a compressive stress value (Ido et al. 2010; Widmann et al. 2012; Barnes et al. 2013; Moya et al. 2013; Pleschberger et al. 2013; Skarvelis and Mantanis 2013; Ang et al. 2014; Jiang et al. 2014; Yorur et al. 2014; Crafford and Wessels 2016; Hong et al. 2016; Kotlarewski et al. 2016; Milch et al. 2016; Tippner et al. 2016; Bahtiar et al. 2017; Kiaei and Abadian 2018; Lukowsky et al. 2018; Miyamoto et al. 2018; Chen et al. 2019; M Hussein et al. 2019; MM Hussein et al. 2019; Kijidani et al. 2019; Pang et al. 2019; Irby et al. 2020; Kovryga et al. 2020; Müller et al. 2020; Roszyk et al. 2020; Uzcategui et al. 2020; Verbist et al. 2020; Muthumala et al. 2021; Sharma and Kelkar 2021; Shmulsky et al. 2021; Bahtiar et al. 2022; Cheng et al. 2022; Cherry et al. 2022; Collins and Fink 2022; Kurt and Korkmaz 2022; Piernik et al. 2022; Smídová et al. 2022; Wu et al. 2022; Yu et al. 2022; Zhang et al. 2022; Feujofack K and Loss 2023; Gupta et al. 2023; Shukla and Viswanath 2023; Fruehwald-Koenig and Heister 2024; Marasigan et al. 2024; Mendes et al. 2024; Neimsuwan et al. 2024; Rosner et al. 2024; Toba et al. 2024; Gambarelli et al. 2025; Ike et al. 2025; Naissi et al. 2025; Saltik 2025). Papers focused on composite materials or engineered wood products were excluded, as the goal of this review was to characterize common testing and analysis methodologies for clear wood. Similarly, papers reporting finite element simulations rather than experimental testing were excluded. The following results summarize the testing and strength calculation methodologies employed across the 54 relevant papers. Many studies include multiple measurements of compressive strength (e.g., reporting the stress at 5% strain and the stress at the proportional limit), and these are considered as independent in the summaries below. As such, the total number of papers reported in Table 3 and the following paragraphs may not sum to the expected total number of papers.

Geographically, the papers spanned six continents: 3 were written by primary authors based in Africa, 23 in Asia, 3 in Australia, 18 in Europe, 5 in North America, and 2 in South America.

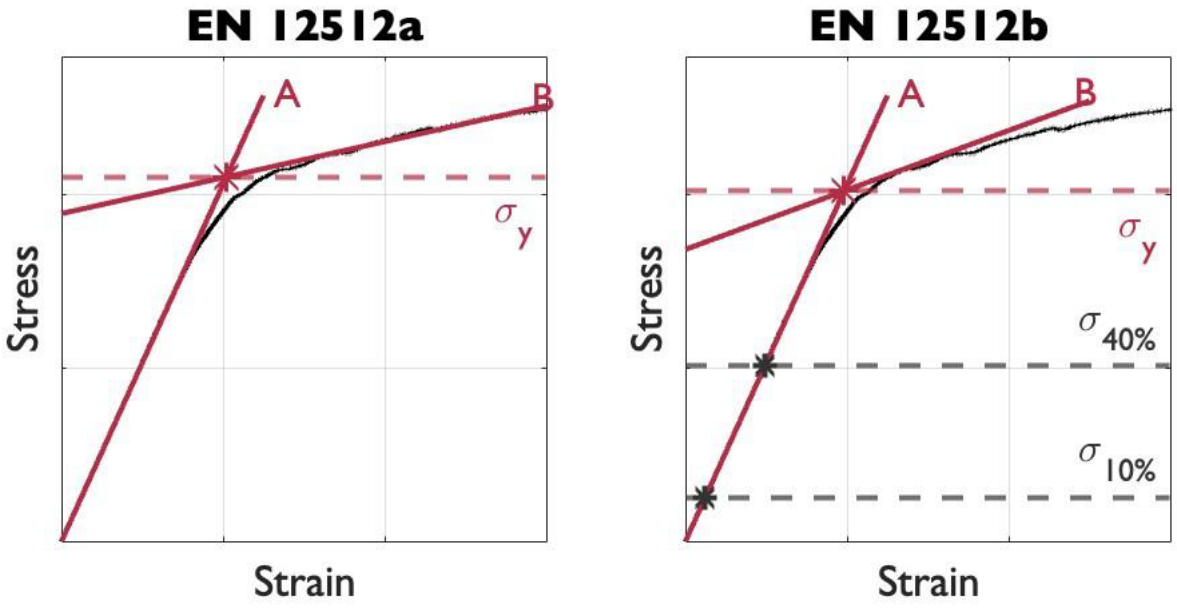


Figure 4. A depiction of the methods outlined for calculating the yield load described in EN 12512.

Due to variations in calculation and testing methods, the standard used for material testing was considered separately from the standard or method used for compressive strength analysis. Table 3 shows the testing standards used in the papers reviewed: 19 papers cite ASTM D143, 6 cite EN 408, and 4 cite ISO 13061-5. Twelve additional testing standards are cited for material testing. Two papers do not cite any standards for material testing.

Of the 54 papers in the literature review, 34 specified how the compressive strength was determined and 20 papers did not indicate any calculation procedure. Of the 34 papers discussing analysis methodology, 14 papers cited a standard used for analysis (AS/NZS 4063 – 2, ASTM D143 – 1, BS 373 – 1, DIN 52192 – 1, EN 408 – 5, ISO 13061-17 – 2, ISO 13910 – 1, ISO 3132 – 1, JIS Z2101 – 1), and 20 papers specified a method for analysis but did not link that to a standard (British Standards Institution 1957; International Organization for Standardization 1975; German Institute for Standardization 1979a; Japan Standards Association 1994; Standards Australia and Standards New Zealand 2010; British Standards Institution 2012; International Organization for Standardization 2014; International Organization for Standardization 2017; ASTM International 2022a). The discussion of the analysis methods used in the literature will focus on papers utilizing ASTM D143, EN 408, and ISO 13061-5 for test methodology (British Standards Institution 2012; International Organization for Standardization 2020; ASTM International 2022a). Table 4 provides an overview of the analysis methods utilized by those papers.

Nineteen papers utilized ASTM D143 for material testing (Table 4) (ASTM International 2022a). This standard does not specify a method for determining the stress of wood in compression perpendicular to the grain. Only nine of these papers specified the methodology used to determine the compressive stress of the wood. Two papers calculated the stress as the proportional limit on the stress-strain curve: one of these papers cited ISO

Table 3. Testing standards for compression perpendicular to the grain cited in the reviewed literature.

Testing standard	Number of papers	Standard's region of development	Country of first author
ASTM D143 (ASTM International 2022a)	19	USA	Australia, Canada, Egypt, Germany, Indonesia, Iran, Korea, Philippines, Portugal, Thailand, United Kingdom, United States, Uruguay
EN 408 (British Standards Institution 2012)	6	Europe	Brazil, Czech Republic, Finland, Germany, Spain
ISO 13061-5 (International Organization for Standardization 2020)	4	Global	China, Japan, Poland
BS 373 (British Standards Institution 1957)	4	UK	Czech Republic, Malaysia, Sri Lanka
DIN 52192 (German Institute for Standardization 1979a)	4	Germany	Austria, Germany, Switzerland
IS: 1708 (Indian Standards Institution 1986)	3	India	India
GB/T 1943–2009 (National Standards of People's Republic of China 2009a)	2	China	China
ISO 13061-17 (International Organization for Standardization 2017)	2	Global	Turkey
JIS Z2101 (Japan Standards Association (JSA) 1994)	2	Japan	Japan
AS/NZS 4063 (Standards Australia and Standards New Zealand 2010)	2	Australia/New Zealand	Australia, South Africa
GB/T 1939-2009 (National Standards of People's Republic of China 2009b)	1	China	China
DIN 52185 (German Institute for Standardization 1979b)	1	Germany	Germany
ISO 3132[1] (International Organization for Standardization 1975)	1	Global	Greece
TS 2473 (Turkish Standards Institution 1976)	1	Turkey	Turkey
Unspecified Chinese national standard	1	China	China
No standard specified	2	N/A	Austria, China

[1] ISO 3132 has been replaced by ISO 13061.

Table 4. Analysis methodologies utilized by papers citing ASTM D143, EN 408, and ISO 13061-5 as the standard test methodology.

Testing standard	Analysis method	Analysis standard cited	Number of papers
ASTM D143	None specified	None	10
	Fixed displacement	AS/NZS 4063	1
		ASTM D143	1
		ISO 3132	1
		None	2
	Proportional limit	ISO 3132	1
		None	1
	Maximum displacement	None	3
	Linear offset	EN 408	1
	Novel method	None	1
EN 408	None specified	None	2
	Linear offset	EN 408	4
ISO 13061-5	None specified	None	1
	Proportional limit	None	2
	Fixed displacement	None	1
	Novel method	None	1

3132 for this calculation, and the other did not cite an analysis standard (International Organization for Standardization 1975). Three papers calculated the stress as the maximum force over the area of the specimen; none of these papers cited an analysis standard. One paper calculated the stress using a linear offset method and cited EN 408 as the analysis standard (British Standards Institution 2012). One paper utilized a novel method to calculate the stress. Five papers calculated the stress at a fixed displacement: one did so according to AS/NZS 4063 at 0.1 times the height of the specimen, one did so according to ISO 3132 at 2.5 mm deflection, and one did so at 1 mm deflection, citing ASTM D143, despite this not being specified in the standard. The remaining two papers did not cite an analysis standard, but one calculated the stress at 1 mm and the other at 2.5 mm (International Organization for Standardization 1975; Standards Australia and Standards New Zealand 2010; ASTM International 2022a). The 2.5 mm displacement corresponds with the end of the compression perpendicular to grain test in specified ASTM D143 and the 1 mm displacement corresponds with serviceability stress definitions provided in ASTM D245, although the connection between the analysis methodology and the standards was not linked in these papers (ASTM International 2022a; ASTM International 2022b). Of the 19 papers utilizing ASTM D143 for material testing, 16 of those papers referred to the calculated strength property as the "strength," "compressive strength," or "compressive strength perpendicular to grain," without specifying whether this is a yield strength, ultimate strength, maximum strength, etc.

Seven papers cited EN 408 as the testing and/or the analysis standard (Table 4) (British Standards Institution 2012). One paper cited ASTM D143 for testing and EN 408 for strength analysis and four papers cited EN 408 for both testing and analysis (British Standards Institution 2012; ASTM International 2022a). Two papers cited EN 408 only for testing and did not specifically discuss a method of analysis; however, this does not necessarily mean a different analysis method was used (British Standards Institution 2012). All seven papers referred to the calculated strength property using generic terms ("strength," "compressive strength," or "compressive strength perpendicular to grain").

Four papers cited ISO 13061-5 as the standard used for material testing (Table 4) (International Organization for Standardization 2020). No papers explicitly stated that ISO 13061-5 was used for analysis as well, although the standard does provide a procedure for calculating the stress at the proportional limit. Of these four papers, two papers used the proportional limit as the compressive strength, one paper determined the compressive strength using a novel method similar to EN 12512 and a fixed displacement at 5% strain, and one paper did not specify an analysis method. Of the four papers utilizing ISO 13061-5 for material testing, three of those papers referred to the calculated strength property using generic terms (British Standards Institution 2005; International Organization for Standardization 2020). Two additional papers utilized ISO 13061-17 for material testing in compression perpendicular to

the grain, calculating the strength as the maximum load over the cross-sectional area, though this standard was developed for compression *parallel* to the grain (International Organization for Standardization 2017).

The literature review demonstrates that several different methods are being used to determine the compressive strength of wood in compression perpendicular to the grain, and no single method seems to be dominating the current literature. Even within a set of papers utilizing the same material testing standard, multiple methods will be used to calculate the compressive strength that may yield drastically different values. The literature review also highlights the need for consistent and clear language when referring to and defining compression strength. This is particularly important for compressive strength perpendicular to the grain, given that the published standards and literature define strength at specified deformation or strain, the proportional limit, the ultimate strength, and/or the yield strength. The high number of papers using ASTM D143 test procedures highlights the need for a standard analysis approach.

Experimental results

Processed stress-strain profiles for the 18 spruce-pine-fir samples are shown in Figure 5.

The mean compression perpendicular to grain modulus of elasticity was 374 ± 136 MPa. The coefficient of variation was 36.28%.

Table 5 contains the mean and standard deviation compressive perpendicular to grain yield stress values for the four methods utilized in addition to the coefficient of variation. The mean yield stress was lowest for the ISO 13061-5 calculation (4.926 MPa) and highest for the EN 408 calculation (6.448 MPa).

Figure 6 provides the results of a single specimen's stress-strain curve to visually represent the different yield points selected by the different methods. The ASTM deformation serviceability limit is also indicated.

Performing an analysis of variance (ANOVA) test indicates that yield stress values resulting from the different calculations

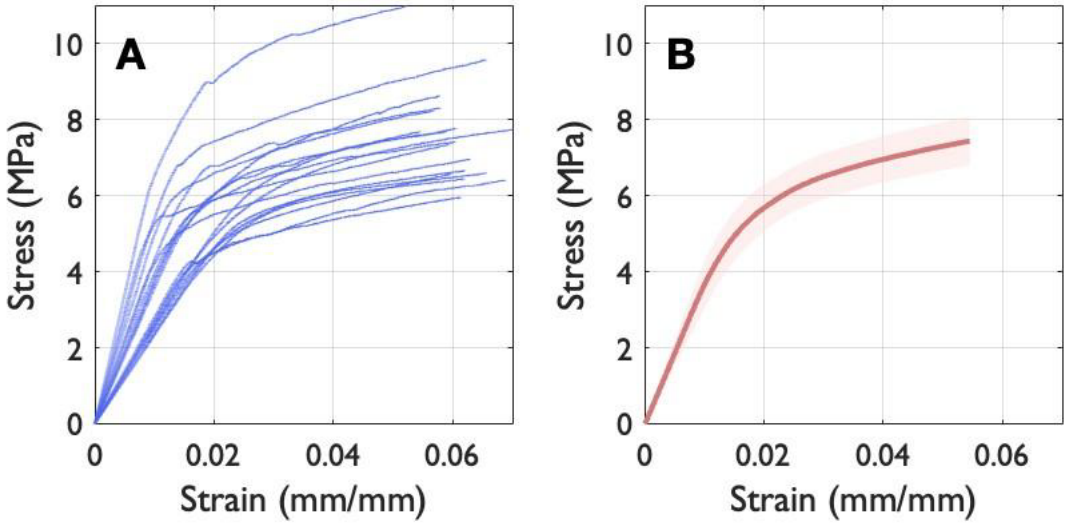


Figure 5. (A) processed stress-strain profiles; (B) mean stress-strain profile with 95% confidence interval.

Table 5. Yield stress values for the four methods tested.

Method	Mean (MPa)	Standard Dev (MPa)	Coefficient of Variation (%)	Maximum (MPa)	Minimum (MPa)
Visual	5.549	0.923	16.63	7.825	4.321
ISO 13061-5	4.926	0.682	13.845	6.180	3.943
EN 408	6.448	1.0741	16.66	9.450	4.941
EN 12512a	6.270	1.077	17.17	9.513	4.818
EN 12512b	5.759	0.930	16.14	8.204	4.396

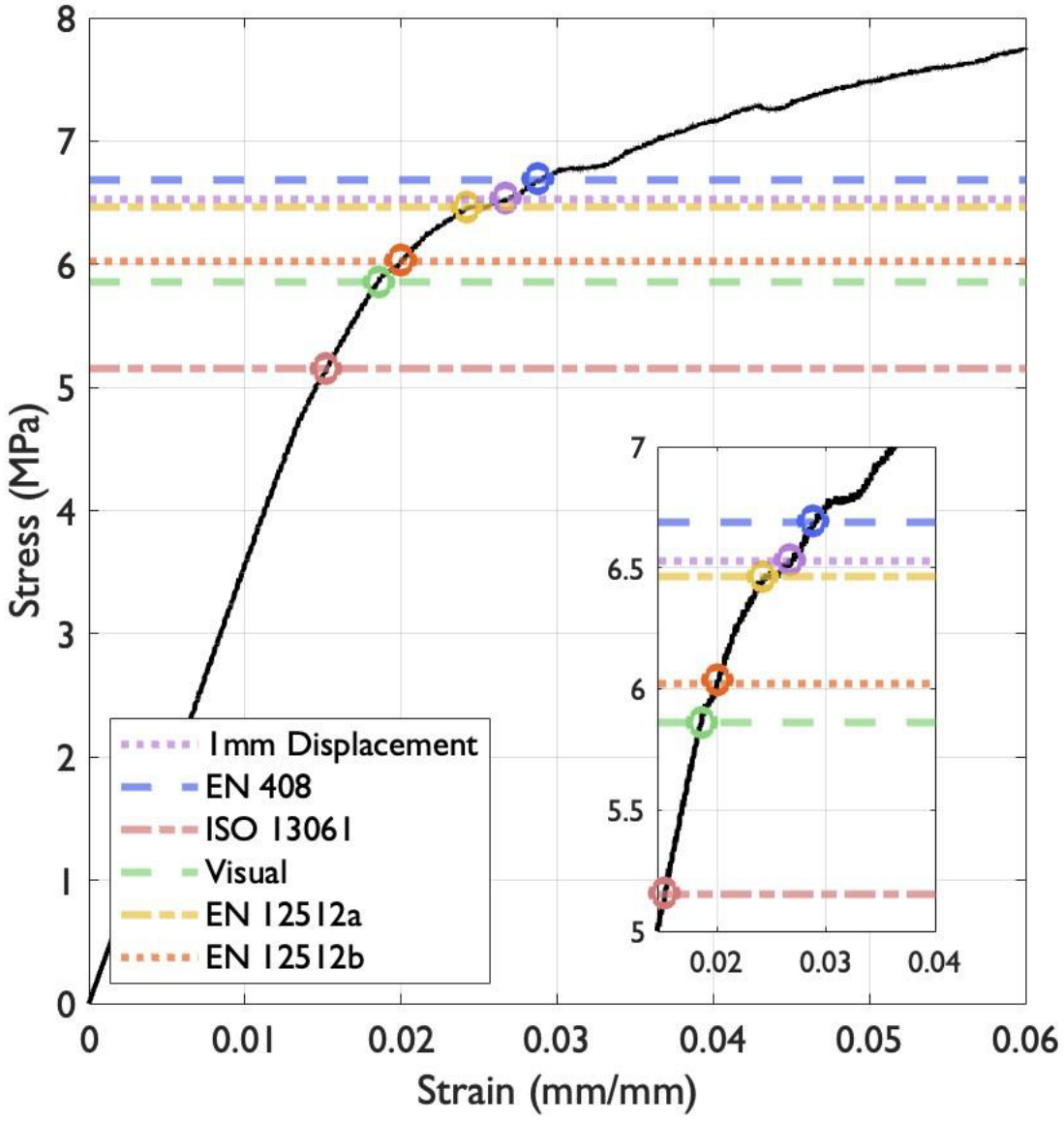


Figure 6. The stress-strain curve of Sample 01A with the resulting yield stresses from the four methods utilized.

methods are significantly different ($p < 10^{-5}$). Figure 7 shows the histogram of yield stresses for each calculation method with a two-parameter Weibull probability-density function fit to each curve. A two-parameter Weibull distribution was selected to align with procedures outlined in ASTM D5457 (ASTM International 2023).

A separate calculation of the stress corresponding to the 1 mm deflection, the ASTM serviceability limit, resulted in a mean stress of 6.295 ± 1.221 MPa (coefficient of variation = 19.39%) (Figure 8). This value most closely aligns with the mean yield stress calculated using EN 12512a (British Standards Institution 2005).

Discussion

This experimental campaign and research investigation characterized differences between international standards for defining compression strength perpendicular to the grain. The literature review showed that there is no dominant method for determining compressive stress and that there is a disconnect between testing and analysis methods. Of the 54 papers reviewed, only 34 provided explicit insight into how the compressive stress was calculated. Within sets of papers utilizing the same material testing standard, multiple methods were used to calculate compressive stress. The experimental campaign evaluated five methods for determining yield stress and found that the methods provided statistically different stress values. Thus, an

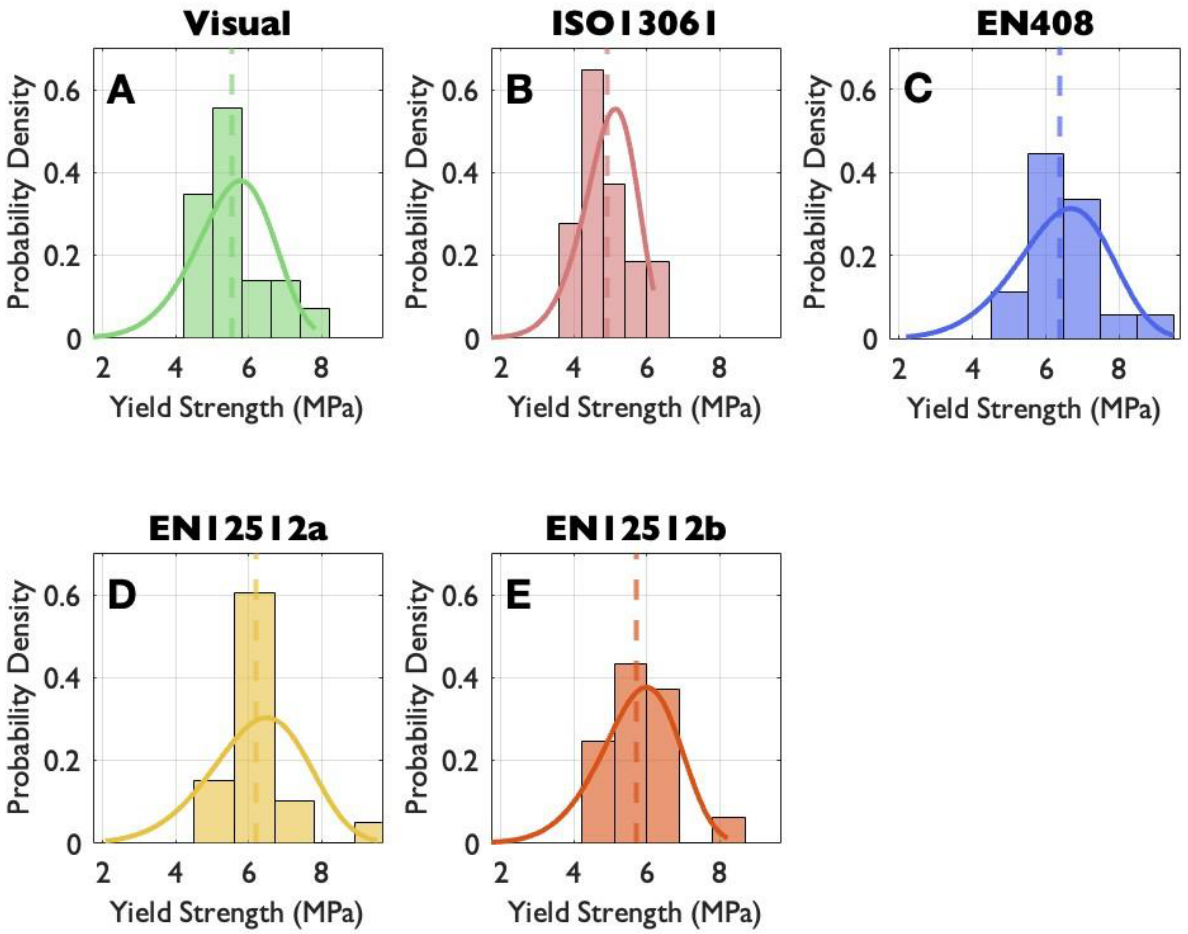


Figure 7. Histograms of the yield stress values with an overlayed Weibull probability-density function and average strength indicated by a dashed line for the (A) visual method, (B) ISO 13061-5, (C) EN 408, (D) EN 12512a, and (E) EN 12512b.

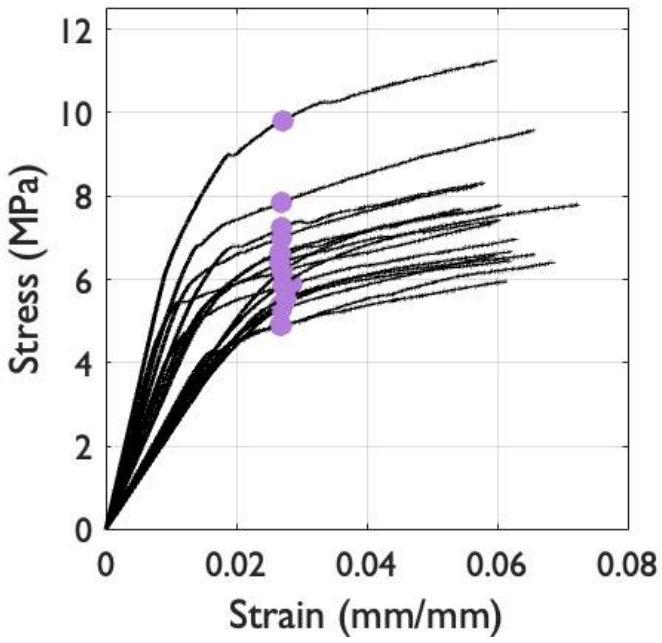


Figure 8. The stress-strain curves with the point of 1 mm deflection indicated as a purple circle.

analysis method must be standardized to allow for reproducible results, especially to be used with ASTM D143, which does not provide a calculation method for determining the yield stress in compression perpendicular to the grain (ASTM International 2022a).

The significant differences in the stress calculated by the analysis methods may reflect the different material properties that each standard was developed to determine. ISO 13061-5, which produced the lowest mean strength, determines the "proportional limit" stress (International Organization for Standardization 2020); this is consistent with the proportional limit representing the beginning of non-linear behavior on the stress-strain curve. EN 12512 determines the "yield" stress, and the two methods specified produced average stresses higher than ISO 13061-5 (British Standards Institution 2005); this is expected because the yield stress is often an engineered calculation that lies above the first instance of non-linear behavior. EN 408, which produced the highest mean stress,

determines the "compression strength." Since the standard defines the load at this strength as the "maximum load," it is expected that this method would produce the highest strength calculation (British Standards Institution 2012).

For reproducibility of analysis, comparison of results, and efficient data processing, it is advantageous for analysis methods to be automated. While the visual method enables each sample to be analyzed independently, the introduction of human engineering judgement can lead to differences in results. Similarly, EN 408 requires engineering judgement for the initial estimate of yield stress to perform the analysis. This human interaction for each sample also reduces the efficiency of data analysis, which is essential for highly heterogenous materials like wood which require large sample sizes. EN 12512, by contrast, is a fully automated procedure (British Standards Institution 2005). While it was not developed for use in compression perpendicular to grain tests, it leads to results that are within range of methods developed for this application while requiring limited human input. As such, EN 12512 provides a standardizable procedure for calculating the yield stress of clear wood perpendicular to grain for tests performed in accordance with ASTM D143.

An additional method proposed by Christensen was considered but ultimately excluded from the analysis (Christensen 2008). This method identifies the yield point as the absolute maximum of the second derivative of the stress-strain curve, corresponding to the point at which the tangent modulus changes at the greatest rate with respect to increasing strain (Christensen 2008). In practice, however, numerical differentiation of experimental data produced unreliable results. Noise in the data led to local negative slopes in the elastic region, despite a globally constant and positive slope. A similar challenge was found when applying the methods of ISO 13061-5 using numerical integration (International Organization for Standardization 2020). Smoothing approaches such as the Savitzky-Golay filter were sensitive to parameter selection, with different parameter choices leading to meaningfully different results. Because this study aimed to develop a methodology that could be applied consistently regardless of data sampling rate, this method was deemed not viable.

The methodologies in EN 12512 are recommended for adoption into the North American practice for defining yield stress (British Standards Institution 2005). It offers a fully automated, analytically efficient procedure, suitable for the large sample sizes required for heterogenous materials like wood. Specifically, EN 12512a provides the most appropriate yield stress calculation method for integration with ASTM D143. ASTM D143 ends testing after 2.5mm of deflection and, given the linear post-yield behavior of most softwood lumber, this would result in a stress-strain curve with two well-defined linear parts (ASTM International 2022a). In that case, EN 12512 specifies method a. Method b would instead be used for a longer-term loading, which is irrelevant when using ASTM D143 testing procedures (British Standards Institution 2005; ASTM International 2022a). Additionally, EN 12512b requires a calculation of the line tangent to the stress-strain curve, which can be computationally challenging and sensitive to noise and data filtering techniques. EN 12512a, thus, provides a fully automated method for determining yield stress that compliments the compression perpendicular to grain testing procedure outlined in ASTM D143.

Conclusion

The yield stress is an essential material property for integrating stress-strain behavior into computational modeling. However, ASTM D143 does not specify a method for calculating the yield stress of wood in compression perpendicular to the grain (ASTM International 2022a). A literature review of 54 papers reveals that no dominant method has been established for determining strength in compression perpendicular to the grain, and testing methods can often be misaligned with analysis procedures. Many papers reviewed utilizing ASTM D143 testing procedures do not specify the analysis method used and use generic language to describe the strength, further highlighting the need to standardize calculation procedures.

This paper compared four different analysis methods for defining compression perpendicular to grain yield stress: the visual method (implied by ASTM D143), ISO 13061-5, EN 408, and EN 12512. The visual method, implied by ASTM D143, and ISO 13061-5 are intended for small, clear wood samples, while EN 408 is intended for structural-scale samples. EN 12512 is a standard test methodology for cyclic testing of mechanical joints in timber structures; however, its process for defining yield stress has been previously applied to clear wood compression strength in the literature. Compression perpendicular to grain tests were performed in accordance with ASTM D143 and analyzed utilizing methodologies outlined in several international testing procedures (ASTM International 2022a). ANOVA results indicated statistically significant differences in yield stresses across the methodologies, highlighting a need for a standardized yield stress calculation method in ASTM D143. The method outlined in EN 12512a is recommended for implementation with ASTM D143 testing proce-

dures as it provides a fully automated, analytically efficient yield stress calculation procedure that is not sensitive to data cleaning methods (British Standards Institution 2005; ASTM International 2022a).

Acknowledgements

The authors would like to thank Dr. Sujit Bhandari for his feedback during the editing process.

Author CRediT Statement

Zoe A. E. Sperduto: Methodology, Investigation, Formal Analysis, Writing – Original Draft, Writing – Review and Editing; Fiona A. O'Donnell: Conceptualization, Methodology, Investigation, Writing – Original Draft, Writing – Review and Editing, Supervision

References

American Wood Council (2024) National Design Specification for Wood Construction. Leesburg, VA. https://awc.org/resources/2024-nds-supplement/.

Ang A, Ashaari Z, Bakar E, Sahri M, Anwar KM, Jawaid M (2014) Possibility of improving the properties of mahang wood (*Macaranga* sp.) through phenolic compreg technique. Sains Malays 43(2):219–225. https://www.researchgate.net/publication/260689812_Possibility_of_Improving_the_Properties_of_Mahang_Wood_Macaranga_sp_through_Phenolic_Compreg_Technique_Kemungkinan_untuk_Meningkatkan_Sifat_Kayu_Mahang_Macaranga_sp_melalui_Teknik_Compreg_Fenolik

Arriaga F, Wang X, Íñiguez-González G, Llana DF, Esteban M, Niemz Pl (2023) Mechanical properties of wood: a review. Forests 14(6):1202. https://doi.org/10.3390/f14061202.

ASTM International (2006) ASTM D2555-06: Standard Practice for Establishing Clear Wood Strength Values. ASTM D07 Committee, West Conshohocken, PA. https://doi.org/10.1520/D2555-06

ASTM International (2022a) ASTM D143-22 Test Methods for Small Clear Specimens of Timber. ASTM D07 Committee, West Conshohocken, PA. https://doi.org/10.1520/d0143-09.

ASTM International (2022b) ASTM D245 − 22: Practice for Establishing Structural Grades and Related Allowable Properties for Visually Graded Lumber. ASTM D07 Committee, West Conshohocken, PA. https://doi.org/10.1520/D0245-22.

ASTM International (2022c) ASTM D198: Test Methods of Static Tests of Lumber in Structural Sizes. ASTM D07 Committee, West Conshohocken, PA. https://doi.org/10.1520/D0198-22A .

ASTM International (2023) ASTM D5457-23: Specification for Computing Reference Resistance of Wood-Based Materials and Structural Connections for Load and Resistance Factor Design. ASTM D07 Committee, West Conshohocken, PA. https://doi.org/10.1520/D5457-23 .

ASTM International (2024) ASTM A370-24a: Test Methods and Definitions for Mechanical Testing of Steel Products. ASTM A01 Committee, West Conshohocken, PA. https://doi.org/10.1520/A0370-24A .

ASTM International (2025a) ASTM D1990-25: Practice for Establishing Allowable Properties for Visually-Graded Dimension Lumber from In-Grade Tests of Full-Size Specimens. ASTM D07 Committee, West Conshohocken, PA. https://doi.org/10.1520/D1990-25 .

ASTM International (2025b) ASTM D4442-20 (Reapproved 2025): Test Methods for Direct Moisture Content Measurement of Wood and Wood-Based Materials. ASTM D07 Committee, West Conshohocken, PA. https://doi.org/10.1520/D4442-20R25 .

Bahtiar E, Nugroho N, Rahman MM, Arinana, Sari RK, Wirawan W, Hermawan D (2017) Estimation the remaining service-lifetime of wooden structure of geothermal cooling tower. Case Stud Constr Mater 6:91–102. https://doi.org/10.1016/j.cscm.2017.01.001.

Bahtiar E, Denih A, Priadi T, Putra GR, Koswara A, Nugroho N, Hermawan D (2022) Comparing the building code sawn lumber's wet service factors (CM) with four commercial wood species laboratory tests. Forests 13(12):2094. https://doi.org/10.3390/f13122094 .

Barnes HM, Sanders MG, Lindsay GB (2013) Compression and bending strength of steamed, treated hardwoods. BioResources 9(1). https://doi.org/10.15376/biores.9.1.537-544 .

Basta CT, Gupta R, Leichti RJ, Sinha A (2011) Characterizing perpendicular-to-grain compression (C⊥) behavior in wood construction. Holzforschung 65(6):845–853. https://doi.org/10.1515/hf.2011.104 .

Bodig J (1969) Improved load-carrying capacity of wood in transverse compression. Forest Prod J 19:39–44.

British Standards Institution (1957) BS 373: Methods of testing small clear specimens of timber. https://knowledge.bsigroup.com/products/methods-of-testing-small-clear-specimens-of-timber.

British Standards Institution (2005) BS EN 12512:2001: Timber structures - Test methods - Cyclic testing of joints made with mechanical fasteners. https://standards.iteh.ai/catalog/standards/cen/383a6e35-dd47-46d9-8ac9-e8781263f371/en-12512-2001?srsltid=AfmBOopKQKYE81YsfD_pnpSfSBtUxdcVeDGeRFI-rVcFEyu2Nvp9oTQH.

British Standards Institution (2012) EN 408: Timber structures. Structural timber and glued laminated timber. Determination of some physical and mechanical properties. BSI Standards Limited. https://knowledge.bsigroup.com/products/timber-structures-structural-timber-and-glued-laminated-timber-determination-of-some-physical-and-mechanical-properties.

Chen M, Li S, Lyu J, IOP (2019) Physical and mechanical properties of *Cupressus funebris* Endl. wood. Mater Sci Eng 493:012105. https://doi.org/10.1088/1757-899X/493/1/012105 .

Cheng Y, Chan AHC, Holloway D, Nolan G (2022) Anisotropic material behaviour under compression of *Eucalyptus nitens* with high moisture content. Constr Build Mater 314(B). https://doi.org/10.1016/j.conbuildmat.2021.124788 .

Cherry R, Karunasena W, Manalo A (2022) Mechanical properties of low-stiffness out-of-grade hybrid pine-effects of knots, resin and pith. Forests 13(6). https://doi.org/10.3390/f13060927 .

Christensen RM (2008) Observations on the definition of yield stress. Acta Mech 196(3–4):239–244. https://doi.org/10.1007/s00707-007-0478-0 .

Collins S, Fink G (2022) Mechanical behaviour of sawn timber of silver birch under compression loading. Wood Mater Sci Eng 17(2):121–128. https://doi.org/10.1080/17480272.2020.1801836.

Crafford P, Wessels C (2016) The potential of young, green finger-jointed *Eucalyptus grandis* lumber for roof truss manufacturing. South For 78(1):61–71. https://doi.org/10.2989/20702620.2015.1108618.

Crespo J, Majano-Majano A, Lara-Bocanegra AJ, Guaita M (2020) Mechanical properties of small clear specimens of *Eucalyptus globulus* Labill. Materials 13(4):906. https://doi.org/10.3390/ma13040906.

Feujofack K BV, Loss C (2023) Experimental campaign on the mechanical properties of Canadian small clear spruce-pine-fir wood: Experimental procedures, data curation, and data description. Data Brief 48:109064. https://doi.org/10.1016/j.dib.2023.109064 .

Fruehwald-Koenig K, Heister L (2024) Macro- and micromechanical behavior of oil palm wood (*Elaeis guineensis* JACQ): tensile, compression and bending properties. Eur J Wood Wood Prod 82(6):1879–1899. https://doi.org/10.1007/s00107-024-02131-w .

Gambarelli S, Bosnjak J, Platas R, Jin K (2025) Experimental study on mechanical properties of European oak and Norway spruce clear wood. Materials 18(14). https://doi.org/10.3390/ma18143257.

German Institute for Standardization (1979a) DIN 52192:1979-05 Testing of wood; compression test perpendicular to grain. https://www.dinmedia.de/en/standard/din-52192/625320.

German Institute for Standardization (1979b) DIN 52185:1976-09 Testing of wood; compression test parallel to grain. https://www.dinmedia.de/en/standard/din-52185/596847.

Gupta A, Jain L, Dutt B, Kumar R, Sharma S (2023) Behavioral change in physical, anatomical, and mechanical characteristics of thermally treated *Pinus roxburghii* wood. BioResources 18(4):7769–7795. https://doi.org/10.15376/biores.18.4.7769-7795 .

Hong J-P, Lee J-J, Yeo H, Kim C-K, Pang S-J, Oh J-K (2016) Parametric study on the capability of three-dimensional finite element analysis (3D-FEA) of compressive behaviour of Douglas fir. Holzforschung 70(6):539–546. https://doi.org/10.1515/hf-2015-0151 .

Hussein M, Nassar K, Darwish M (2019) The effect of the moisture content on some mechanical properties for Casuarina wood. In A Zingoni (Ed.), Advances in Engineering Materials, Structures and Systems: Innovations, Mechanics and Applications - Proceedings of the 7th International Conference on Structural Engineering, Mechanics and Computation, CRC Press, London, pp. 1757–1761.

Hussein MM, Nassar K, Darwish M (2019) Mechanical Properties of Egyptian *Casuarina* Wood. J Mater Civ Eng 31(12). https://doi.org/10.1061/(ASCE)MT.1943-5533.0002955 .

Ido H, Nagao H, Kato H, Miyatake A, Hiramatsu Y (2010) Strength properties of laminated veneer lumber in compression perpendicular to its grain. J Wood Sci 56(5):422–428. https://doi.org/10.1007/s10086-010-1116-3.

Ike V, Jesus A, Mojtabaei S (2025) Experimental investigation of the moisture-dependent behaviour of Norway spruce glulam beams. Constr Build Mater 497. https://doi.org/10.1016/j.conbuildmat.2025.143807.

Indian Standards Institution (1986) IS:1780 Indian Standard Methods of Testing Small Clear Specimens of Timber. https://law.resource.org/pub/in/bis/S03/is.1708.1-18.1986.pdf.

Instron (2023) Proportional Limit. https://www.instron.com/en/resources/glossary/proportional-limit/.

International Organization for Standardization (1975) ISO 3132:1975 Wood — Testing in compression perpendicular to grain. https://www.iso.org/standard/8290.html.

International Organization for Standardization (2014) ISO 13910:2014 Timber structures — Strength graded timber — Test methods for structural properties. https://www.iso.org/standard/52977.html.

International Organization for Standardization (2017) ISO 13061-17 Physical and mechanical properties of wood — Test methods for small clear wood specimens Part 17: Determination of ultimate stress in compression parallel to grain. https://www.iso.org/standard/60079.html.

International Organization for Standardization (2020) ISO 13061-5 Physical and mechanical properties of wood — Test methods for small clear wood specimens Part 5: Determination of strength in compression perpendicular to grain. https://www.iso.org/standard/74335.html.

Irby N, França FJN, Barnes HM, Seale RD, Shmulsky R (2020) Effect of growth rings per inch and specific gravity on compression perpendicular to grain in No. 2: 2 by 8 and 2 by 10 southern pine lumber. Forest Prod J 70(2):213–220. https://doi.org/10.13073/FPJ-D-19-00043 .

Japan Standards Association (1994) JIS Z 2101: Methods of test for woods. https://archive.org/details/jis.z.2101.j.1994.

Jiang T, Gao H, Sun J, Xie Y, Li X (2014) Impact of DMDHEU resin treatment on the mechanical properties of poplar. Polym Polym Comps 22(8):669–674. https://doi.org/10.1177/096739111402200803.

Kiaei M, Abadian Z (2018) Physical and mechanical properties of hornbeam wood from dominant and suppressed trees. Drv Ind 69(1):63–69. https://doi.org/10.5552/drind.2018.1705.

Kijidani Y, Morita H, Aratake S, Tsuyama T, Arima T (2019) Partial compression strength of sugi (Japanese cedar, *Cryptomeria japonica*) wood near the pith perpendicular to the grain. J Wood Sci 65(1):16. https://doi.org/10.1186/s10086-019-1796-2.

Kotlarewski N, Belleville B, Gusamo B, Ozarska B (2016) Mechanical properties of Papua New Guinea balsa wood. Eur J Wood Wood Prod 74(1):83–89. https://doi.org/10.1007/s00107-015-0983-0.

Kovryga A, Stapel P, van de Kuilen J (2020) Mechanical properties and their interrelationships for medium-density European hardwoods, focusing on ash and beech. Wood Mater Sci Eng 15(5):289–302. https://doi.org/10.1080/17480272.2019.1596158.

Kunesh RH (1968) Strength and elastic properties of wood in transverse compression. Forest Prod J 18:65–72.

Kurt S, Korkmaz M (2022) Effects of moisture and direction of grain on the thermal conductivity and mechanical properties of black alder and Scots pine. Kastamonu Univ J For Fac 22(1):33–39. https://doi.org/10.17475/kastorman.1095741.

Leijten AJM, Franke S, Quenneville P, Gupta R (2012) Bearing strength capacity of continuous supported timber beams: Unified approach for test methods and structural design codes. J Struct Eng 138(2):266–272. https://doi.org/10.1061/(asce)st.1943-541x.0000454 .

Leijten AJM, Larsen HJ, Van der Put TACM (2010) Structural design for compression strength perpendicular to the grain of timber beams. Constr Build Mater 24(3):252–257. https://doi.org/10.1016/j.conbuildmat.2009.08.042.

Lukowsky D, Keiser U, Gohla A (2018) Strength properties of Scots pine from harbour piles degraded by erosion bacteria. Eur J Wood Wood Prod 76(4):1187–1194. https://doi.org/10.1007/s00107-018-1304-1.

Marasigan O, Alipon M, Bondad E, Hopia K (2024) Physical and mechanical properties of thirteen senile fruit-bearing trees in the Philippines and their potential uses. J Trop For Sci 36(1):91–104. https://doi.org/10.26525/jtfs2024.36.1.91 .

Mendes RAB, Benincá ME, Subhani M, Acosta AP, Delucis RdA, Désir JM, Morsch IB, Ilgın HE, Karjalainen M (2024) Cross-laminated timber (CLT) in compression perpendicular to the plane: experimental analysis on the column below the wall load configuration. Buildings 14(3):607. https://doi.org/10.3390/buildings14030607.

Milch J, Tippner J, Sebera V, Brabec M (2016) Determination of the elasto-plastic material characteristics of Norway spruce and European beech wood by experimental and numerical analyses. Holzforschung 70(11):1081–1092. https://doi.org/10.1515/hf-2015-0267.

Miyamoto B, Sinha A, Leavengood S, Morrell J, DeVisser D, Kruse D (2018) Mechanical property assessment for establishing design values of western juniper. Wood Fiber Sci 50(2):167–179. https://doi.org/10.22382/wfs-2018-018.

Moya L, Laguarda-Mallo M, Cagno M, Cardoso A, Gatto F, O'Neill H (2013) Physical and mechanical properties of loblolly and slash pine wood from Uruguayan plantations. Forest Prod J 63(3–4):128–137. https://doi.org/10.13073/FPJ-D-13-00024

Müller K, Sonderegger W, Kläusler O, Klippel M, Escamilla EZ (2020) Mechanical characterisation of densified hardwood with regard to structural applications. J Renew Mater 8(9):1091–1109. https://doi.org/10.32604/jrm.2020.09483.

Muthumala C, De Silva S, Arunakumara K, Alwis P (2021) Failure modes and compression strength of seven finger-jointed wood species from Sri Lanka. J Fail Anal Prev 21(6):2215–2223. https://doi.org/10.1007/s11668-021-01274-9.

Naissi M, Pranjic A, Yancheva S, Trautz M (2025) Vacuum infiltration of bio-based and synthetic polymers for enhancing wood properties in construction. Wood Mater Sci Eng. https://doi.org/10.1080/17480272.2025.2521632.

National Standards of People's Republic of China (2009a) GB/T 1943-2009 Method for determination of the modulus of elasticity in compression perpendicular to grain of wood. https://www.chinesestandard.net/PDF/English.aspx/GBT1943-2009.

National Standards of People's Republic of China (2009b) GB/T 1939-2009 Method of testing in compression perpendicular to grain of wood. https://webstore.ansi.org/standards/spc/gb19392009?srsltid=AfmBOorM-5AWjr55RfEmADbYZmyiKRv4CwcxngXhOaLVppRHL1uobtBK.

Neimsuwan T, Tangkit K, Takuathung CN, Kaakkurivaara N, Meunpong P, Jumwong N, Sangvisitpirom P, Kaakkurivaara T (2024) Mechanical and

physical properties of three *Eucalyptus* spp. clones planted in Thailand. J For Sci 70(10):512–528. https://doi.org/10.17221/34/2024-JFS .

Pang S, Liang L, Tao W, Liu Y, Huan S, Qin H (2019) Effect of the strain rate and fiber direction on the dynamic mechanical properties of beech wood. Forests 10(10):881. https://doi.org/10.3390/f10100881 .

Pellicane P, Bodig J, Mrema A (1994) Modeling wood in transverse compression. J Test Eval 22(4):376–382. https://doi.org/10.1520/JTE11848J .

Piernik M, Woźniak M, Pinkowski G, Szentner K, Ratajczak I, Krauss A (2022) Color as an indicator of properties in thermally modified Scots pine sapwood. Materials 15(16):5776. https://doi.org/10.3390/ma15165776 .

Pleschberger H, Teischinger A, Müller U, Hansmann C (2013) Mechanical characterization of lumber of small-diameter hardwood species after different drying schedules. Dry Technol 31(9):1056–1062. https://doi.org/10.1080/07373937.2013.772899 .

Rosner S, Luss S, Konnerth J, Kunert N (2024) Radial compression strength can predict the hydraulic vulnerability of mature Norway spruce sapwood. Maderas-Cienc Tecnol 26:1–8. https://doi.org/10.22320/s0718221x/2024.19.

Roszyk E, Stachowska E, Majka J, Mania P, Broda M (2020) Moisture-dependent strength properties of thermally-modified *Fraxinus excelsior* wood in compression. Materials 13(7):1647. https://doi.org/10.3390/ma13071647.

Saltik B (2025) Effects of microwave and infrared plus microwave drying of wood materials on energy consumption, water absorption, and mechanical properties. BioResources 20(1):282–294. https://doi.org/10.15376/biores.20.1.282-294.

Sharma SK, Kelkar BU (2021) Effect of densification on certain physical and mechanical properties of inner soft wood of *Borassus flabellifer* L. J Indian Acad Wood Sci 18(1):39–44. https://doi.org/10.1007/s13196-021-00277-1 .

Shmulsky R França FJN, Ratcliff JT, Farber B, Senalik CA, Ross RJ, Seale RD(2021) Compression properties of small clear southern yellow pine specimens tested across five decades. Forest Prod J 71(3):240–245. https://doi.org/10.13073/FPJ-D-20-00039 .

Shukla S, Viswanath S (2023) Comparison of growth and few wood quality parameters of 24-25-year-old *Tectona grandis* (teak) trees raised under three agroforestry practices. Agrofor Syst 97(4):631–645. https://doi.org/10.1007/s10457-023-00815-5 .

Skarvelis M, Mantanis G (2013) Physical and mechanical properties of beech wood harvested in the Greek public forests. Wood Res 58(1):123–129. https://www.woodresearch.sk/wr/201301/13.pdf

Smídová E, Kabele P, Sejnoha M (2022) Material parameters of European spruce for tensile-shear fracture modeling. Eng Struct 270. https://doi.org/10.1016/j.engstruct.2022.114534 .

Standards Australia, Standards New Zealand (2010) AS/NZS 4063-1:2010 - Characterization of structural timber. Part 1, Test methods. Standards Australia; Standards New Zealand. https://store.standards.org.au/product/as-nzs-4063-1-2010 .

Tippner J, Hrivnák J, Kloiber M (2016) Experimental evaluation of mechanical properties of softwood using acoustic methods. BioResources 11(1):503–518. https://bioresources.cnr.ncsu.edu/resources/experimental-evaluation-of-mechanical-properties-of-softwood-using-acoustic-methods/

Toba K, Nakai T, Saito H (2024) Effects of wood drying temperatures on the reduction in mechanical properties of Japanese cedar (*Cryptomeria japonica* D. Don) perpendicular to grain. buildings 14(9). https://doi.org/10.3390/buildings14092624 .

Turkish Standards Institution (1976) TS 2473 Wood - Testing in Compression Perpendicular to Grain. https://standards.globalspec.com/std/1055453/ts-2473

Uzcategui M, Seale R, França F (2020) Physical and mechanical properties of hard maple (*Acer saccharum*) and yellow poplar (*Liriodendron tulipifera*). Forest Prod J 70(3):326–334. https://doi.org/10.13073/FPJ-D-20-00005 .

Verbist M, Branco JM, Nunes L (2020) Characterization of the mechanical performance in compression perpendicular to the grain of insect-deteriorated timber. Buildings 10(1):14. https://doi.org/10.3390/buildings10010014 .

Web of Science Master Journal List - WoS MJL by Clarivate. https://mjl.clarivate.com/home .

Widmann R, Fernandez-Cabo J, Steiger R (2012) Mechanical properties of thermally modified beech timber for structural purposes. Eur J Wood Wood Prod 70(6):775–784. https://doi.org/10.1007/s00107-012-0615-x .

Wu C, Xue J, Song D, Ren G, Zhang J (2022) Mechanical performance of inclined Dougong bracket sets under vertical load: Experimental tests and finite element calculation. J Build Eng 45:103555. https://doi.org/10.1016/j.jobe.2021.103555 .

Yorur H, Kurt S, Yumrutas H (2014) The Effect of aging on various physical and mechanical properties of Scotch pine wood used in construction of historical Safranbolu Houses. Drv Ind 65(3):191–196. https://doi.org/10.5552/drind.2014.1328 .

Yu X, Wei N, Liu Q, Wu Z, Fan M, Zhao W, Zeng Q (2022) Study on microwave pretreatment technology to improve the effect of shellac impregnation of fast-growing Chinese fir. J Renew Mater 10(8):2041–2053. https://doi.org/10.32604/jrm.2022.018027 .

Zhang C, Chun Q, Lin Y, Wang H, Li P (2022) Experimental and nonlinear finite-element analysis study on lateral push resistance of San-dou components perpendicular and parallel to grain in traditional timber buildings. J Wood Sci 68(41). https://doi.org/10.1186/s10086-022-02049-y.

[This page is intentionally left blank.]